Spring 5-15-2016

Optical Probes in Multiphase Reactors

Boung Wook Lee
Washington University in St. Louis

Washington University in St. Louis

School of Engineering and Applied Science

Department of Energy, Environmental & Chemical Engineering

Dissertation Examination Committee:

Milorad P. Dudukovic, Chair
Pratim Biswas
Renato Feres
Marcus Foston
Palghat A. Ramachandran
Ramaswamy C. Ramaswamy
Heinz Schaettler

Optical Probes in Multiphase Reactors

by

Boung Wook Lee

A dissertation presented to the
Graduate School of Arts & Sciences
of Washington University in
partial fulfillment of the
requirements for the degree
of Doctor of Philosophy

May 2016
St. Louis, Missouri

Table of Contents

List of Figures

List of Tables

Nomenclature

a	Interfacial area (cm^2/cm^3)
D_{BC}	Bubble column reactor diameter
D_g	Axial dispersion coefficient
D_T	Turbine diameter
D_{STR}	Stirred tank reactor diameter
E	Fraction of light emitted at the optical probe tip (flat end)
fb	Impeller rotational frequency
Fl	Flow number
Fr	Froude number
g	Gravitational constant
H_{2D}	2-D bubble column liquid height
H_{ST}	Sparged tank liquid height
H_{STR}	Stirred tank reactor liquid height
L33	Three smaller and three larger cavities
N	Impeller rotational rate (RPM)
N_A, N_B	Local bubble count measured by optical probes oriented at opposite directions
$N(1), N(2)$	Local bubble count due to bubbles traveling at opposite directions
P_A, P_B	Local gas holdup measured by optical probes oriented at opposite directions
$P(1), P(2)$	Local gas holdup due to bubbles traveling at opposite directions
Q_g	Gas flow rate (m^3/s)
R	Fraction of light reflected at the optical probe tip

R_{BC}	Bubble column reactor radius
R_{STR}	Radius of the stirred tank reactor
R_{xx}	Autocorrelation sequences
RC	Ragged cavities
S33	Three large and three clinging cavities
T_{2D}	2-D bubble column thickness
t_r	Time for one impeller rotation
U_{gas}	Superficial gas velocity
V	Volume fraction (phase holdup)
$V_{normalized}$	Normalized voltage signal
VC	Vortex clinging cavities
W_{2D}	2-D bubble column width
x_1, x_2	Fraction of bubbles approaching from the backside of the probes that are captured
1L	Clinging cavities
2L	Two large cavities

Greek Symbols

α	Void fraction (gas holdup)
β	Acceptance angle
$\varepsilon_{gas,\ local}$	Local gas phase holdup
$\varepsilon_{gas,\ local}$	Global gas phase holdup
θ	Impact angle
υ	Probe orientation with respect to major bubble movement direction

List of Abbreviations

ADM	Axial Dispersion Model
CARPT	Computer Automated Radioactive Particle Tracking
CDT	Half circular blades disk turbine
CFD	Computational Fluid Dynamics
CREL	Chemical Reaction Engineering Laboratory
CSTR	Continuously Stirred Tank Reactor
CT	Computed Tomography
DFT	Discrete fourier transform
FPS	Frames Per Second
GXL	Gas Expanded Liquid
HSC	High Speed Camera
OPPM	Optical Probe Probabilistic Model
PFR	Plug Flow Reactor
PSD	Power spectral density
RPD	Relative power demand
RPM	Revolutions per minute
RT	Ruston Turbine
RTD	Residence Time Distribution
STR	Stirred tank reactor

Acknowledgments

As I write this dissertation, I can think of dozens of people I am truly grateful for. First and foremost, I would like to thank God for blessing me with many things in my life. My time here at Washington University as an undergraduate and graduate student hasn't been a short one, and I've certainly had ups and downs. It is also during this time I was blessed to have met my wife, Hyunmin, and have welcomed Joshua into our family. I don't know where this life will take us, but I am very much looking forward to it!

I am so grateful to have met my advisor, Professor Dudukovic, during my senior year. Taking reaction engineering course after two years of absence was not the most exciting thing, but looking back, meeting him through this course has been nothing but a true blessing. Professor Dudukovic, THANK YOU for everything!

I would like to thank Professors Biswas, Foston, and Ramachandran from the EECE Department, Professor Schaettler from the ESE Department, Professor Feres from the Math Department, and Dr. Ramaswamy from Eastman, for serving as my committee member and enriching my experience as a researcher. Professor Biswas, thank you for making my stay at CREL possible; Professor Foston, thank you for providing very useful comments on my presentations; Professor Ramachandran, thank you for introducing me the transport phenomena subject (and for your great book); Professor Schaettler, thank you for going over the optical probe probabilistic model and your fantastic teaching; Professor Feres, thank you for making yourself available at various times; Dr. Ramaswamy, thank you for your sharp questions and suggestions on the optical probe technique.

I undoubtedly owe a lot to former CREL students and their work. Dan, Mehmet, Vesna, Mohamed, and many others prior to them, thank you for your outstanding work and kindness you showed. Yujian and Onkar, thank you for everything you've shared with me. As I continue my journey as an engineer, I hope we cross paths as colleagues once again.

Last but not least, I would like to extend my thanks to Professor Jim Ballard from the Engineering Communication Center and Rose from the EECE Department for all their help. Professor Ballard and Rose, thank you.

As I leave Washington University and CREL, I hope I was able to have positive impact on others and have created useful knowledge.

"Tim" Boung Wook Lee

Washington University in St. Louis

May 2016

ABSTRACT OF THE DISSERTATION

Optical Probes in Multiphase Reactors

by

Boung Wook Lee

Doctor of Philosophy in Energy, Environmental & Chemical Engineering

Washington University in St. Louis, 2016

Professor Milorad P. Dudukovic, Chair

This dissertation examines the application of optical probe techniques in two predominant multiphase reactors used for contacting gas and liquid phases: bubble column reactors and gas-liquid stirred tank reactors. Multiphase reactors are ubiquitous in industry, and for most processes, successful operation depends on successful inter- and intra-phase contacting and mixing. Extensive modeling and experimental research efforts have been made for better reactor design, modeling, and scale-up, yet, much remains unknown about the gas phase.

Optical probes offer significant advantages for gas phase dynamics measurements. Consequently, they have been adapted by numerous researchers around the world for detailed fluid dynamic investigations and model verifications. However, optical probes do possess a key disadvantage, the invasiveness that causes the measured parameters to show directional sensitivity.

Considering this often-overlooked disadvantage, this dissertation first details the development of the Optical Probe Probabilistic Model (OPPM), which turns the directional sensitivity into an advantage. The model makes use of simple logical assumptions and is gives novel information about bubble history that can be used for many things, e.g., sparger design, baffle design, and reactor modeling.

The application of the OPPM in a lab-scale bubble column reactors is then shown. For the (largest) mid-column zone, the results reveal the highest degree of gas phase backmixing in the transition flow regime. A plug flow reactor (PFR) like behavior, with the smallest degree of backmixing, was observed in the same zone for the homogeneous and heterogeneous flow regimes. For the entrance and exit zones, the gas phase dynamics showed very complex behavior that required case-by-case treatment.

Lastly, the dissertation discusses the usefulness of time-series analysis methods for optical probe measurements. In particular, it examines their use in lab-scale gas-liquid stirred tank reactors (STR) equipped with either a Ruston turbine (RT) or half circular blades disk turbine (CDT). The analyses reveals a physical local gas phase distinction between different global hydrodynamic flow regimes. These findings show the potential of optical probes as an industrial validation and control tool.

Chapter 1. Introduction and objectives

Multiphase reactors are prevalent in all sectors of industry, including the chemical, petrochemical, biochemical, and pharmaceutical sectors. Successful intimate contacting between reactants in the same or different phases is essential for maximizing reactor performance. Thus, the goal of multiphase multiscale reaction engineering is quantification of kinetics, multiphase flow, intra and interphase transport, and their interactions on various scales (Figure 1.1).

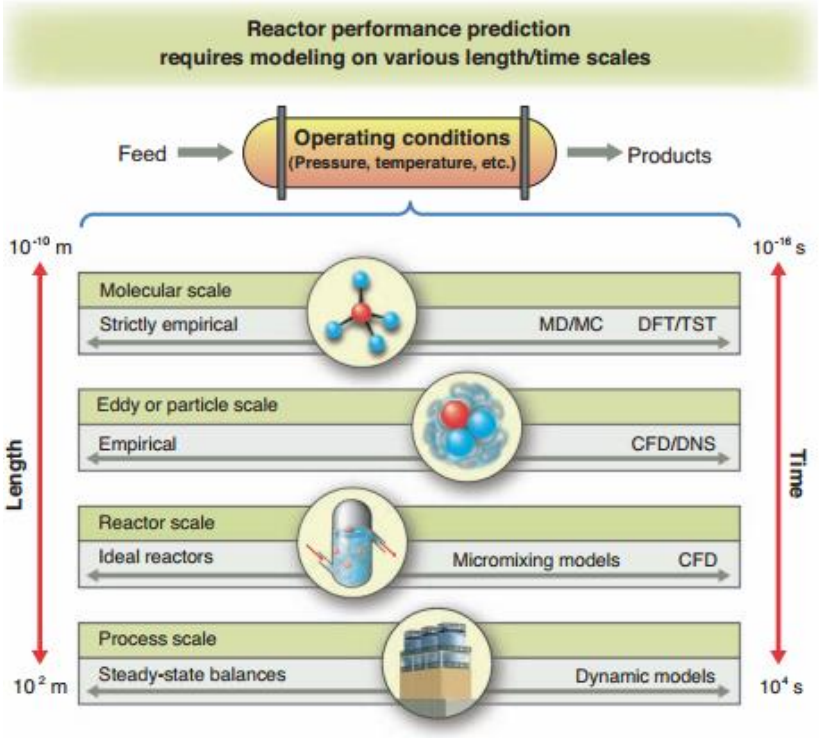

Figure 1.1: Scales in multiscale reaction engineering (source: Dudukovic, 2009).

Figure 1.2 shows some of the most commonly used multiphase reactors for treating single and multiphase reactants and products. Reactors that involve only one changing phase (the upper

figures) are still considered as multiphase reactors because the reactions that take place are multiphase in nature.

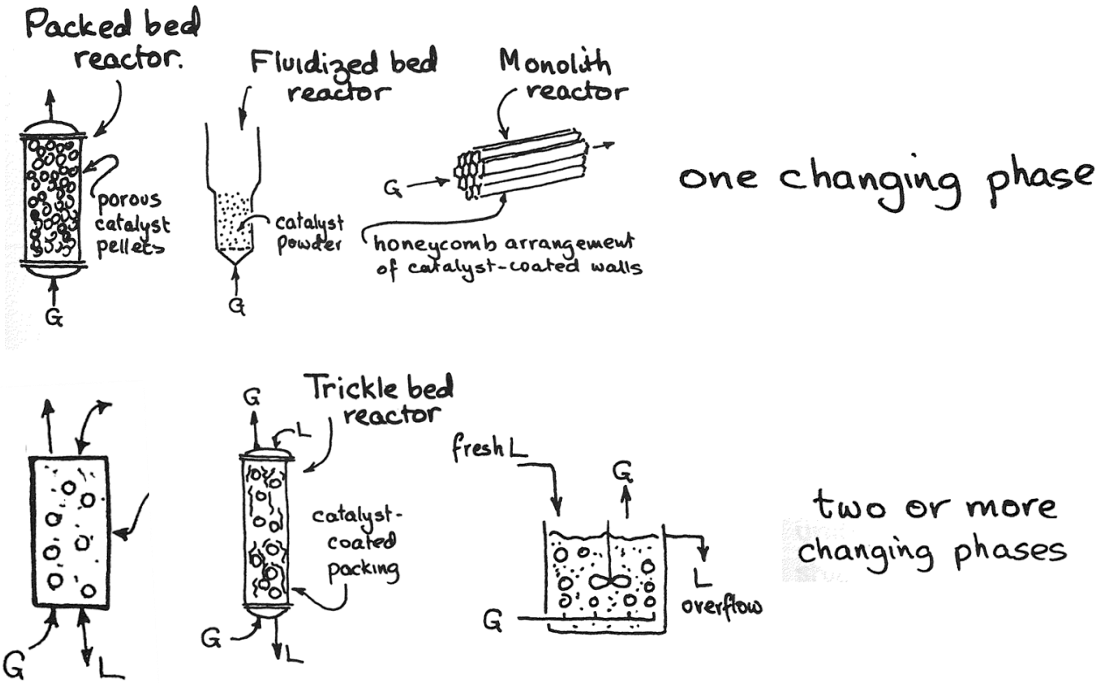

Figure 1.2: Various reactor types (source: Lenvenspiel, 2002).

For full description / prediction of overall reactor performances, calculating full solutions describing reactor momentum, mass, and energy at all scales is most desirable. However, in practical situations this cannot be done based on first principles, despite all the computational advancements made within the last couple decades, e.g., computational fluid dynamics (CFD). Important parameters associated with flow and turbulence must be approximated based on simplifying assumptions for a particular observable scale, and the results are subject to validation by appropriate experimental data. While much success has been reported for single-phase systems, much remains to be uncovered for multiphase systems and reactors, where most processes are being operated (Dudukovic et al., 2002). Theoretically, CFD can provide what is

sought with only a few assumptions; however, due to the already highly complex nature of flow characteristics and the typically large reactor dimensions, further simplifying models/assumptions are generally used. For practical processes, the results are even more prone to error due to other physicochemical properties one should consider. Detailed investigation via proven experimental techniques is required for a more accurate process and reactor design, modeling, and control.

Over the years, much effort has been expended on development of reliable techniques, as summarized by Boyer et al. (2002), Chaouki et al. (1997) and Yang et al. (2007). Because all techniques have particular advantages and disadvantages, care must be given when choosing which technique to use. Figure 1.3 shows available measurement techniques in multiphase systems and reactors, as summarized by Mueller (2009).

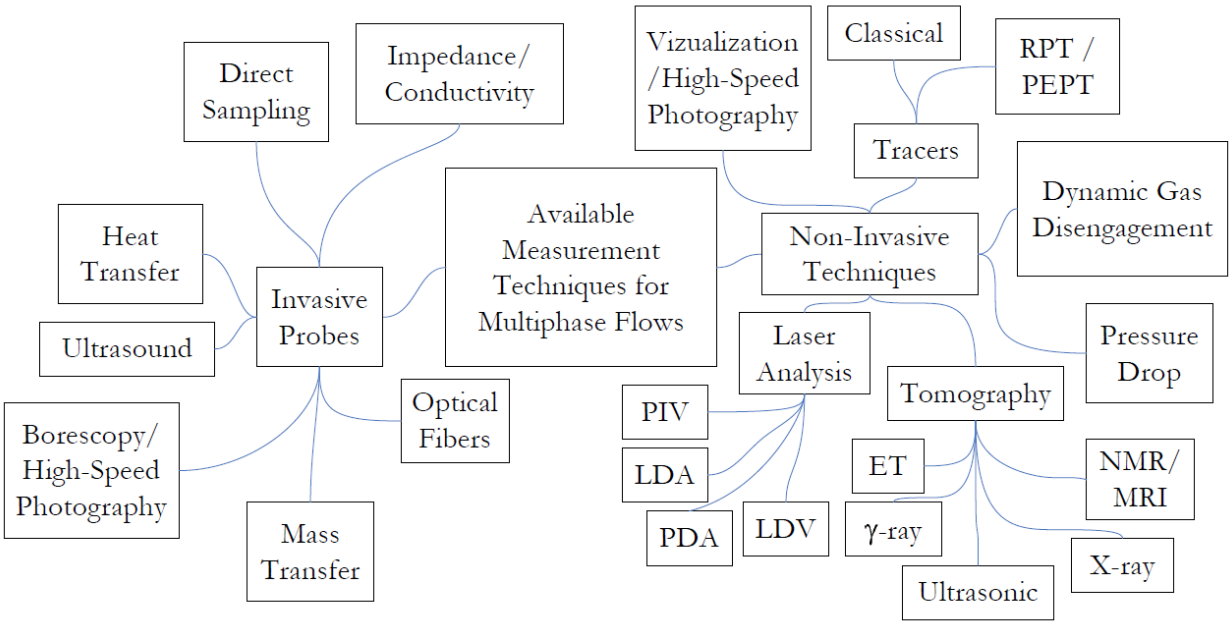

Figure 1.3: Measurement techniques for multiphase reactors (source: Mueller, 2009).

In our Chemical Reaction Engineering Laboratory (CREL), a number of different experimental techniques have been utilized to characterize local and global fluid dynamic behaviors for all three phases involved, i.e., liquid, solid, and gas phases. These include radioactive particle tracking (RPT) methods, tracers, tomographies, pressure drop measurements, high-speed photography, conductivity probes, optical fiber / probes, mass transfer probes, and borescopy. In particular, the development of computer automated radioactive particle tracking (CARPT) and computed tomography (CT) and their utilization in bubble column reactors (e.g., Devanathan, 1991; Degaleesan, 1997; Gupta, 2002), in risers (e.g., Bhusarapu, 2005), and in stirred-tank reactors (e.g., Rammohan, 2002; Guha, 2007), positioned the CREL at the forefront of multiphase multiscale reactor modeling and scale-up research. First-principle and turbulence-based models were developed and verified by detailed measurements for the solid and liquid phases, and the developed reactor models were successfully applied in commercial processes (e.g., Degaleesan, 1997).

For the gas phase, however, much research remains to be done, because the available techniques have very little ability to give detailed local dynamic behaviors. Most reactor models rely on global measurements from conventional tracer methods, e.g., Han (2007) and Hamed (2012), yet gas phase dynamics dominate the hydrodynamics of all other phases, due to their higher volumetric flow rate of the gas phase. For example, for bubble column reactors, Degaleesan (1997) noted that the liquid superficial velocity – the volumetric flow rate divided by the cross sectional area – is at least by an order of magnitude less than that of the gas phase for most applications. For gas-liquid stirred tank reactors, Mueller (2009) identified one of the key challenges for successful reactor design, modeling, and scale-up: the lack of phenomenological

descriptions of gas phase dynamics, e.g., local and global gas phase holdup and detailed bubble dynamics. Clearly, a deeper understanding of gas phase dynamic behaviors is needed for better reactor design, modeling, and scale-up. Optical probes possess this exact potential.

1.1. Research objectives

This work seeks to advance the understanding of the gas phase dynamics of gas and liquid multiphase reactors by using the optical probe technique. The specific research goals and chapters are listed below:

- Advance the optical probe technique by making use of its invasiveness, which is otherwise considered its key disadvantage (Chapter 2).
- Enhance the understanding of gas-phase backmixing behavior in bubble column reactors (Chapter 3).
- Enhance the understanding of gas-phase dynamics in gas-liquid stirred tank reactors (Chapter 4).

Chapter 2. Optical probes in gas-liquid reactors and the Optical Probe Probablistic Model (OPPM)[1]

Since their first development circa 1980s, optical probe techniques have had much success in multiphase reactor studies. Several tip configurations were developed (Cartellier, 1990, 1992; Fordham et al., 1999a, 1999b, 1999c; Guet et al., 2003; Julia et al., 2005) and used to measure important fluid and flow properties. In the CREL, the optical probe technique has been proven to be one of the most versatile tools for characterizing gas phase dispersions by measuring local gas phase holdups and bubble dynamics. Optical probes offer several distinct advantages: simple setup, easy signal interpretation, a high signal-to-noise ratio, a wide range of applicable media, and many operating conditions including high temperature and pressure.

First adopted in the CREL by Xue (2004), the optical probe technique has been successfully applied to bubble columns (Youssef, 2010; Hamed, 2012), slurry bubble columns (Wu, 2007), gas-liquid stirred tanks (Mueller, 2009), and pressurized autoclaves (Mueller et al., 2007; Mueller and Dudukovic, 2010). Tapered end, conical probes in particular have proven useful for a wide range of applications.

2.1. Optical probe technique

A typical optical probe technique setup is shown in Figure 2.1. At one end are two optical fibers, connected to a light source (usually a monochromatic laser) and a photodiode. At the other end,

[1] Some material in this chapter was previously published in Lee and Dudukovic (2014a, 2014b, 2015).

the probe tip ‘sees’ the medium. As the illuminating light travels along the fiber and reaches its tip, it is partially reflected and refracted. The extent depends on the geometric configuration of the tip and the refractive index of the surrounding medium. Reflected light travels back until it reaches the photodiode, where its intensity (the information we seek) is recorded by opto-electric devices.

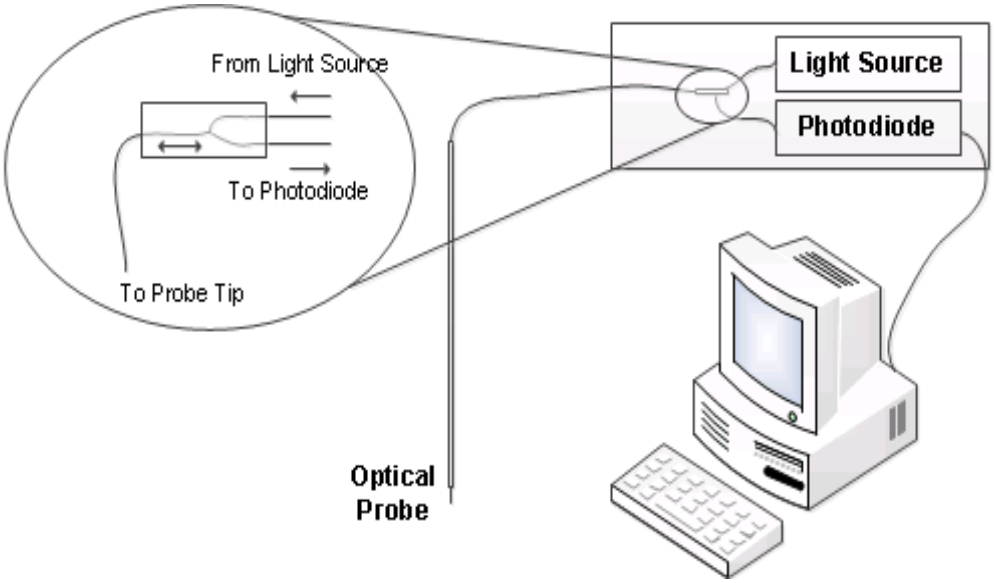

Figure 2.1: Optical probe technique setup.

All optical probes used in the CREL are made in-house by sheathing one or more optical fiber(s) in a metal jacket, so from here on, “probe” will refer to optical fiber(s) sheathed in a metal jacket. Depending on the desired measurement type, e.g., local gas holdup or bubble dynamics, tips are crafted into specific shapes either via the method outlined by Mueller (2009) or by the fiber manufacturer’s manual. Tapered (conical) and flat ended optical fibers have been utilized in the CREL to make three probe tip types.

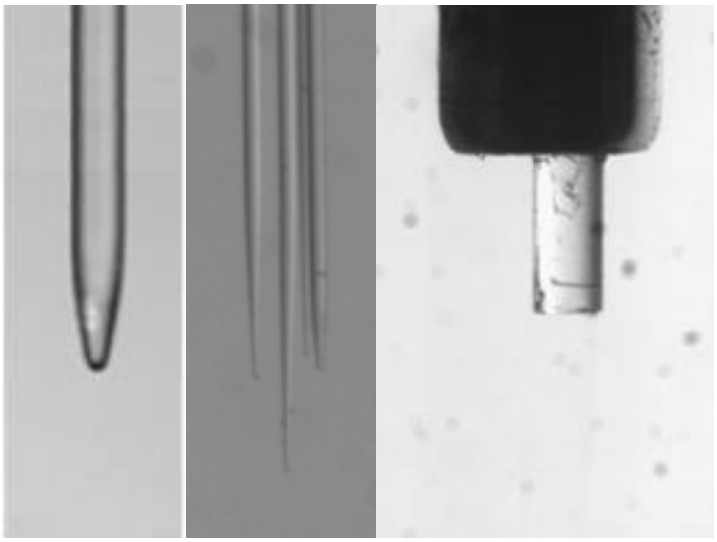

Figure 2.2: Optical probe tip types (left, single point; middle, four point; right, flat end).

For tapered end optical fibers (single and four point optical probes), a binary-like signal is observed when they are immersed in gas and liquid reactors. This signal is a result of different refractive indexes of the gas and liquid phases, and the contact angle of the tips. The binary-like collected signals are then processed using advanced algorithms developed in the CREL to give detailed gas phase dispersion and dynamic information. For a flat end optical probe, interpreting the signal is a very complex task, because the amount of light reflected at the tip-medium interface is a function of both the refractive index and the exposure area – which cannot be quantified in great detail in very turbulent flow conditions.

The detailed principles of operation and detailed descriptions of each configuration are given in Appendix A, and the crucial parameters obtainable from each tip when immersed in gas liquid reactors summarized in Table 2.1.

Table 2.1: Flow / system parameters obtainable by optical probe.
Bold and italicized represent crucial parameters.

Single point (tapered)	Four point (tapered)	Flat end
• ***Local gas phase holdup*** • Bubble count • Bubble residence time distribution	• Local gas phase holdup • Bubble count • Bubble residence time distribution • ***Bubble velocity distribution*** • ***Bubble chord length distribution*** • ***Bubble approach angle distribution*** • ***Interfacial area***	• Refractive index of the surrounding medium

The most important parameter a single-point optical probe can measure is the local gas phase holdup. Local and global gas phase holdups are defined as the local and global reactor volume fraction occupied by the gas phase. They are crucial parameters because the majority of the experimental and computational research in reactor engineering directed at quantifying gas phase dispersions, intra and interphase mixing, and gas-liquid transport has thus far relied on them. In reactor design equations, e.g., ideal reactor models (CSTR – continuously stirred tank reactor or PFR – plug flow reactor) or phenomenological reactor models (ADM – axial dispersion model), these measures are denoted as $\varepsilon_{gas,\ local}$ and $\varepsilon_{gas,\ global}$.

For a four point optical probe, information regarding bubble dynamics – bubble velocity distribution and bubble chord length distribution – is particularly useful as these parameters are

directly related to the gas phase flow field and bubble drag correlations / coefficients, which are necessary information for detailed reactor models. Appendix A summarizes the flat end probe's capability.

2.2. Optical probe probabilistic model (OPPM)

Despite all of the advantages of the tapered end optical probe technique, a significant and often-neglected disadvantage is potential bias when the tip is employed in 'improper' orientations. The probe tip must pierce bubbles to detect them. As a consequence, the probe can detect only bubble populations traveling in certain directions. The probe can miss a significant number of bubbles, especially if the probe tip is much larger than the bubbles and/or the tip is not facing the main flow direction. While several studies have provided general guidelines on how big the probe tip must be, e.g., Mueller (2009), no theoretical foundation has been firmly established for correcting the directional sensitivity of the technique. Notable works which touch on the potential error due to directional sensitivity and attempt to correct it include those by Julia et al. (2005), Mueller and Dudukovic (2010), Lee and Dudukovic (2014a), and Groen (2004). In all of these works, with the exception of the work by Groen (2004), the authors reported 'true' and unbiased local gas holdups based on measurement results obtained from tips that were oriented to face the main flow directions, where either the largest local gas holdups were measured or practically all of the bubbles were assumed to have been captured by the probe. Groen (2004) suggested a model to correct for the directional sensitivity, but it has not been adapted by other researchers most likely due to what he termed "a crude assumption" for the variables he introduced.

While using the optical probe technique in strictly unidirectional flow may result in 'true' and unbiased representation of gas holdup, in other flow conditions, e.g., bubbly or turbulent flows where bubbles fluctuate and move in various directions, it is questionable whether the optical probe measurements yield the 'true' gas holdup. A comprehensive method or model capable of correcting for directional sensitivity is needed. In this section, discussions on the developed optical probe probabilistic model (OPPM) are given.

2.2.1. Experimental setup and the optical probe

To examine the developed model, three experimental setups were used: a gas-liquid stirred tank reactor[2] with a sparger equipped with and without a turbine and baffles, and a 2-D bubble column (Figure 2.3). For the tank reactors, three flow conditions were investigated: one unidirectional flow and two bubbly flow conditions. For the 2-D bubble column, a flow condition with a large amount of gas phase recirculation was investigated.

[2] More discussion on reactor and turbine dimensions is given in chapter 4.

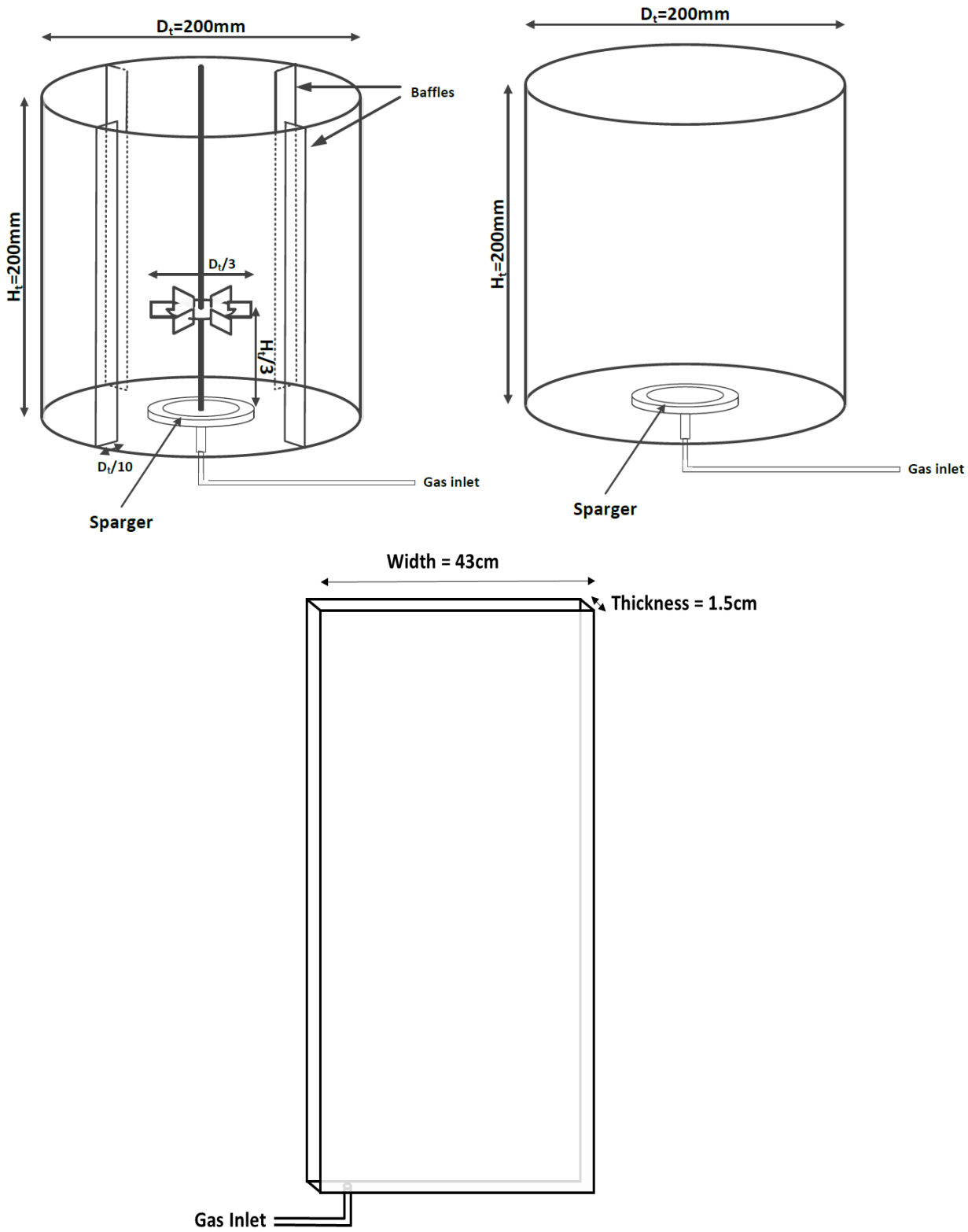

Figure 2.3: Top left: stirred tank equipped with a Rushton Turbine (RT) and four baffles. Top right: sparged tank. Bottom: 2-D bubble column.

Approximately unidirectional flow (stirred tank)

Flooding, loading, and fully recirculated regimes (Figure 2.4) were identified in the stirred tank.[3] The three regimes are marked by distinct differences in the regions which the bubbles occupy and the predominant local bubble movement direction. In the flooding regime, bubbles from the sparger are not effectively dispersed throughout the reactor, and a bubble column-like behavior (bubbly flow) is observed in the central region. In the outer regions, very few to no bubbles are observed. In the loading regime, bubbles from the sparger are dispersed just enough to occupy the upper part of the stirred tank (above the impeller discharge plane) in both the inner (central) and outer regions, and bubbles show a near-unidirectional movement towards the top of the reactor (free surface). In the fully recirculated regime, bubbles occupy all regions of the stirred tank, and recirculation loops are observed below and above the impeller discharge plane. As the turbine revolutions per minute (RPM) is increased and the flow becomes more dispersed, smaller recirculation loops are observed in regions close to the free surface, reactor walls, and the baffles.

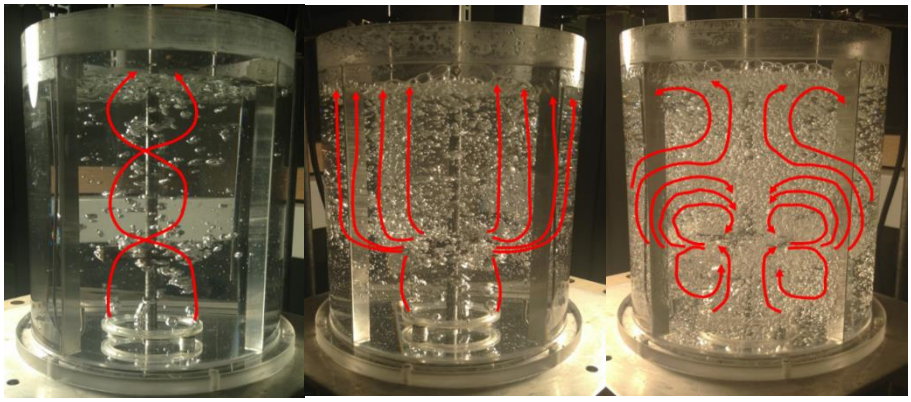

Figure 2.4: The three flow regimes of a gas-liquid stirred tank. Left, the flooding regime; middle, the loading regime; right, the fully recirculated regime. Red lines with arrows represent predominant local bubble movement directions.

[3] More discussion is given in Chapter 4.

Careful visual inspection of the three flow regimes at various operating conditions and regions revealed the most distinct unidirectional flow region to be the upper outer region of the loading regime. Accordingly, the optical probe was deployed at an height of h = 115mm ($0.575H_{STR}$, where H_{STR} = liquid height), a radial position r = $0.9R_{STR}$ (where R_{STR} = radius of the stirred tank), and 45° from the baffle (midway between the two baffles), under operating conditions of 515 RPM and 0.0068 m^3/min of gas flow at standard temperature and pressure. These conditions corresponded to operating dimensionless parameters of *Fl* = 0.045 and *Fr* = 0.5. *Fl* and *Fr* represent *the Flow Number* and *the Froude Number*, respectively, and are the two mostly commonly used dimensionless operating parameters for assessing the flow regime and quantifying the overall degree of dispersion of an air-water stirred tank.[4]

Bubbly flow (stirred and sparged tanks)

For bubbly flow conditions, optical probes were employed in the stirred and sparged tank and sparged tank setups to investigate whether the degree of gas phase dispersions had significant effects on our model results. For the stirred tank, the optical probe was deployed in the region where only a small number of bubbles was observed, at a height of h = 135mm ($0.675H_{STR}$, H_{STR} = liquid height), radial position r = $0.4R_{STR}$ (R_{STR} = radius of the stirred tank), and 45° from the baffle (midway between the two baffles) under operating conditions of 230 RPM and 0.0031 m^3/min (*Fl* = 0.045 and *Fr* = 0.1). For the sparged tank, the optical probe was deployed in a region where a relatively large number of bubbles was observed, at a height of h = $13.5H_{ST}$ (H_{ST} = liquid height) and in the center of the tank, under an operating condition of 0.0087 m^3/min.

[4] More discussion is given in chapter 4.

Flow with large recirculation (2-D bubble column)

To verify the results from the OPPM visually, the optical probe was deployed in the center region of the 2-D bubble column ($0.5H_{2D}$, H_{2D} = liquid height, $0.5W_{2D}$, W_{2D} = width of the column, $0.5T_{2D}$, T_{2D} = thickness of the column) under a gas flow rate 0.0378 m^3/min. The flow was recorded using a high speed camera (HSC) at 240 fps (frames per second). Three experimental conditions were recorded: 1) flow without probe, 2) flow with the probe pointing downward – facing the major bubble movement direction, and 3) flow with the probe pointing upward. For each recording, ~ 180 seconds were recorded and ~ 43,000 images were analyzed.

Optical probe and data acquisition

To make the probes, 105/125/250 μm core/cladding/coating diameter multimode optical fibers from Thorlabs were used. The fibers were first tapered and polished via methods outlined by Mueller (2009) to make their tips conical. The finished fibers were then epoxied into 1/8 inch-diameter stainless steel tubes and inserted into the reactor from the top (free surface) for the stirred and sparged tanks; for 2-D bubble column, the probe was inserted through a side port. For all measurements made in the stirred and sparged tanks, measurements were collected at impact angles (θ) ranging from 0° (facing the main flow direction, towards the bottom of the stirred tank and sparged tank) to 330° (Figure 2.5); for measurements made in 2-D bubble column, two optical probe measurements were made, with the probe tips pointing down and up. The voltage signal from the photodiodes (Thorlabs PDA36A) was collected at a rate of 40 kHz (PowerDAQ PD-BNC-16) for 1500 data acquisition frames, a total duration of 691.2 seconds. For all the setups we investigated, the majority of the bubbles were at least an order of magnitude larger (≥ 1.05 millimeters) than the optical probe tip, as reported in our group's previous work (Xue, 2004;

Mueller, 2009). Hence the measurement inaccuracy caused by drifting and/or deformation of bubble interfaces for "small" bubbles could be ignored (Jiri et al., 2010).[5]

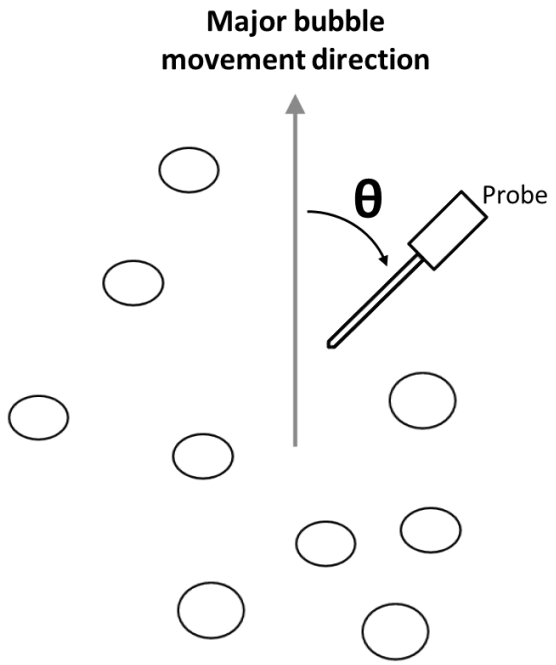

Figure 2.5: 'Needle like' probe in gas-liquid system. Circles represent gas bubbles, and θ represents the impact angle (angle away from the main flow direction and major bubble movement) at which the probe is employed.

Data processing

The collected signals were normalized, first by subtracting the minimum voltage observed during the whole measurement time, and then dividing this value by the difference between a reference voltage and the minimum voltage observed. The reference voltage was set to a value that constrained the dry tip normalized voltage between 0.8 and 1.2. In equation form, this is equivalent to

[5] Signals from tapered end optical probes must first be checked to see if the signals are bimodal. See Appendix C for detailed discussion on errors caused by piercing near the bubble edge and parallel piercing.

$$V_{normalized} = \frac{Meausred\ voltage - Minimum\ voltage}{Reference\ voltage - Minimum\ voltage}. \quad (2.1)$$

2.2.2. Directional sensitivity of 'needle like' probes

There are numerous literature reports based on 'needle like' probe techniques (which include our optical probe technique), as summarized by Boyer et al. (2002), yet only a few consider the directional dependency of their results. To the author's knowledge, the most detailed discussion is provided by Bombac et al. (1997), who included the directional sensitivity of their measurements inside a reactor region where unidirectional flow was observed. For their micro-resistivity probe, which operates on a similar principle to our optical probe and also has a tapered tip, the magnitude of directional dependency was found to be insignificant up to an impact angle (θ) of 90°, suggesting the acceptance angle (β) of their probe to be 180° (Figure 2.6). As the impact angle (θ) increased to 120°, only a slight reduction (10%) in the measured holdup values was reported, and measurement results beyond θ = 150° were not provided.

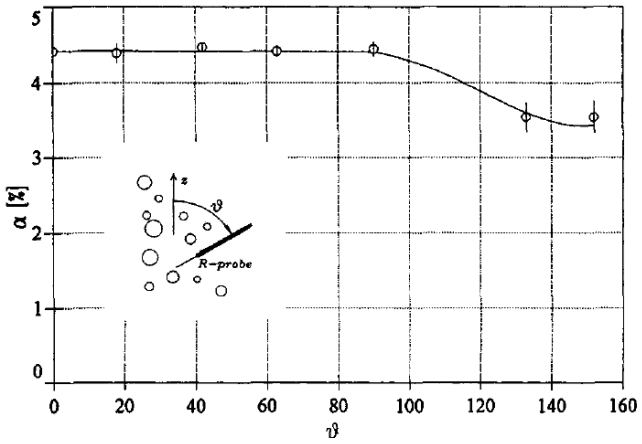

Figure 2.6: Directional sensitivity for the R-probe (resistivity-probe). α represents the void fraction (gas holdup) and υ represents the probe orientation with respect to the major bubble movement direction (Source: Bombac et al., 1997).

From our CREL, Mueller and Dudukovic (2010) and Lee and Dudukovic (2014a) noted the optical probe's directional sensitivity, but included no discussion regarding the magnitude of directional dependency. In theory, the two techniques (resistivity and optical probes) should have equivalent directional sensitivities. However, since numerous attributes can cause differences, e.g., the exact tip shape (angle) and size, processing algorithms, detector sensitivities, bubble size distribution, velocity, and shape, here we present our optical probe's directional sensitivities for the measurements made in the stirred and sparged tanks.

Approximate unidirectional flow

Figure 2.7 shows the gas holdups and bubble counts obtained at impact angles ranging from θ = 0° (Figure 3) to 330°, at intervals of 30°, for the approximate unidirectional flow condition. The results are very similar to what was previously reported by Bombac et al. (1997) with their resistivity probe. As the impact angle (θ) increased from 0° to 90°, i.e., up to an acceptance angle (β) of 180°, the gas holdups and bubble counts remained relatively constant; as the impact angle (θ) increased from 90° to 180°, the two parameters decreased and reached their minimum values before increasing once again as θ increased. The minimum gas holdup and the minimum bubble count observed at θ = 180° were approximately 45 % and 60% of what was observed when the probe was oriented to face the main flow direction (θ = 0°), respectively.

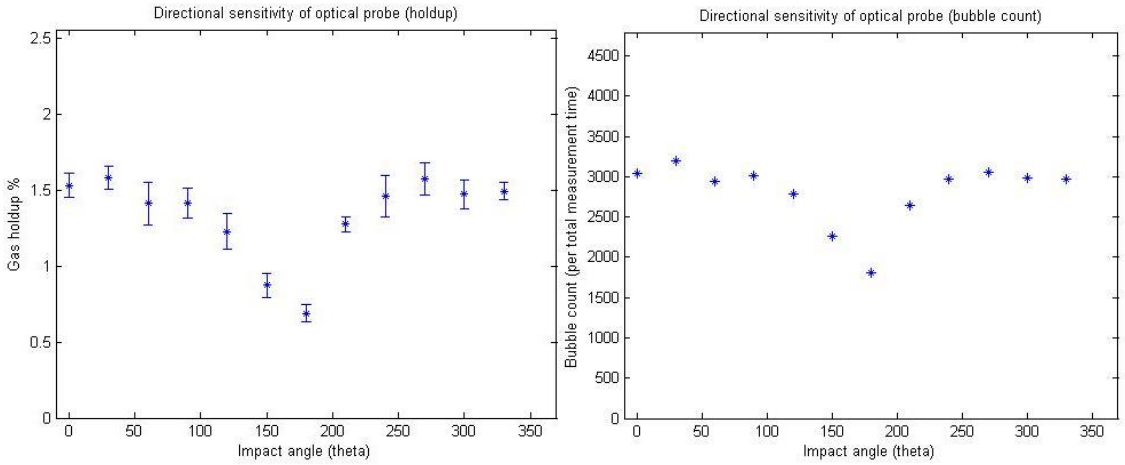

Figure 2.7: Measured gas holdups and bubble counts at various impact angles for approximate unidirectional flow in the stirred tank.

The fact that a significant number of bubbles were detected and contributed to the local gas phase holdup and total bubble count for the probe oriented at $\theta = 180°$ indicates that a significant number of bubbles deviated from the main flow direction, even for a seemingly unidirectional flow: thus the wording 'approximate unidirectional flow' and not 'unidirectional flow.' In gas-liquid systems, bubbles always have a very well defined mean velocity, but with considerable variations. When these variations are confined locally, and when the mean velocity has a very small global variance and is always in one direction, we have unidirectional flow. For such conditions, a probe oriented at $\theta = 180°$ would miss almost all bubbles, since the fiber and the metal sheathing aligned with the main flow direction would block them from ever reaching the tip.

Bubbly flows

Figures 2.8 and 2.9 show the gas holdups and bubble counts obtained at various impact angles for the two bubbly flow conditions we investigated. The results reveal a similar pattern to that of 'unidirectional' flow (a nearly constant gas holdup from impact angles of 0° to 90°, followed by

a decrease for impact angles of 90° to 180°). Nevertheless, there are two noticeable differences: the magnitudes of the (standard) deviations for gas holdups and the degree of gas phase holdup measured by the probe oriented at θ = 180° (compared to what was measured at θ = 0°) were higher in the two bubbly flow conditions. For the stirred tank, the gas holdups and bubble counts measured at θ = 180° were 57% and 60% of those measured at θ = 0°, respectively; for the sparged tank, the ratios were 50% and 75%, respectively. These results suggest a higher degree of bubble trajectory deviation from the main flow direction in the bubbly flow conditions.

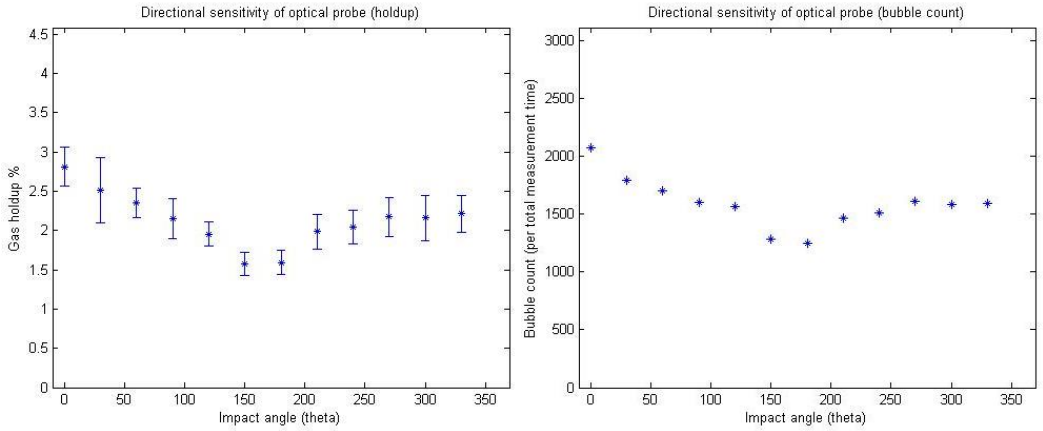

Figure 2.8: Measured gas holdups and bubble counts at various impact angles for bubbly flow in the stirred tank.

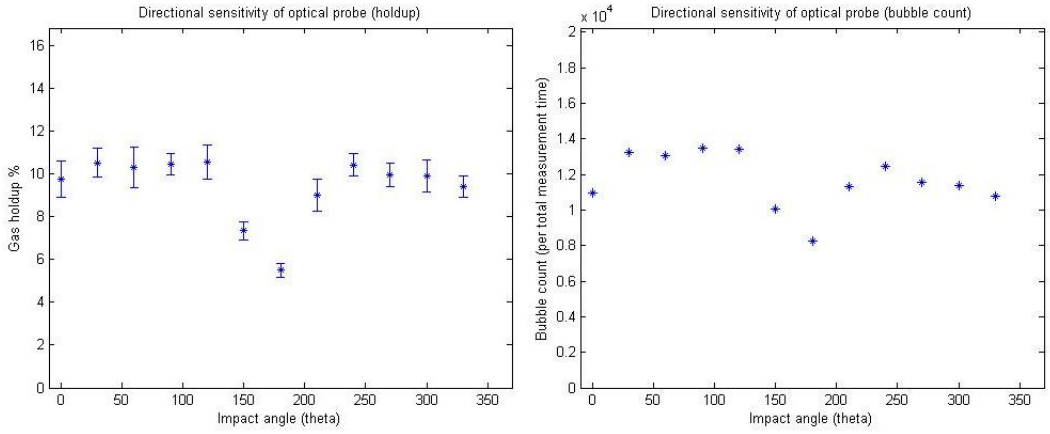

Figure 2.9: Measured gas holdups and bubble counts at various impact angles for bubbly flow in the sparged tank.

2.2.3. The Optical Probe Probabilistic Model (OPPM) and constitutive equations

As mentioned previously, the magnitude of our optical probes' directional sensitivity, as well as that of other 'needle-like' techniques, depends on various attributes, such as the exact probe tip geometry, curvatures of moving interfaces, evolution of the interface profiles, angle of attack with respect to the tip, etc., most of which are not available *a priori*. Rather than a detailed theoretical analysis of case-by-case piercing mechanisms that would involve additional assumptions, this section provide a robust model that can be extended to all other 'needle-like' probes.

Cone of acceptance angle

Our model is based on one assumption regarding the acceptance angle cone: all bubbles, i.e., interfaces, travelling within the impact angle of 90°, or the acceptance angle (β) of 180°, are successfully captured by the optical probe, while only a fraction of the bubbles travelling at larger angles are captured by the probe. Pictorially, this is represented in Figure 2.10.

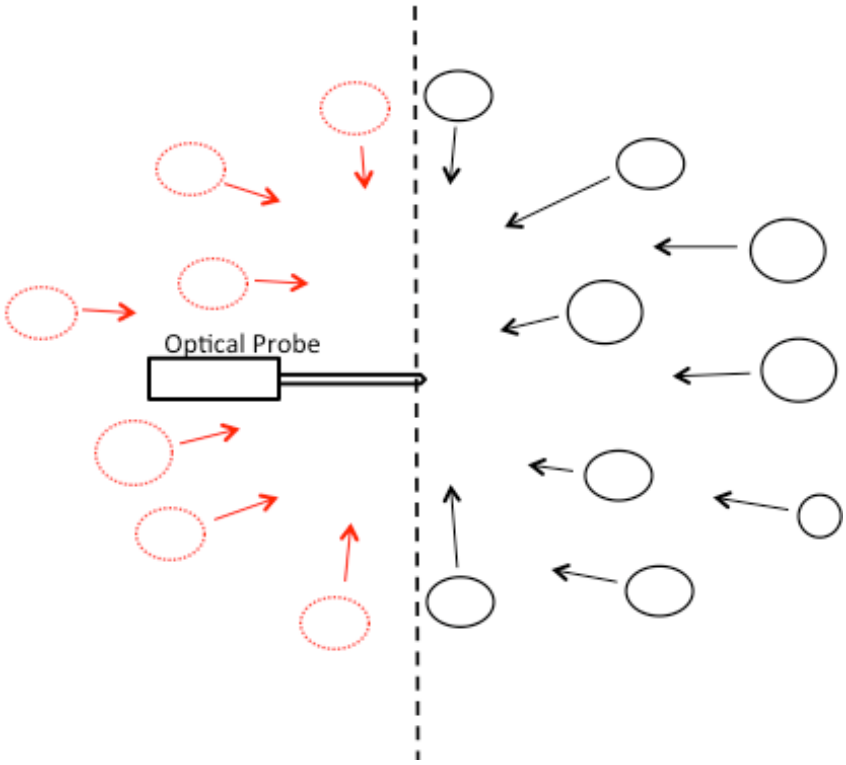

Figure 2.10: An optical probe (‘needle-like’ probe) in a gas-liquid system with bubbles moving in various directions. Black, solid circles represent bubbles moving from the right to the left ($\beta \leq 180°$) with respect to the probe tip orientation. Red, dashed circles represent bubbles moving from the left to the right ($\beta > 180°$) with respect to the probe tip orientation. We assume: all bubbles (interfaces) traveling from right to left are detected by the probe, whereas only a fraction of those travelling from the left to right are detected.

Since the probe tips we used are much smaller (105µm core diameter, detection area ~ 10µm) than typical bubble sizes observed in standard temperature and pressure gas-liquid systems, our assumption can be represented in terms of near-flat bubble interfaces approaching the probe tip, as shown in Figure 2.11.

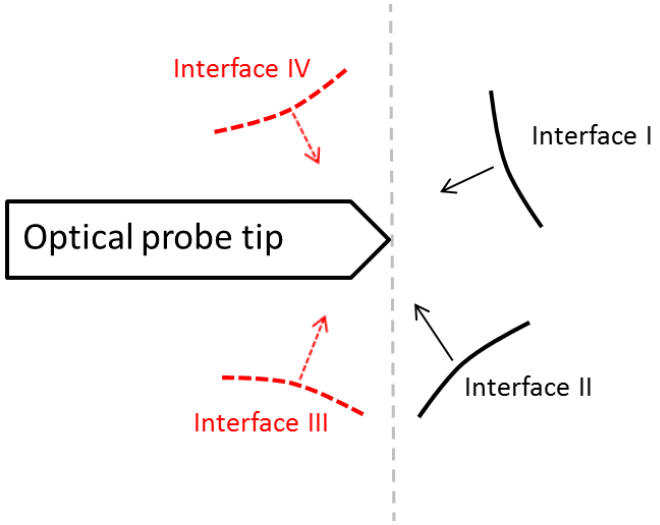

Figure 2.11: Gas-liquid interfaces (bubbles) approaching the optical probe tip from various directions. Black, solid lines represent interfaces moving from right to left ($\beta \leq 180°$). Red, dashed lines represent interfaces moving from the to the ($\beta > 180°$).

According to our assumption, all interfaces travelling within $\beta \leq 180°$ shown in Figure 2.11 (and therefore bubbles in Figure 2.10), i.e., interfaces I and II, are successfully detected by the probe, whereas only a fraction of interfaces traveling at $\beta > 180°$, i.e., interfaces III and IV, are detected. Two of the most likely mechanisms which cause such behavior include: 1) significant interface-probe interaction which causes certain bubbles traveling at $\beta > 180°$ to move away from the detection area, and 2) the inability of the probe tip to pierce small travelling at $\beta > 180°$. According to this assumption, when not employed in a unidirectional flow region, the optical probe technique always can underestimate the true local gas phase holdup and bubble count.

Probabilistic description of gas phase dispersions and the model

Analysis of our collected optical measurements in the frequency domain revealed chaotic bubble occupancy for all positions and conditions investigated, i.e., no distinct frequency was found. No noticeable auto- or cross-correlations were observed, and the likelihood (probability) of a bubble

occurrence was statistically independent for measurements collected at different orientations (θ). Figure 2.12 shows the joint probabilities of gas phase occupancy, i.e., local gas phase holdup, for the signal taken at θ = 0° and all other θ's for the bubbly flow condition we investigated in the sparged tank. All joint probabilities were essentially equal to the product of the corresponding individual probabilities, a necessary condition for two events being statistically independent. The same relationship was found for two other flow conditions we investigated.

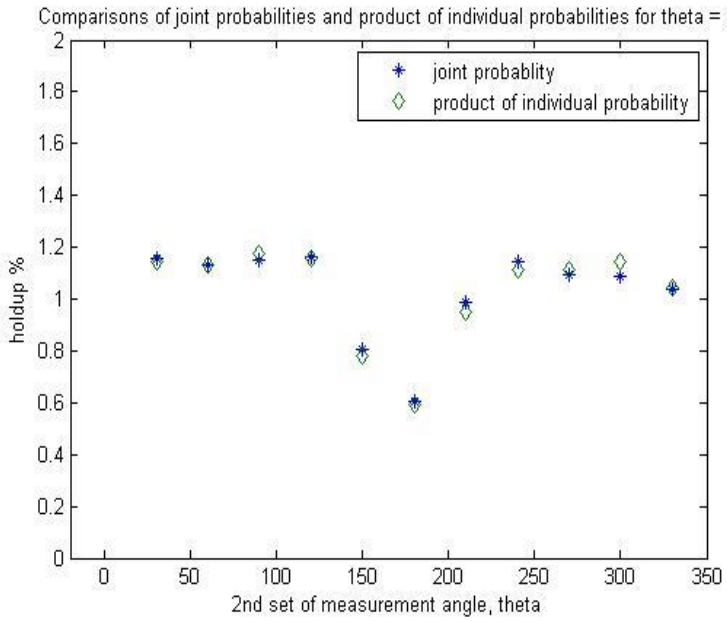

Figure 2.12: The joint probabilities of gas phase occupancy at θ = 0° and all other θ's, and the product of the gas phase occupancy at θ = 0° and all other θ's. Results are from bubbly flow investigated in the RT tank.

Based on these results and our assumption for the acceptance angle cone, we formulated a probabilistic model that separates directional contributions of bubbles from the local gas phase holdup and bubble count, as shown in Equations 2.2 through 2.5. The model separates the contributions to the local gas holdup and bubble count (number of interface boundaries detected)

from bubbles traveling in opposite directions, e.g., from left to right and right to left. Figure 2.13 schematically represents the introduced variables.

$$P_A = P(1) + x_1 \cdot P(2) - x_1 \cdot P(1) \cdot P(2) \quad (2.2)$$

$$P_B = P(2) + x_2 \cdot P(1) - x_2 \cdot P(1) \cdot P(2) \quad (2.3)$$

$$N_A = N(1) + x_1 \cdot N(2) \quad (2.4)$$

$$N_B = N(2) + x_2 \cdot N(1) \quad (2.5)$$

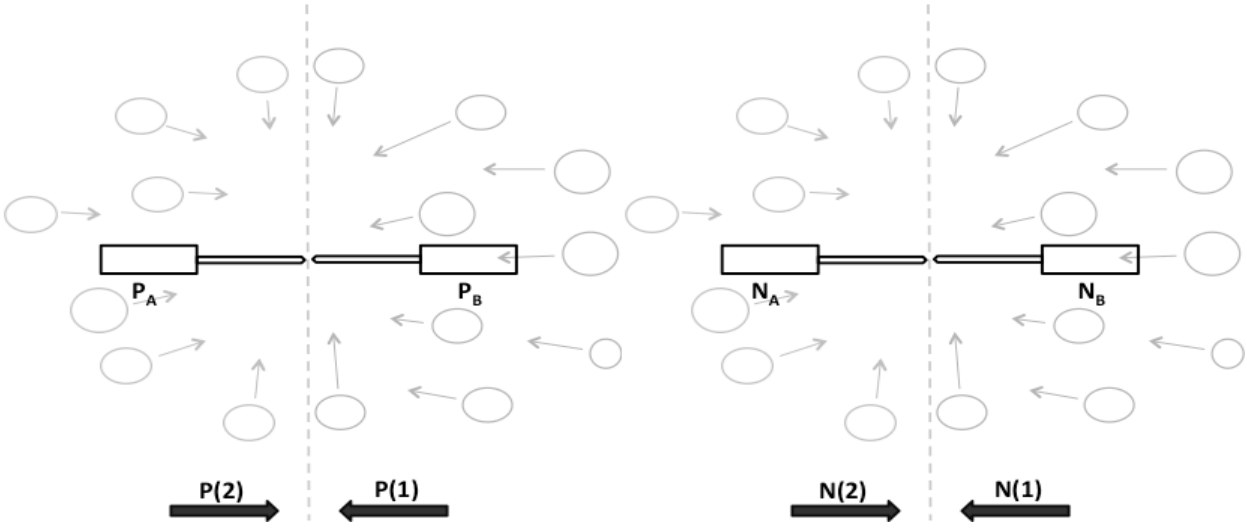

Figure 2.13: Introduced variables for OPPM.

In Equations 2.2 through 2.5, P_A and P_B represent the measured probability of gas occupancy for a probe tip oriented in one of two opposite directions; $P(1)$ and $P(2)$ represent the directional probabilities of gas phase holdup due to bubbles travelling towards either probe tip A or B within $\beta \leq 180°$; N_A and N_B represent the number of interface boundaries (bubble counts) detected by either probe tip A or B; $N(1)$ and $N(2)$ represent the number of interfaces travelling towards

either probe tip A or B within $\beta \leq 180°$; and x_1 and x_2 represent the fraction of the gas phase holdup and number of interfaces detected by a probe tip for bubbles traveling at angles larger than the cone of acceptance angle, $\beta > 180°$.

Because P_x and N_x measured by the probe have different statistical properties, the two sets of equations (Equations 2.2 & 2.3 and Equations 2.4 & 2.5) result in two additional terms for the first set ($x_1 \cdot P(1) \cdot P(2)$ for Equation 2 and $x_2 \cdot P(1) \cdot P(2)$ for Equation 3). By the definition of local gas holdup in our algorithms, the measure of gas phase occupancy probability (local gas phase holdup, P_x) is not mutually exclusive, i.e., bubbles travelling from two opposite directions ($P(1)$ and $P(2)$) can occupy the same point in space simultaneously and contribute to the local gas phase holdup. For bubble counts, this is not the case, as the signal rise from the passing of an interface at the probe tip can be due only to one interface, thus N_x is mutually exclusive.

The third set of equations needed to solve for the six unknown parameters, $P(1), P(2), N(1), N(2), x_1$, and x_2, uses the ratio between the two parameters $P(x)$ and $N(x)$, $\frac{P(x)}{N(x)}$, which represents the average amount of time spent by a bubble at a local reactor space (Equation 2.6).

$$\frac{P(x)}{N(x)} = \frac{\frac{total\ amount\ of\ time\ spent\ in\ gas\ phase\ for\ bubbles\ traveling\ in\ x-direction}{total\ measurement\ time}}{\frac{total\ number\ of\ bubbles\ (interfaces)\ traveling\ in\ x-direction}{total\ measurement\ time}} =$$

$$\frac{total\ amount\ of\ time\ spent\ in\ gas\ phase\ for\ bubbles\ traveling\ in\ x-direction}{total\ number\ of\ bubbles\ (interfaces)\ traveling\ in\ x-direction}. \qquad (2.6)$$

As shown in Figure 2.14, this ratio is highly direction-dependent since it is a function of local flow properties that include the bubble velocity, travel direction, and size distribution.

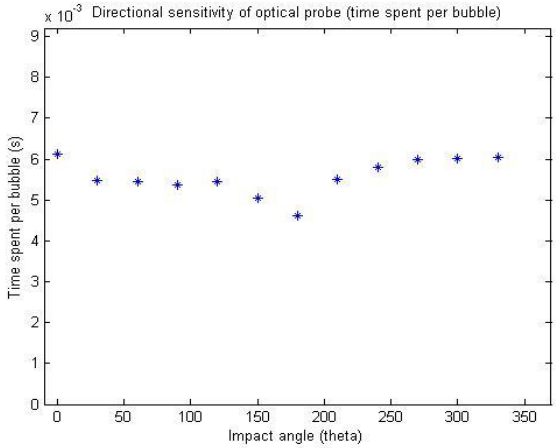

Figure 2.14: The average amount of time spent per bubble (at the detection space) for the bubbly flow condition in the sparged tank region where our probes were employed. Similar profiles were observed for the two other operating conditions.

By assuming these measured ratios are equivalent to the weighted average of the two ratios for two bubble populations travelling in opposite directions, Equations 2.7 and 2.8 can be formulated:

$$\frac{P_A}{N_A} = \frac{\frac{P(1)}{N(1)} + x_1 \frac{P(2)}{N(2)}}{1 + x_1} \tag{2.7}$$

$$\frac{P_B}{N_B} = \frac{\frac{P(2)}{N(2)} + x_2 \frac{P(1)}{N(1)}}{1 + x_2}. \tag{2.8}$$

Along with Equations 2.2 to 2.5, Equations 2.7 and 2.8 can now be used to solve for the six unknown parameters, from which the true (unbiased) local gas phase holdups and bubble counts can be obtained via Equations 2.9 and 2.10. Moreover, the local gas phase dispersion can be separated based on two bubble movement directions.

$$Gas\ holdup_{true,unbiased} = P(1) + P(2) - P(1) \cdot P(2) \tag{2.9}$$

$$Bubble\ count_{true,unbiased} = N(1) + N(2) \tag{2.10}$$

2.2.4. Results

There are several points within the range of possible solutions where our constitutive equations (Equations 2.2 to 2.5, 2.7, 2.8) become underdetermined, e.g., $x_1, x_2 = 0$, or ill-posed, e.g., $N(1) = N(2)$. To avoid these points, the ranges of possible solutions listed in Table 2.2 were included as part of the algorithm. The ranges were determined based on an assumption that the higher the gas holdups and bubble counts measured by the probe (compared to a probe oriented in the opposite direction), the more likely the bubbles will travel in that direction and the higher the fraction of backflow (bubbles traveling at $\beta > 180°$) detected by the probe.

Table 2.2: Restricted ranges of values for the OPPM.

Variables	Range
$\boldsymbol{P(1)}$	$P_B < P(1) \leq P_A$, if $P_A \geq P_B$ $0.1 \cdot P_\mathrm{A} < P(1) \leq P_\mathrm{A}$, if $P_A < P_B$
$\boldsymbol{P(2)}$	$0.1 \cdot P_B < P(2) \leq P_B$, if $P_A \geq P_B$ $P_A < P(2) \leq P_B$, if $P_A < P_B$
$\boldsymbol{N(1)}$	$N_B < N(1) \leq N_A$, if $N_A \geq N_B$ $0.1 \cdot N_\mathrm{A} < N(1) \leq N_\mathrm{A}$, if $N_A < N_B$
$\boldsymbol{N(2)}$	$0.1 \cdot N_B < N(2) \leq N_B$, if $N_A \geq N_B$ $N_A < N(2) \leq N_B$, if $N_A < N_B$
$\boldsymbol{x_1}$	$\frac{N_B}{N_A} < x_1 \leq 1$, if $N_A \geq N_B$ $0.1 \cdot \frac{N_\mathrm{A}}{N_\mathrm{B}} < x_1 \leq \frac{N_\mathrm{A}}{N_\mathrm{B}}$, if $N_A < N_B$
$\boldsymbol{x_2}$	$0.1 \cdot \frac{N_B}{N_A} < x_2 \leq \frac{N_B}{N_A}$, if $N_A \geq N_B$ $\frac{N_\mathrm{A}}{N_\mathrm{B}} < x_2 \leq 1$, if $N_A < N_B$

Approximate unidirectional flow

Figures 2.15, 2.16, and 2.17 respectively show the unbiased local gas phase holdups obtained via Equation 2.9, the magnitudes of dispersions that have been separated into contributions from various directions, and the fractions of backflow (bubbles traveling at $\beta > 180°$ of the probe tip) detected by the optical probe. Since our model requires at least one set of measurements composed of two optical probe measurements taken from tips facing in opposite directions, these figures represent results combined from six measurement sets: 0°-180°, 30°-210°, 60°-240°, 90°-270°, 120°-300°, and 150°-330°.

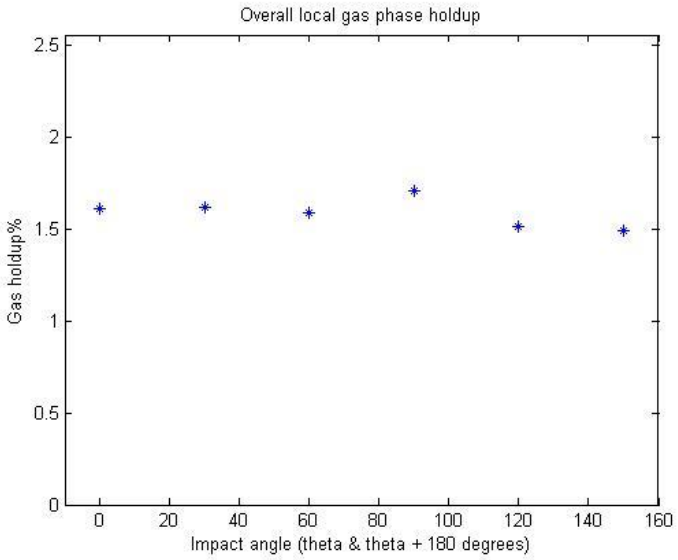

Figure 2.15: Unbiased local gas phase holdups in a 'unidirectional' flow in the stirred tank. Results from six measurement sets.

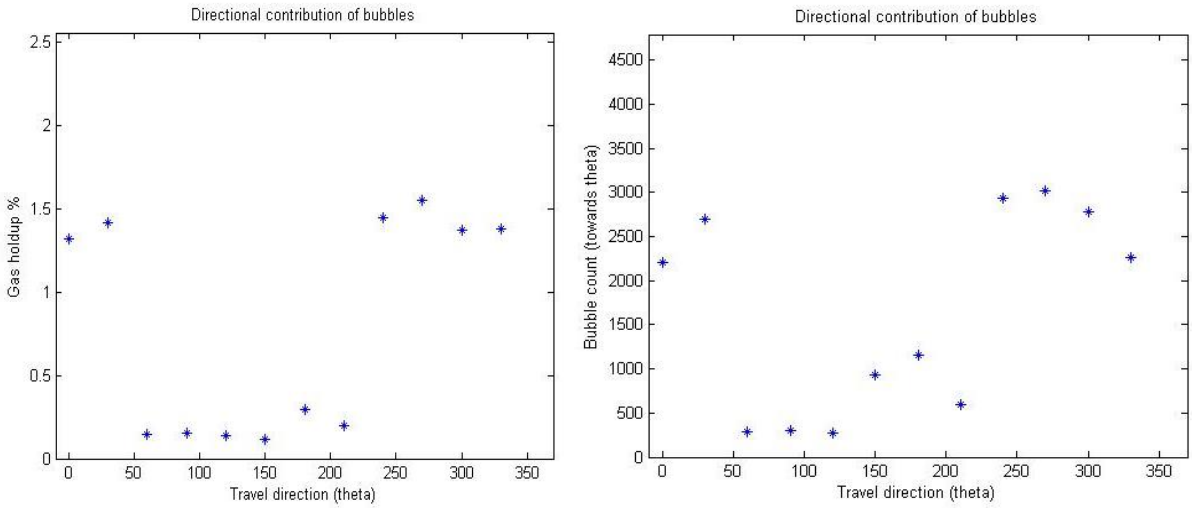

Figure 2.16: Degree of contribution to the overall local gas phase holdup and bubble count within $\beta \leq 180°$ of θ in a unidirectional flow in the stirred tank.

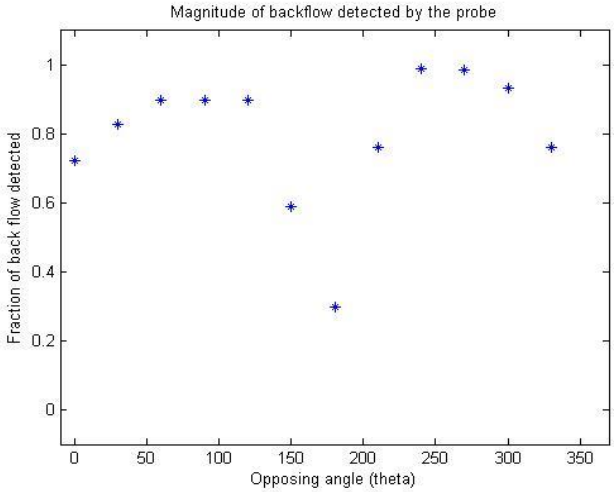

Figure 2.17: Fraction of backflow detected by the optical probe in a 'unidirectional' flow in the stirred tank.

The unbiased local gas phase holdups obtained via Equation 2.9 confirm the validity of our constitutive equations and the assumptions for the 'unidirectional' flow conditions. For all six sets of measurements, the unbiased local gas phase holdups were found to be equal to each other, with a mean value of 1.69% and a standard deviation 0.08%, and directional sensitivity was not observed. Optical probe measurements collected within $\theta = \pm 90°$ were found to be within the

measurement error (standard deviation) of the unbiased local gas holdup, suggesting the optical probe technique's usefulness when positioned at 'proper' orientations. These results are also in agreement with what was previously suggested by Mueller (2009) and Mueller and Dudukovic (2010), who came to their conclusion after comparing their results with those from non-invasive techniques: 1) For an accurate measurement of gas phase holdup via optical probe technique, one must obtain at least two measurements with tips oriented in opposite orientations and report the larger gas holdup of the two, and 2) It is best to have the probe oriented facing the flow direction for regions where the main flow directions are known. The unbiased bubble counts were also nearly equal to each other for all six measurement sets.

The magnitudes of directional contributions to the local gas phase holdups and bubble counts were found to be near their maxima for bubbles traveling within $\beta \leq 180°$ of angles proximate to $\theta = 0°$, i.e., $\theta = 0°$, 30°, 240°, 270°, 300°, and 330° (Figure 2.16). The gas phase holdup contributions from bubbles traveling towards the probe tips oriented at $60° \leq \theta \leq 210°$ (within $\beta \leq 180°$ of them) were found to be less than 0.3%, but still significant (18.9% of the unbiased local gas phase holdup), suggesting that even for a seemingly unidirectional flow, there exists a small number of bubbles that deviate greatly from the main flow direction, possibly due to velocity fluctuations caused by eddies of different sizes. These bubbles are most likely travelling at $\theta \approx 330°$ (-35°), because near constant contributions were observed for $\theta = 0°$, 30°, 240°, 270°, 300°, and 330°. Further investigation and analysis are necessary for a firmer conclusion.

The profile for the degree of backflow detected by the probe (Figure 2.17) closely resembles the gas holdup and the bubble count profiles shown in the previous section (Figure 2.7). The fraction of backflow reached a near maximum value at angles proximate to $\theta = 0°$, decreased as θ

increased up to θ = 180°, reached its minimum value at θ = 180°, and increased as θ increased up to θ = 360° (0°). This profile is consistent with the definition of θ and our understanding of the mechanisms responsible for underestimation of gas phase dispersion when the probe is oriented in 'improper' directions: The larger the θ (up to 180°), the more likely the probe will interfere with bubbles travelling along the main flow direction and keep them from ever reaching and being pierced by the probe tip.

Bubbly flows

Figures 2.18, 2.19, and 2.20 respectively show the unbiased local gas phase holdups, the magnitudes of dispersions that have been separated into contributions from various directions, and the fractions of backflow (bubbles traveling within β > 180° of the probe tip) detected by the optical probe for the two bubbly flow conditions we investigated.

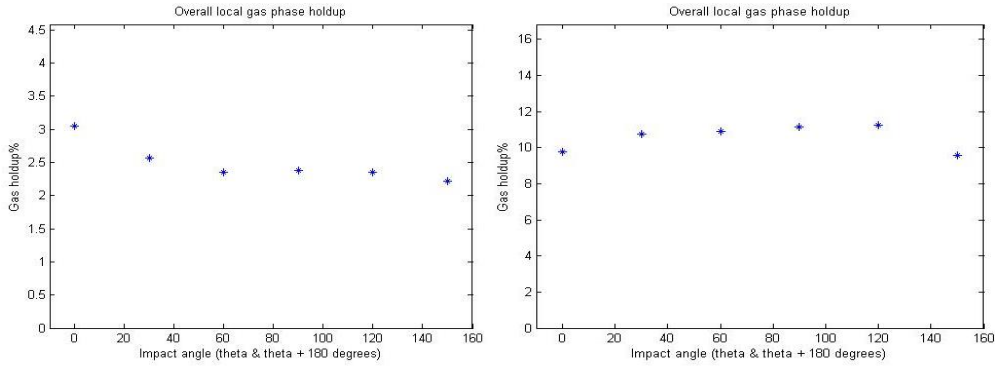

Figure 2.18: Unbiased local gas phase holdups. Results from six measurement sets. Left, bubbly flow condition in the stirred tank; right, bubbly flow condition in the sparged tank.

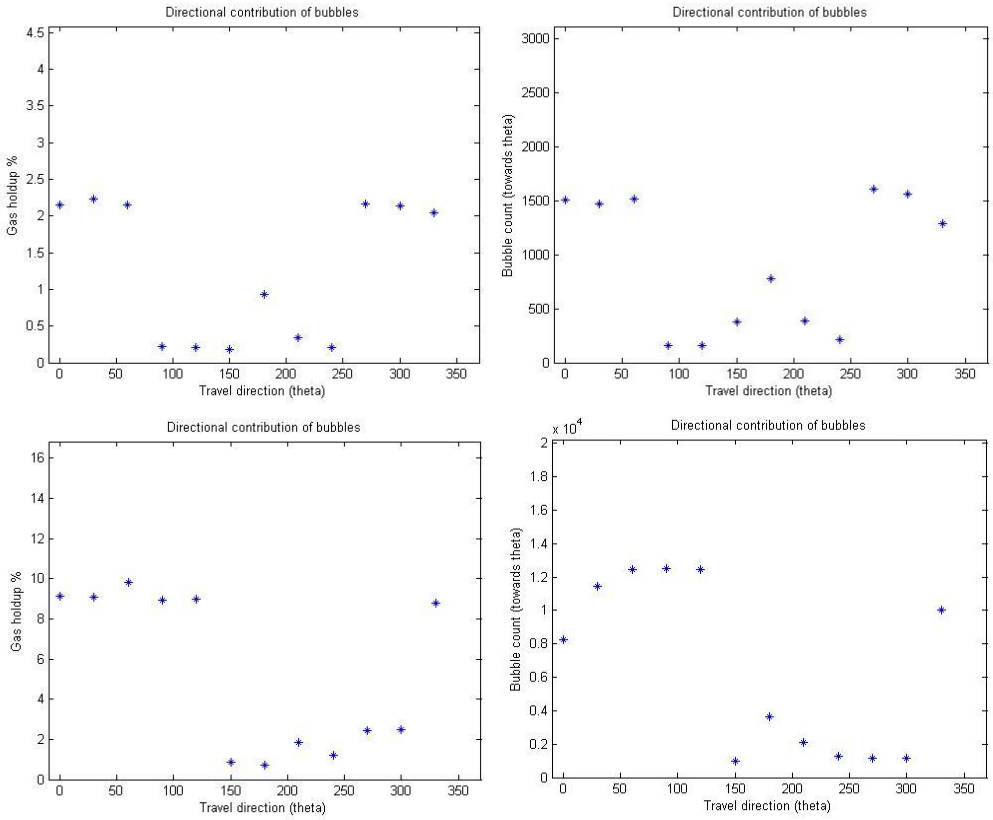

Figure 2.19: Degree of contributions to the overall gas phase holdup (left) and bubble count (right) within $\beta \leq 180°$ of θ. Upper figures, bubbly flow condition in the stirred tank; lower figures, bubbly flow condition in the sparged tank.

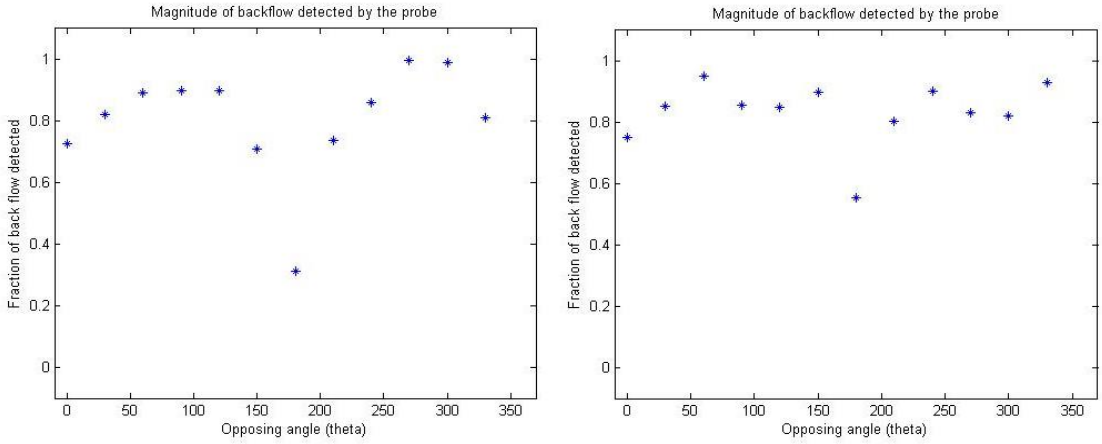

Figure 2.20: Fraction of backflows detected by the optical probe. Left, bubbly flow condition in a stirred tank; right, bubbly flow condition in the sparged tank.

As was the case for the 'unidirectional' flow, the unbiased local gas holdups validated our constitutive equations and the assumptions for the bubbly flow conditions. For the stirred tank, the unbiased local gas holdup was found to be 2.49%, with a standard deviation of 0.30%; for the sparged tank, the unbiased local gas holdup was found to be 10.57%, with a standard deviation of 0.71% (Figure 2.18). These values were once again well within the range of optical probe measurements collected within $\theta = \pm 90°$, suggesting the guideline provided by Mueller and Dudukovic (2010) may still be applied in bubbly flow conditions. The unbiased bubble counts were also found to be well within each measurement's range.

For the bubbly flow conditions, the majority of the local gas holdup was found to be due to bubbles traveling along the main flow directions (Figure 2.19). Contributions from bubbles traveling against the main flow direction, $\beta \leq 180°$ of $\theta = 180°$, were found to be 30% and 7% of the unbiased local gas phase holdup for the two bubbly flow conditions in the stirred tank and the sparged tank, respectively.

The fraction of the backflow detected by the probe (Figure 2.20) closely resembled the gas holdup and the bubble count profiles (Figures 2.8 and 2.9). The fractions were near their maximum value of 1 at angles proximate to 0°, decreased as θ increased up to 180°, reached their minimum value at $\theta = 180°$, and increased as θ increased back up to $\theta = 360°$ (0°).

Flow with large recirculation (2-D bubble column)

Comparisons between the results from the OPPM and HSC also validated the model and the assumptions involved. The experimental setup and the results obtained from the HSC and the OPPM are shown in Figure 2.21 and Table 2.3, respectively.

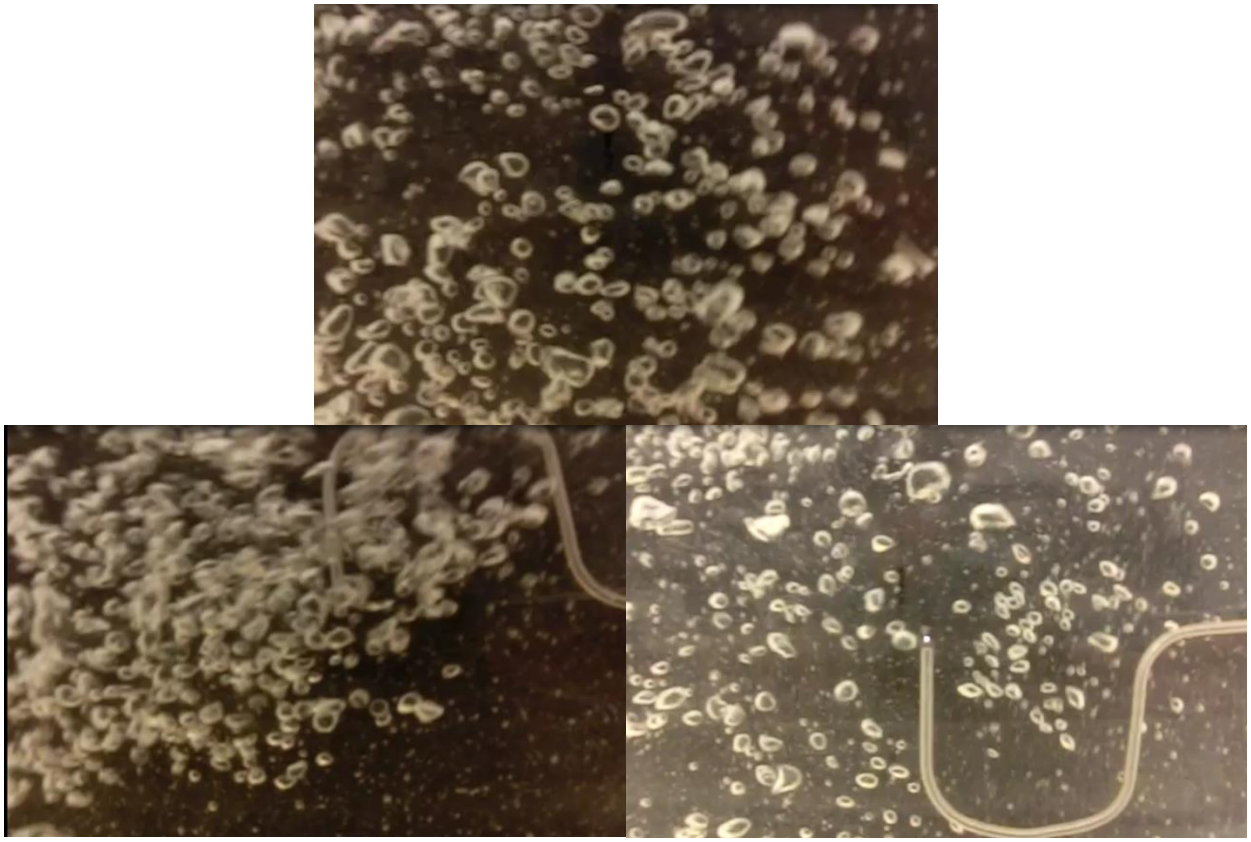

Figure 2.21: 2-D bubble column with and without the optical probe. Top, without optical probe; bottom, with optical probe.

Table 2.3: Comparitive results from OPPM and HSC.

	Without probe (HSC)	**With probe pointing down (HSC)**	**With probe pointing up (HSC)**	**OPPM**
Gas holdup ratio (bubble up / bubble down)	2.12	1.99	2.20	1.81 ± 0.46

For each HSC result, ~ 43,000 images were analyzed on a frame-by-frame basis and the gas-holdup due to bubbles traveling in opposing directions was quantified. The ratios in Table 2.3 therefore represent the ratios between the local gas holdups contributed by gas phase bubbles traveling up and down ($\frac{\%}{\%}$). For the OPPM results in Table 2.3, the optical probe data collected

for 691.2 seconds was further broken down into five segments (172.8 seconds / segment) for a better comparison between the HSC and the OPPM with respect to time scales.

The visually observed time-averaged local gas holdups were found to be significantly lower than the results obtained from the OPPM. This difference arose because of the finite thickness of the column, despite being named a 2-D bubble column, and the optical probe's inability to capture all bubbles that are accounted for by the HSC.

2.3. Conclusions

This chapter introduced a probabilistic model that corrects for the directional sensitivity of the optical probe technique. The model uses the chaotic nature of the optical probe measurement signals to interpret the measured signals in terms of probability. The model is based on two assumptions. First, all bubbles traveling within the acceptance angle (β) of 180° are successfully captured by the probe. Second, the ratio between the two measured parameters, $\frac{P(x)}{N(x)}$, which represents the average amount of time spent by a bubble at a local reactor space, is a unique property of bubbles traveling in different directions. Application of the model enables separating the contributions of bubbles travelling in different directions to the overall local gas phase holdup and bubble counts. To solve for the six parameters associated with the model, at least two measurements, collected with the probe tips oriented in opposing directions, are needed.

For all three flow conditions we investigated in the stirred and the sparged tanks (one 'unidirectional' flow and two bubbly flow conditions), the majority of the 'unbiased' gas phase holdup was contributed by bubbles traveling within $\beta \leq 180°$ of the main flow direction, i.e., $\theta = 0°$. For the 'unidirectional' flow condition, approximately 81% of the unbiased local gas phase

holdup was due to bubbles traveling within $\beta \leq 180°$ of $\theta = 0°$. For the two bubbly flow conditions, 70% and 93% of the 'unbiased' local gas phase holdup was found to be due to bubbles traveling within $\beta \leq 180°$ of the main flow direction for the stirred tank and the sparged tank, respectively. No clear distinction was observed between the two flow conditions in terms of directional contribution.

Comparisons between the OPPM and HSC results made in the 2-D bubble column confirmed the validity of the constitutive equations and the assumptions associated with them. Despite the column being named a 2-D bubble column, the finite thickness of the column and optical probe's property to giving only local point measurements resulted in HSC giving a significantly higher gas holdup values.

Significant underestimation, i.e., data bias, of the local gas holdup and bubble counts could result from the optical probe measurements if the probe is oriented in the 'wrong' directions, i.e., $\theta > \pm 90°$. The suggestion previously made by Mueller (2009) and Mueller and Dudukovic (2010), regarding the need for at least two measurements with the probe tip oriented in opposite directions, was found to be effective for all flow conditions we investigated.

The introduced model, for the first time, can provide detailed bubble history information in terms of gas phase holdup and bubble counts. Implementation of the model in multiphase reactors is expected to be very useful for developing scale-up and reactor modeling, because the information on bubble history helps us determine which reactor model to use for the gas phase hydrodynamics. Moreover, the model can help us quantify baffle and sparger effects very near and far from these features.

Chapter 3. Measurements of gas phase backmixing in bubble column reactors

Bubble column reactors provide an effective way for contacting gas-liquid or gas-liquid-solid phases. In a conventional setup, gas is introduced at the bottom of the reactor through a sparger and the liquid (bubble column reactor) or liquid-solid medium (slurry bubble column reactor). Both the dispersed phase (gas phase) and the continuous phase (liquid or liquid-solid medium) can operate in the continuous mode. Figure 3.1 shows the general schematic of the reactor setup.

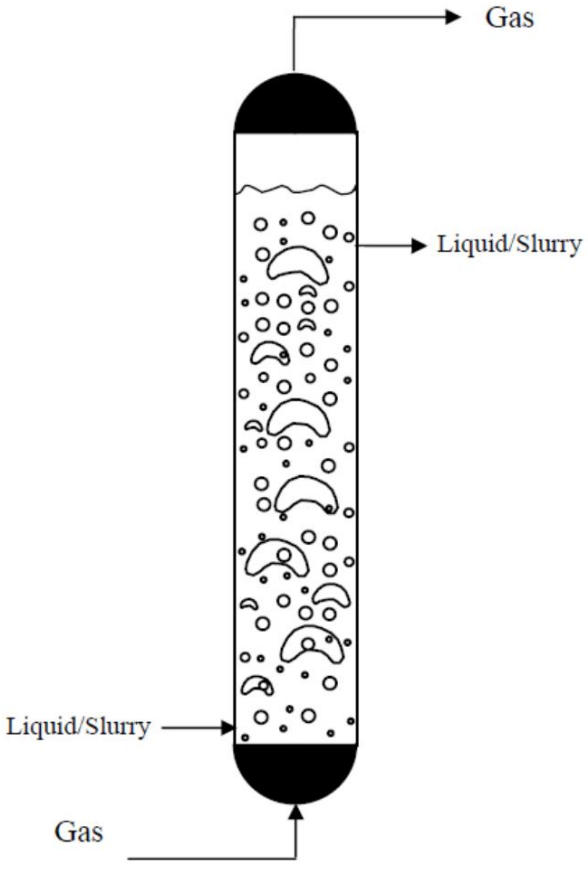

Figure 3.1: Bubble column reactor (source: Chen, 2004).

Bubble column reactors possesses numerous advantage, including good heat and mass transfer characteristics, simplicity in setup, and lack of moving parts. Many industrial process rely on them; for example, in the chemical and petrochemical industries, bubble column reactors have been used for partial oxidation of ethylene to acetaldehyde, wet-air oxidation, and liquid phase methanol synthesis. In the biochemical industry, they have been used for cultivation of bacteria and mold fungi, and treatment of sewage (Hamed, 2012).

3.1. Hydrodynamic flow regimes in bubble column reactors

Youssef (2010) noted that important parameters that affect the hydrodynamics and performance of bubble column reactors are the degree of local and global backmixing, which depend on local and global gas holdup; bubble velocity; gas-liquid interfacial area; bubble size distribution, bubble passage frequency; and mass and heat transfer. Youssef (2010) also noted that these parameters, in turn, depend on many operating variables, including the volumetric flow rate, column geometry, sparger design, presence of internals, and physicochemical properties of the reactants and the products. Measuring or accurately determining based on theory all these parameters at the needed time and length scales is not possible, so simplifying assumptions and correlations have been developed and utilized.

For practical purposes, the concept of the hydrodynamic flow regime has been utilized to extend the developed assumptions and correlations. Five distinct flow regimes in bubble columns hve been identified, namely the homogeneous (bubbly), transition, heterogeneous (churn-turbulent), slug, and annular flow regimes (Figures 3.2 and 3.3).

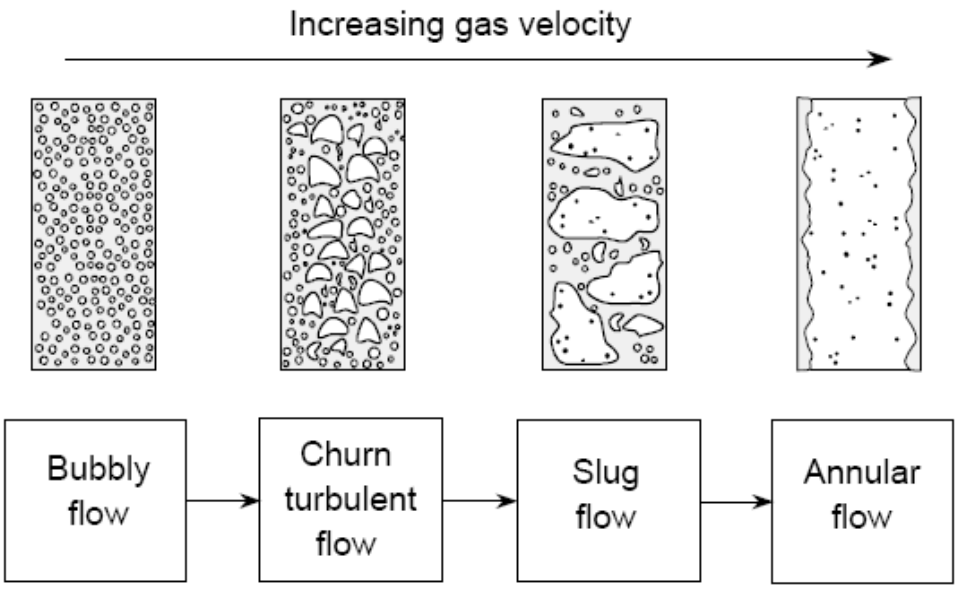

Figure 3.2: Flow regimes observed in bubble columns (source: Al-Dahhan, 2006).

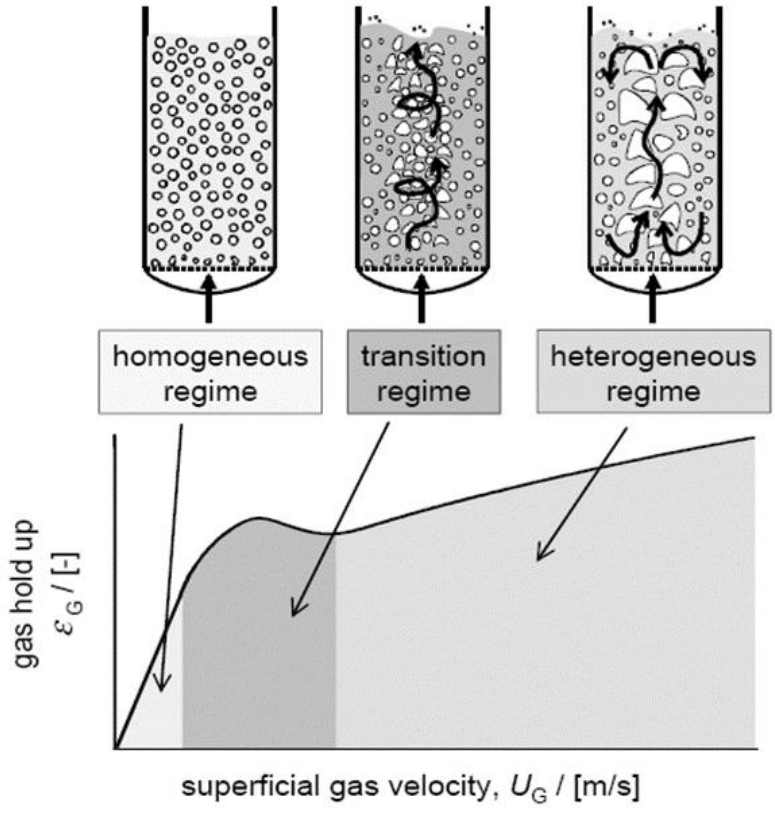

Figure 3.3: Flow regimes classification based on overall gas holdup profile (source: Al-Dahhan, 2006).

Flow regime can be identified by visual observation, studying the evolution of the overall gas holdup, measuring temporal characteristics of predominant hydrodynamic parameters, and employing other advanced measurement techniques, such as CT and CARPT (e.g., Letzel et al., 1997; Lin et al., 2001; Buwa and Ranade, 2002; Shaikh and Al-Dahhan, 2007). Several flow regime maps have been drawn for simple reactor setups, e.g., Shah et al. (1982), and these maps have been used as a starting point for detailed hydrodynamic studies.

For air water systems, the slug flow regime has been reported only in reactors with very small diameters. Similarly, the annular flow regime has been reported only at very high superficial gas flow rates. Therefore, for most practical applications, a reactor is operated in either the homogeneous or heterogeneous flow regimes. Figure 3.4 shows photographs of the two flow regimes, and Table 3.1 summarizes the key flow characteristics for these regimes and their applications.

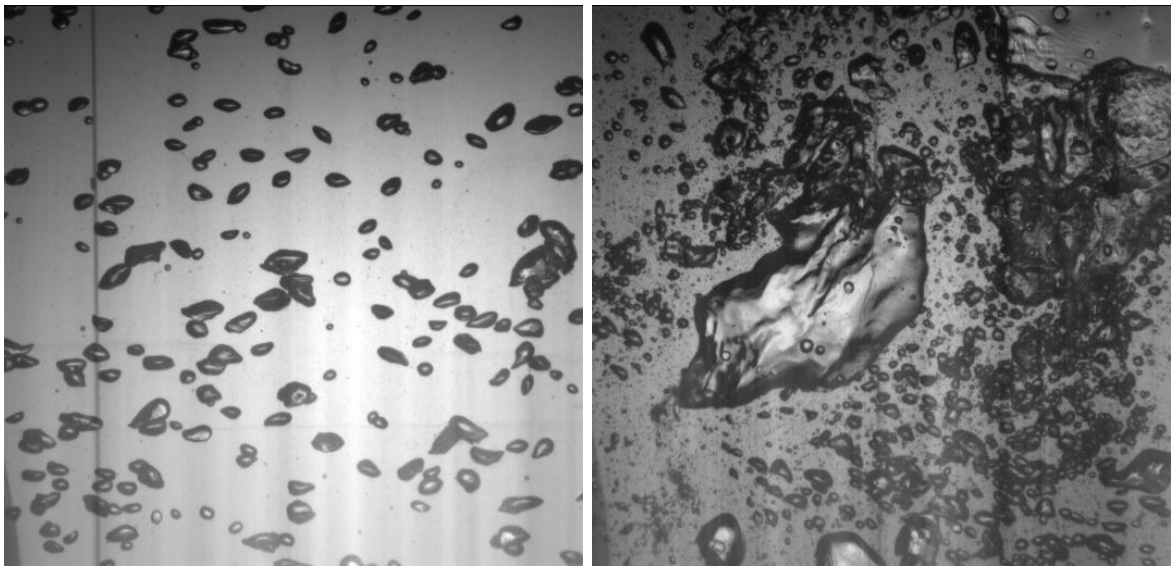

Figure 3.4: Photographic representation of the homogeneous (left) and heterogeneous (right) flow regimes (source: Chen, 2004).

Table 3.1: Homogeneous versus heterogeneous flow regimes
(Chen, 2004; Shaikh and Al-Dahhan, 2007).

	Homogeneous	**Heterogeneous**
Characteristics	• Low gas holdup • Individual ellipsoid bubbles • Narrow bubble size distribution • Negligible bubble-bubble interaction	• High gas holdup • Large irregular voids • Strong bubble-bubble interaction • Wide bubble size distribution • Better heat and mass transfer
Applications	• Most biochemical applications (low stress) • Fermentation • Waste water treatment	• Preferable for highly exothermic processes (liquid phase methanol synthesis, Fischer Tropsch synthesis)

3.2. Advances and challenges in reactor modeling

Despite extensive research, we are still far from being able to model complex fluid dynamics and mixing behaviors based on first principles. Predictive reactor design and modeling mostly rely on the ideal, phenomenological, or compartmental models at the reactor scale. As mentioned, this simplicity acknowledges the complex and irregular intra- and inter-phase forces induced flow patterns and reflects the lack of experimental techniques to capture this behavior, especially under turbulent flow conditions.

Regardless of the approach, the path forward for successful reactor design, modeling, and scale-up requires sound phenomenological descriptions and quantification of backmixing for all phases. Depending on the degree of backmixing, reactor performance, e.g., selectivity, yield, and productivity, change significantly for the complex reaction networks encountered in practical processes. Numerous attempts were thus made in the CREL and elsewhere to measure phase backmixing and incorporate the results in reactor models. Reported studies on gas phase mixing mainly relied on tracer experiments. The results were used to fit the axial dispersion model (ADM) (Han, 2007; Hamed, 2012), variations of ADM (Shetty, 1992), and compartmental models (Gupta, 2002). For the liquid phase mixing, thermal dispersion methods to fit the ADM (Yang and Fan, 2003); the RPT technique to fit the ADM (Han, 2007) and compartmental models (Degaleesan, 1997; Gupta, 2002) were usually employed. For solid (dispersed catalyst) phase, the RPT technique has also been used to fit the sedimentation-dispersion model (Han, 2007). In ADM, the non-ideal behavior of tubular reactors, which differs from the PFR model in the z-direction (axial direction), is quantified using a diffusion-like term, $D_s \frac{\partial^2 C_s}{\partial z^2}$, where D_g is named the axial dispersion coefficient, as shown in Equation 3.1:

$$\frac{\partial C_s}{\partial t} = D_s \frac{\partial^2 C_s}{\partial z^2} - U_s \frac{\partial C_s}{\partial z}. \qquad (3.1)$$

The first term on the left hand side of the equation and the last term on the right hand side represent the time-dependent and the convection-dependent transport terms, respectively. Here, reaction terms are neglected for simplicity. To solve for the axial dispersion coefficient and solve Equation 3.1., either closed-closed (Danckwerts) or open-open boundary conditions are typically used (Fogler, 2006).

In all of the above mentioned works, hydrodynamic behavior for the solid and liquid phases were successfully measured at various length and time scales, and the results were incorporated into the reactor modeling by utilizing the ADM or its variations. The CREL's main contribution has been the development of 1-D and 2-D recirculation models that incorporate the very different flow patterns observed in the core and the annular zones (Degaleesan, 1997; Mudde et al., 1997; Mudde et al., 1998; Gupta, 2002) by compartmentalizing these zones separately. The distinct flow patterns have been reported in the literature for some time, but the introduction of first-principle and turbulence-based reactor models using results from advanced experimental techniques such CARPT and CT provided a clear path towards how local fluid dynamics can be incorporated into bubble column reactor modeling.

For the gas phase, on the other hand, models that take into account only the global reactor hydrodynamic behavior have been developed. Because these models do not consider local hydrodynamic behaviors, their utility for reactor modeling and scale-up remains to be seen. Moreover, an additional assumption regarding the degree of mixing is typically required to interpret global reactor measurements, e.g., residence time distribution (RTD) (Levenspiel, 2002).

A recent surge in CFD modeling (e.g., Krishna et al., 2000; Laborde-Boutet et al., 2010; Yang et al., 2011; Rohair et al., 2011; Hamidipour et al., 2012) has shown promising results; however, direct utilization of CFD modeling for reactor design and modeling still requires considerable work, because most multiphase CFD simulations require extensive validation using proven experimental techniques.

Gas phase modeling

As noted in the introduction, the gas phase dynamics dominate the overall bubble column reactor hydrodynamics due to the much higher volumetric flow rate of gas. Much recent experimental research in CREL therefore has focused on closing the knowledge gap between the gas phase holdups, bubble dynamics measurements, and reactor models (Youssef, 2010; Hamed, 2012; Manjrekar and Dudukovic, 2015). While earlier studies usually modeled the gas phase as being plug flow (the ideal reactor model), more recent research revealed significant deviation from ideal flow (Kumar et al., 1997; Xue, 2004) caused by complex gas phase dynamics that include radial gas phase holdup and wide bubble size distributions.

Figure 3.5 presents some of the most notable models developed thus far. The most common approach has been to quantify the degree of deviation from the plug flow model by adding the axial dispersion term in the transport equation. Despite the lack of experimental techniques that could be used to extract axial dispersion coefficients (such as CARPT for the liquid and solid phases), modeling the gas phase using ADM remains very popular to this day, as noted by Hamed (2012). A more representative description of gas phase backmixing is required at the local and global scale to fully justify ADM usage for gas phase and reactor model development. Furthermore, we need a fundamental description of the entrance and exit zone effects, i.e., how gas phase dynamics and backmixing stay the same or change in these zones, for more representative gas phase modeling (Hills, 1976; Liu, 1993; Warsito and Fan, 2005).

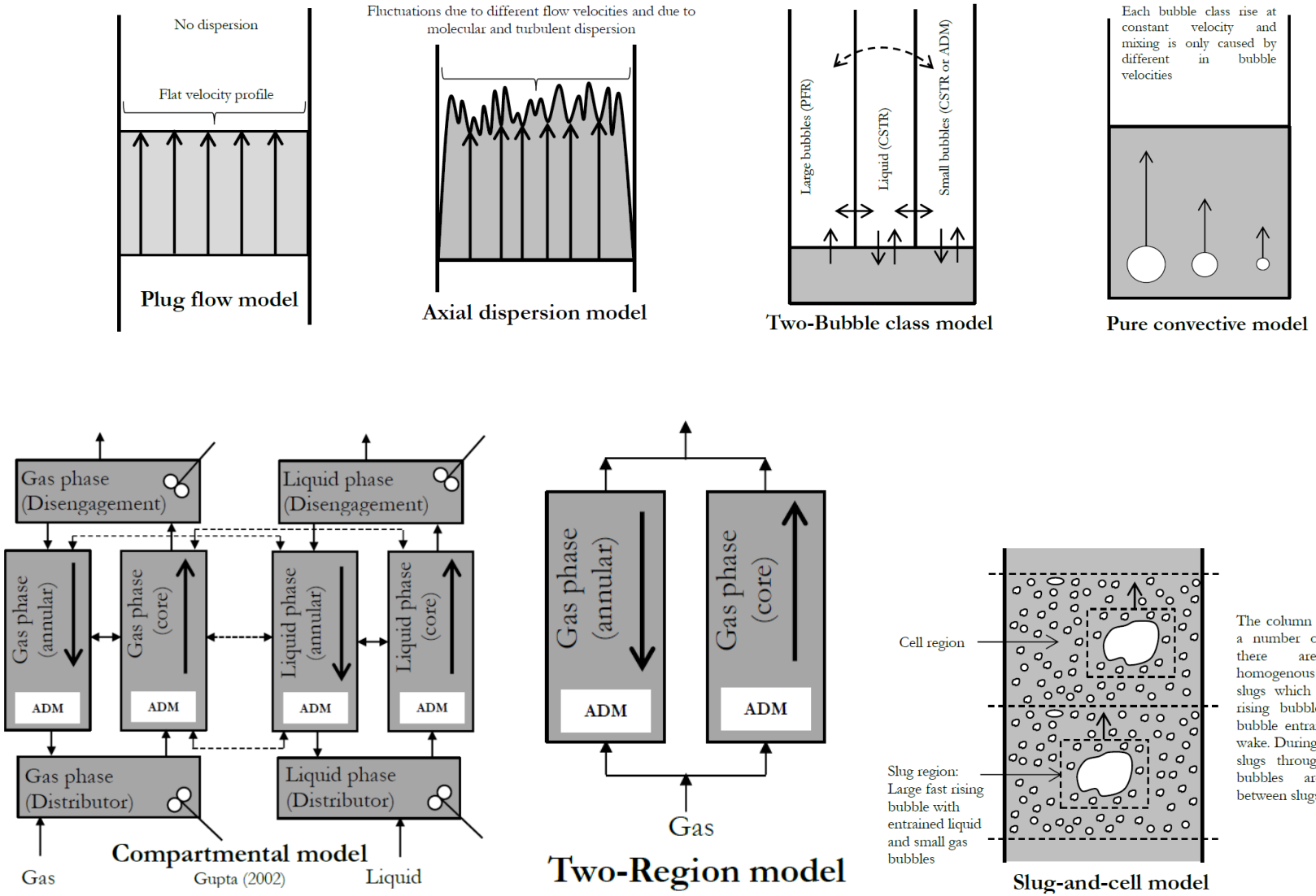

Figure 3.5: Gas phase models in bubble column reactors (source: Hamed, 2012).

3.3. Gas phase backmixing measurements

The Optical Probe Probabilistic Model (OPPM) introduced in Chapter 2 was employed in a lab-scale bubble column reactor at a wide range of operating conditions to enhance our understanding of gas phase backmixing, i.e., the fraction of gas phase traveling back towards the bottom of the reactor. This section summarizes the major findings and discusses the significance of the results.

3.3.1. Experimental setup and the optical probe

A 10-cm diameter bubble column reactor without any internals was investigated. Figures 3.6 and 3.7 show the perforated sparger and the reactor. The gas phase was operated continuously; the liquid phase was operated in a batch mode. Before employing the optical probes and the OPPM, the global reactor gas holdups were first measured using the volume of expansion method to determine the operating conditions at which the flow regimes transitioned.

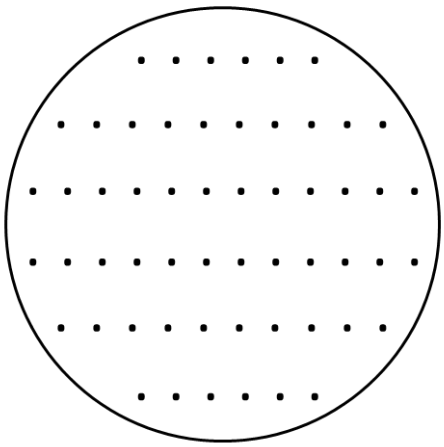

Figure 3.6: Uniform perforated sparger
(small holes, shown not to scale).

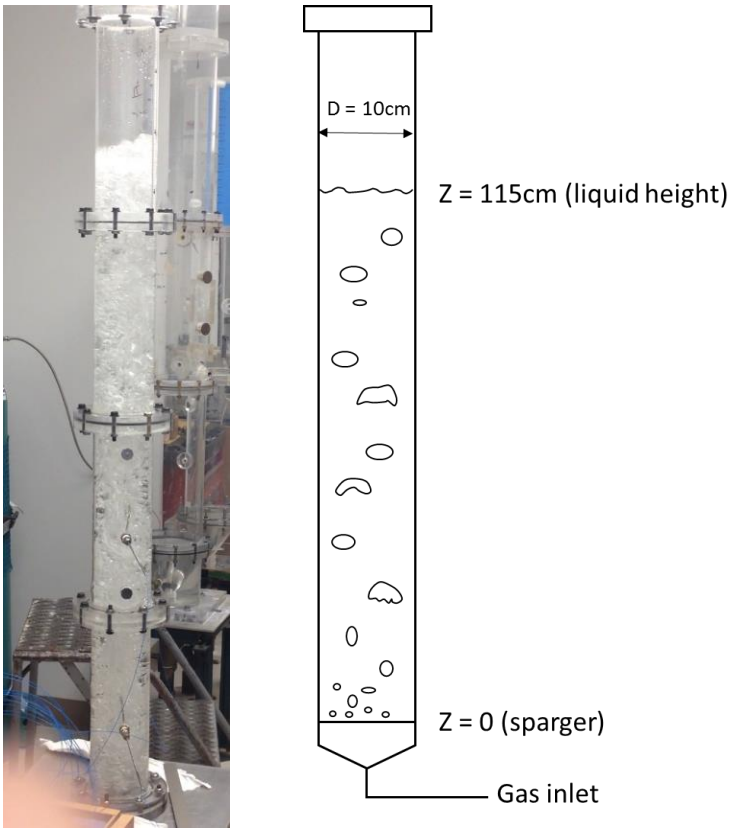

Figure 3.7: Photograph (left) and schematic (right)
of the 10-cm diameter bubble column reactor.

To make the optical probes, we used 200/225/500 µm core/cladding/coating diameter multimode optical fibers from Thorlabs. The fibers are of very similar dimensions compared to those developed by Xue (2004) and used by Wu (2007), Youssef (2010), and Hamed (2012) in bubble column reactors of different sizes and operating conditions. After the fibers were finished using the methods outlined in Mueller (2009), the fibers were sheathed in a U-shaped (Figure 3.8) stainless steel metal tubing of 1/8-inch diameter, and inserted into the reactor through the port installed on the reactor wall. The U-shape makes the change of the orientation in between runs much easier than for conventional L-shape probes. To change the probe orientation while keeping the measuring point the same, one simply needs to rotate the metal sheathing from the outside.

Figure 3.8: The U-shaped optical probe.

The probe was employed at six radial and four axial positions: at radial positions of $0.2R_{BC}$, $0.4R_{BC}$, $0.6R_{BC}$, $0.7R_{BC}$, $0.8R_{BC}$, and $0.9R_{BC}$ (R_{BC} = radius of the bubble column reactor) and at axial positions of $1.5D_{BC}$, $5D_{BC}$, $7.5D_{BC}$, and $9.5D_{BC}$ (D_{BC} = column diameter) measured from the sparger location. To quantify the recirculating loops near the reactor wall / annular region, optical probes were employed at narrower intervals near the reactor wall. Two optical probe measurements were made for each position, with the probe tips pointing down and up. The voltage signal from the photodiodes (Thorlabs PDA36A) were collected at a rate of 40kHz (PowerDAQ PD-BNC-16) for 1500 data acquisition frames, a total duration of 691.2 seconds.

The axial measurements made at the lowest and highest points represent the measurements made in the entrance and exit zones, because they are within $2D_{BC}$ of the sparger and free liquid surface. However, they are still within the mid-column zone in the CREL developed core-annulus models; the model originally developed by Degaleesan (1997) and later improved by Gupta (2002) for the heterogeneous flow regime defines the entrance and exit zones to be $1D_{BC}$ from the sparger and the free liquid surface.

3.3.2. Flow regime identification by the volume of expansion method

The volume of expansion method – how much the liquid level rises after the gas is introduced – was used to measure the overall gas phase holdup for the superficial gas phase velocity (U_{gas}) range of 1 cm/s to 25 cm/s. The results are shown in Figure 3.9.

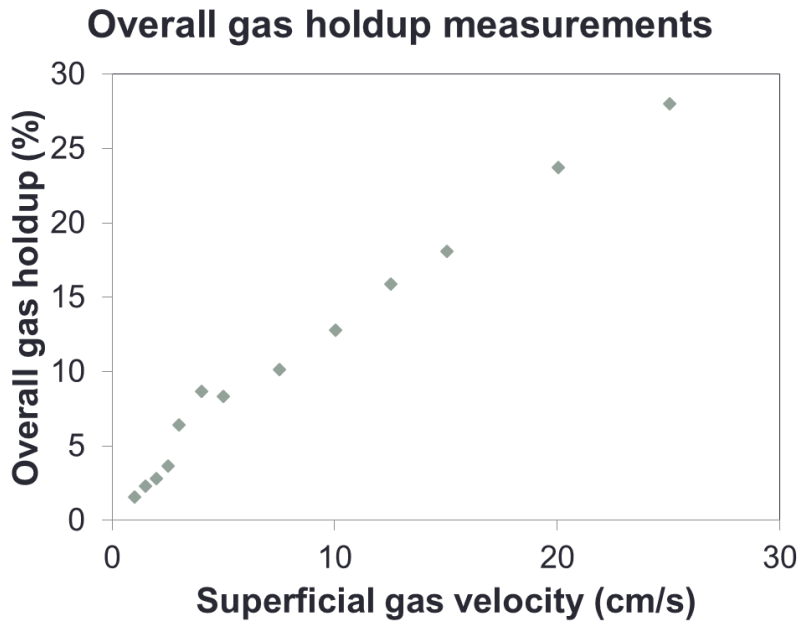

Figure 3.9: Overall gas holdup measurements.

The overall gas holdup profile looked very similar to that reported in the literature, i.e., Figure 3.3, with three distinct regions marked by different slopes / shapes at the ranges of 1 cm/s – 2.5 cm/s, 2.5 cm/s – 5 cm/s, and 5 cm/s – 25 cm/s (Figure 3.10). These results suggest that the transition points from the homogeneous to transition to heterogeneous flow regimes were at 2.5 cm/s and 5 cm/s, respectively. For the column size we investigated, Shah et al. (1982) suggested that the hydrodynamic flow regime directly transitioned into the slug flow regime (skipping the heterogeneous regime); however, visual observation of the column suggested the onset of the heterogeneous flow regime occurred with no slugs.

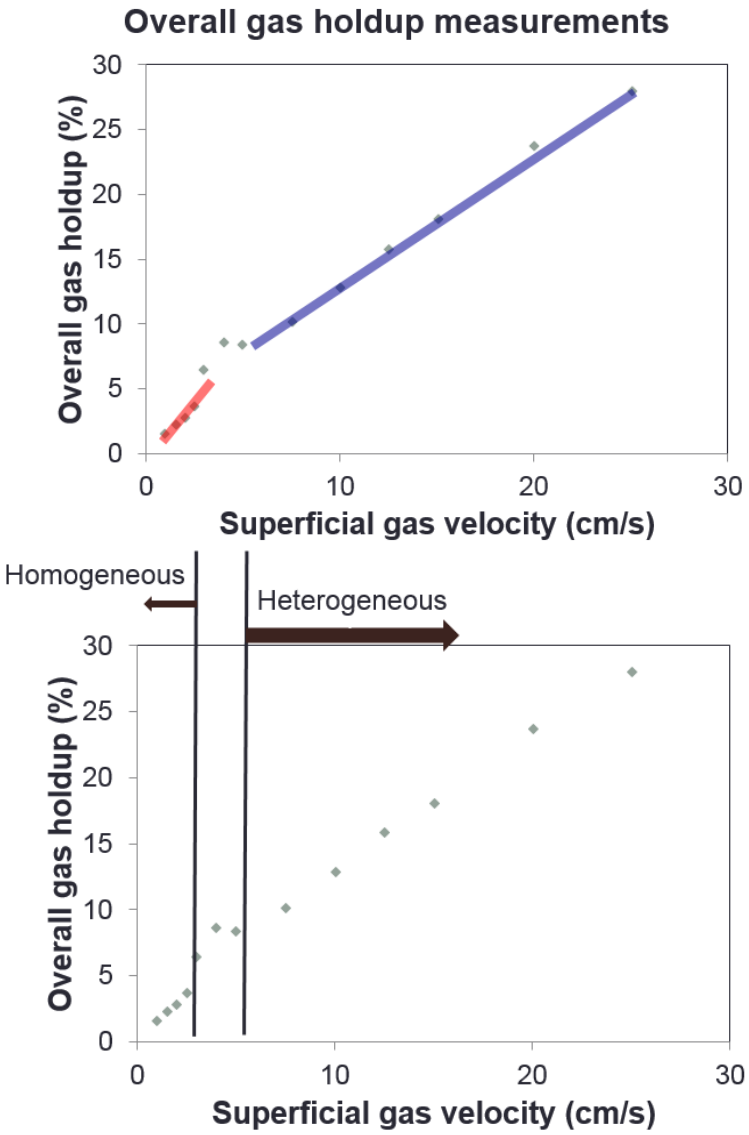

Figure 3.10: Identification of flow regime transitions.

Having verified the existence of the three flow regimes, we now discuss the results from the OPPM. All results shown here are reproducible, i.e., negligible standard deviation. Error bars are omitted as average gas holdups were used as inputs to the OPPM, because the longer the measurement time, the more representative our optical probe measurements. The results enable further fundamental understanding of how gas phase backmixing changes within each flow regime and with respect to other flow regimes.

3.3.3. Backmixing in homogeneous flow regime

Figure 3.11 shows the results from the OPPM in the entrance zone. Green circles represent the "unbiased" local gas phase holdup that takes into account bubbles that travel both upward and downward; blue circles represent the local gas phase holdup due to bubbles traveling upward; and red circles represent the local gas phase holdup due to bubbles traveling downward.

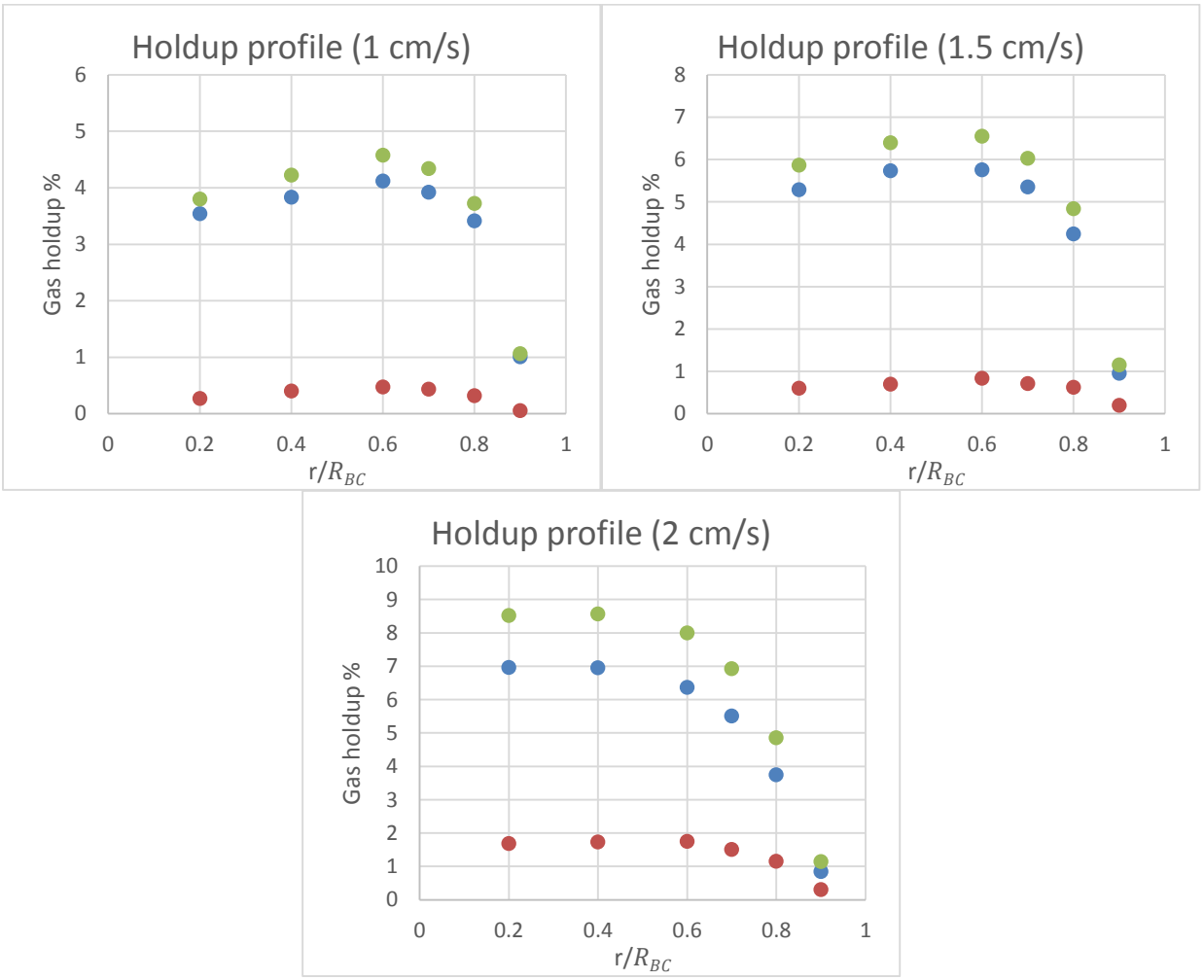

Figure 3.11: Measured gas phase holdup in entrance zone. X-axis, dimensionless radial position; y-axis, gas holdup. Green represents "unbiased" local gas phase holdup; blue represents gas holdup contributed by bubbles traveling upward; red represents gas holdup contributed by bubbles traveling downward.

Two features are notable in Figure 3.11:

1. When the superficial gas phase velocities are low, 1 cm/s and 1.5 cm/s, a parabolic gas holdup profile was not observed. Rather, the gas holdups were at their maximum at r ≈ $0.6R_{BC}$ with the concavity pointing downward. While further investigation may be necessary, visual observation revealed two causes for this phenomenon: insufficient distribution of air across the sparger and a lack of bubble-to-bubble interactions allowing the holdup profile to reach the hydrodynamic equilibrium. As U_{gas} increased to 2 cm/s, a parabolic holdup profile was established.

2. For all radial positions investigated, as U_{gas} increased, so did the fraction of the "unbiased" gas phase holdup contributed by bubbles traveling downward. This pattern can be seen in Figure 3.11 by locating how far the blue circles are from the green circles, or by locating how close the red circles are to the green circles. The observed trend is in line with a basic understanding of reactor hydrodynamic behavior: the higher the U_{gas}, the greater the gas phase backmixing. Great degree of bubble-bubble interactions, flow recirculation, and the turbulence are believed to be responsible for this behavior.

Very similar findings are observed when the same plots were made for the two mid-column and the exit zones. Figure 3.12 shows the two results from the mid-column zone; Figure 3.13 shows the result from the exit zone.

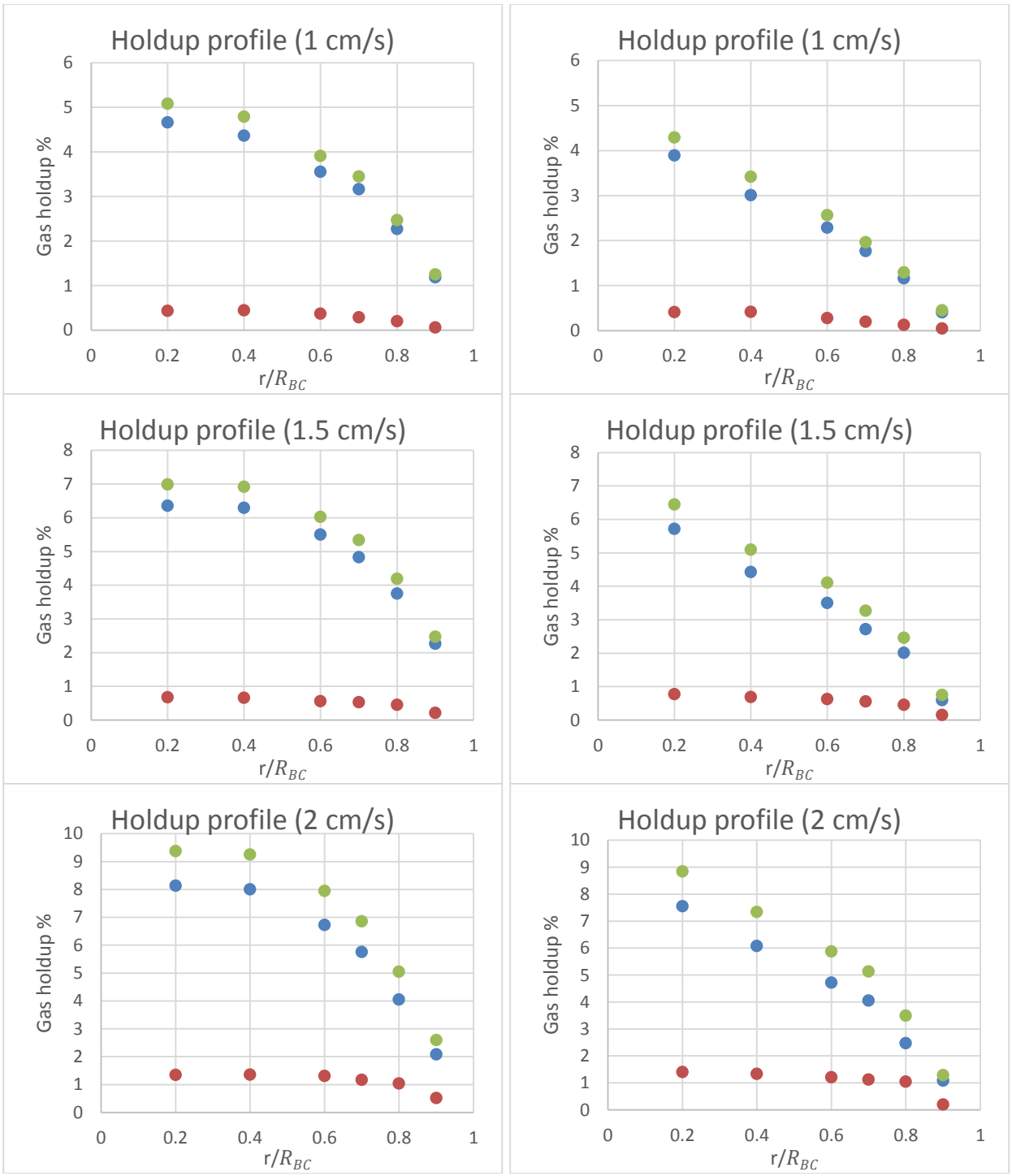

Figure 3.12: Measured gas phase holdup in the mid-column zone (left, lower mid-column zone; right, upper mid-column zone). X-axis, dimensionless radial position; y-axis, gas holdup. Green represents "unbiased" local gas phase holdup; blue represents gas holdup contributed by bubbles traveling upward; red represents gas holdup contributed by bubbles traveling downward.

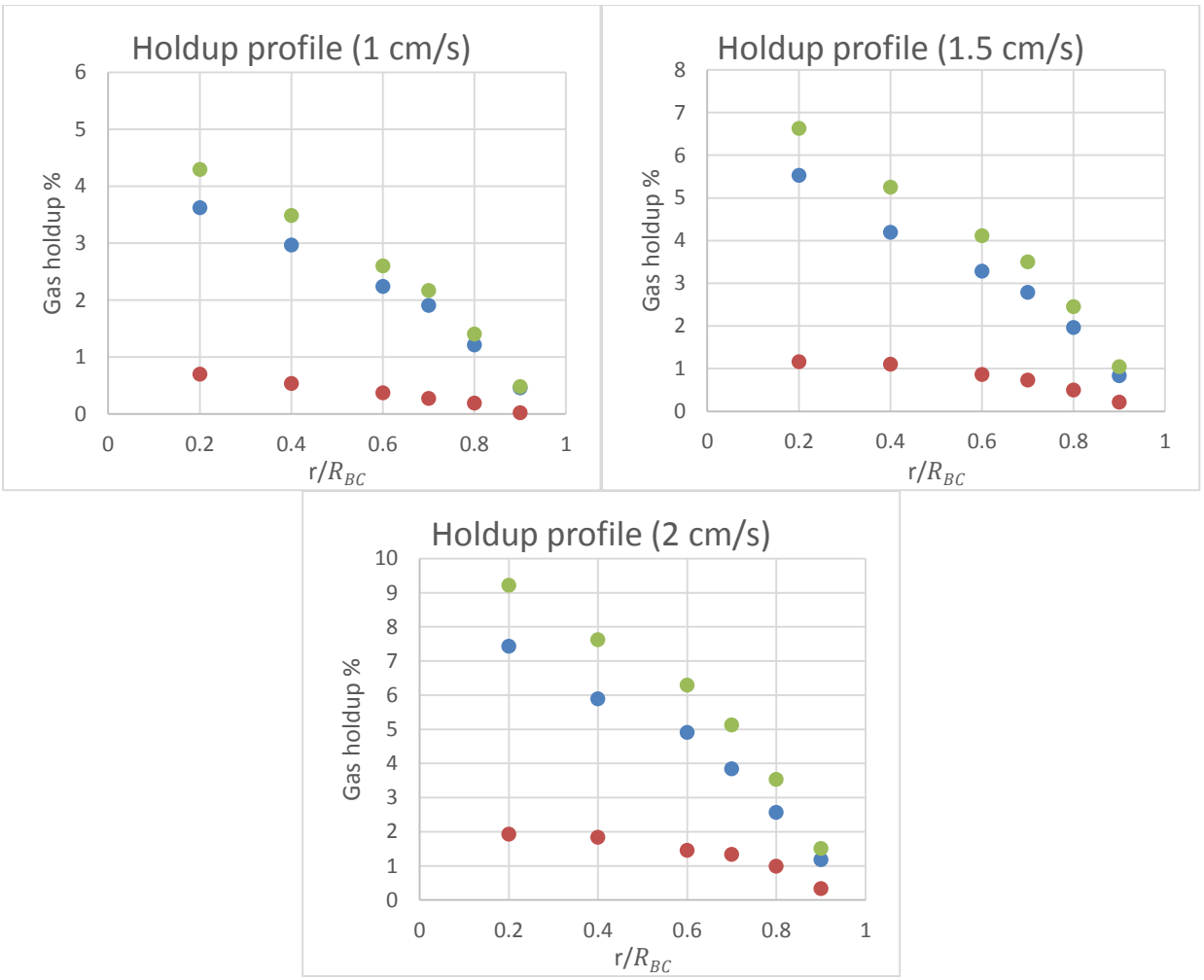

Figure 3.13: Measured gas phase holdup in exit zone. X-axis, dimensionless radial position; y-axis, gas holdup. Green represents "unbiased" local gas phase holdup; blue represents gas holdup contributed by bubbles traveling upward; red represents gas holdup contributed by bubbles traveling downward.

For all heights investigated, gas holdups due to bubbles traveling downward were found to be nearly identical for the regions where parabolic gas holdup profiles were observed. Within the two mid-column zone positions, however, one key difference was observed: the "unbiased" gas phase holdup values were higher in the lower position due to larger contribution from bubbles traveling upward.

Very similar hydrodynamic behavior was found in the two sets of measurements in the lower and upper parts of the reactor. The "unbiased" gas holdup profile for the lower mid-column zone was identical to that of the entrance zone when U_{gas} = 2 cm/s; the "unbiased" gas holdup profiles for the upper mid-column zone were identical to those of the exit zone for all operating conditions. These findings provide useful information on how to compartmentalize the reactor based on gas phase hydrodynamics in the homogeneous flow regime. As a first step, the column should be compartmentalized into lower and upper zones, with the boundary located in between heights of $5D_{BC}$ and $7.5D_{BC}$. Whether these compartments should be broken down into smaller compartments for reactor modeling depends on the existence of "true" entrance and exit zones, which can be obtained from additional analysis, similar to that described in this section.

3.3.4. Backmixing in transition flow regime

Figure 3.14 shows the results from the OPPM in the entrance zone in the transition flow regime; Figures 3.15 and 3.16 show the results in the mid-column and the exit zones. Contrary to the homogeneous flow regime, for all regions and operating conditions investigated, a parabolic gas holdup profile was observed.

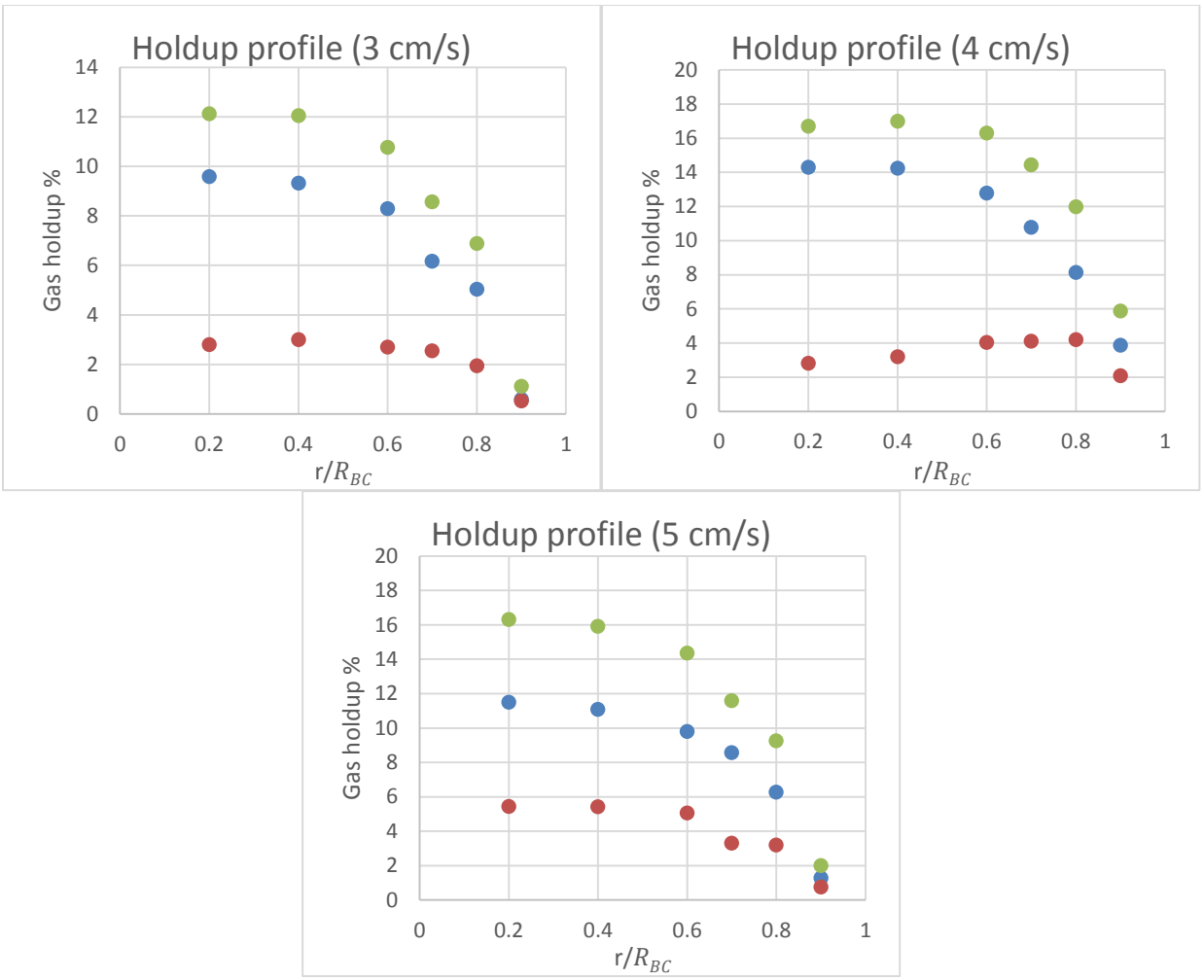

Figure 3.14: Measured gas phase holdup in entrance zone. X-axis, dimensionless radial position; y-axis, gas holdup. Green represents "unbiased" local gas phase holdup; blue represents gas holdup contributed by bubbles traveling upward; red represents gas holdup contributed by bubbles traveling downward.

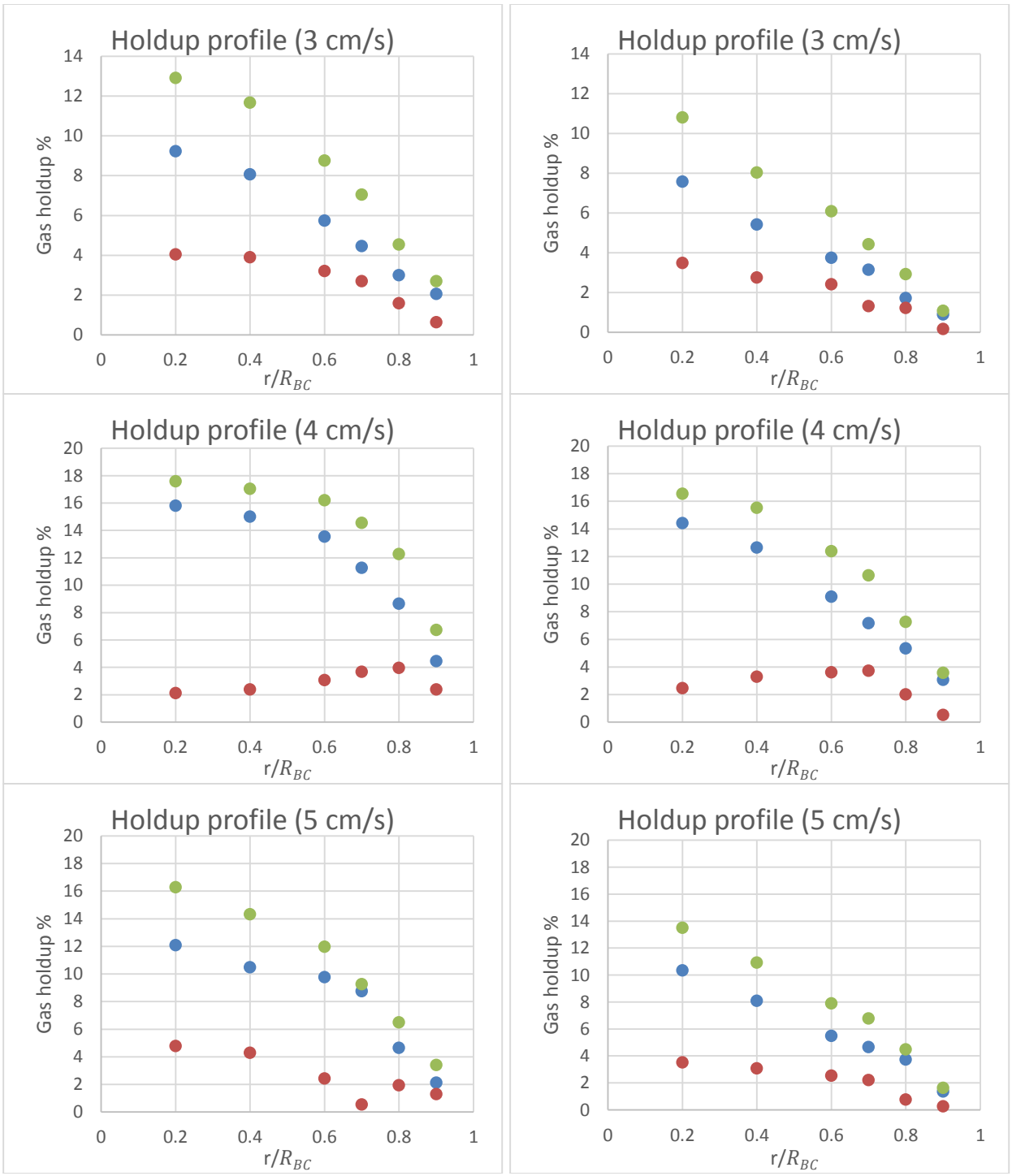

Figure 3.15: Measured gas phase holdup in the mid-column zone (left: lower mid-column zone, right: upper mid-column zone). X-axis, dimensionless radial position; y-axis, gas holdup. Green represents "unbiased" local gas phase holdup; blue represents gas holdup contributed by bubbles traveling upward; red represents gas holdup contributed by bubbles traveling downward.

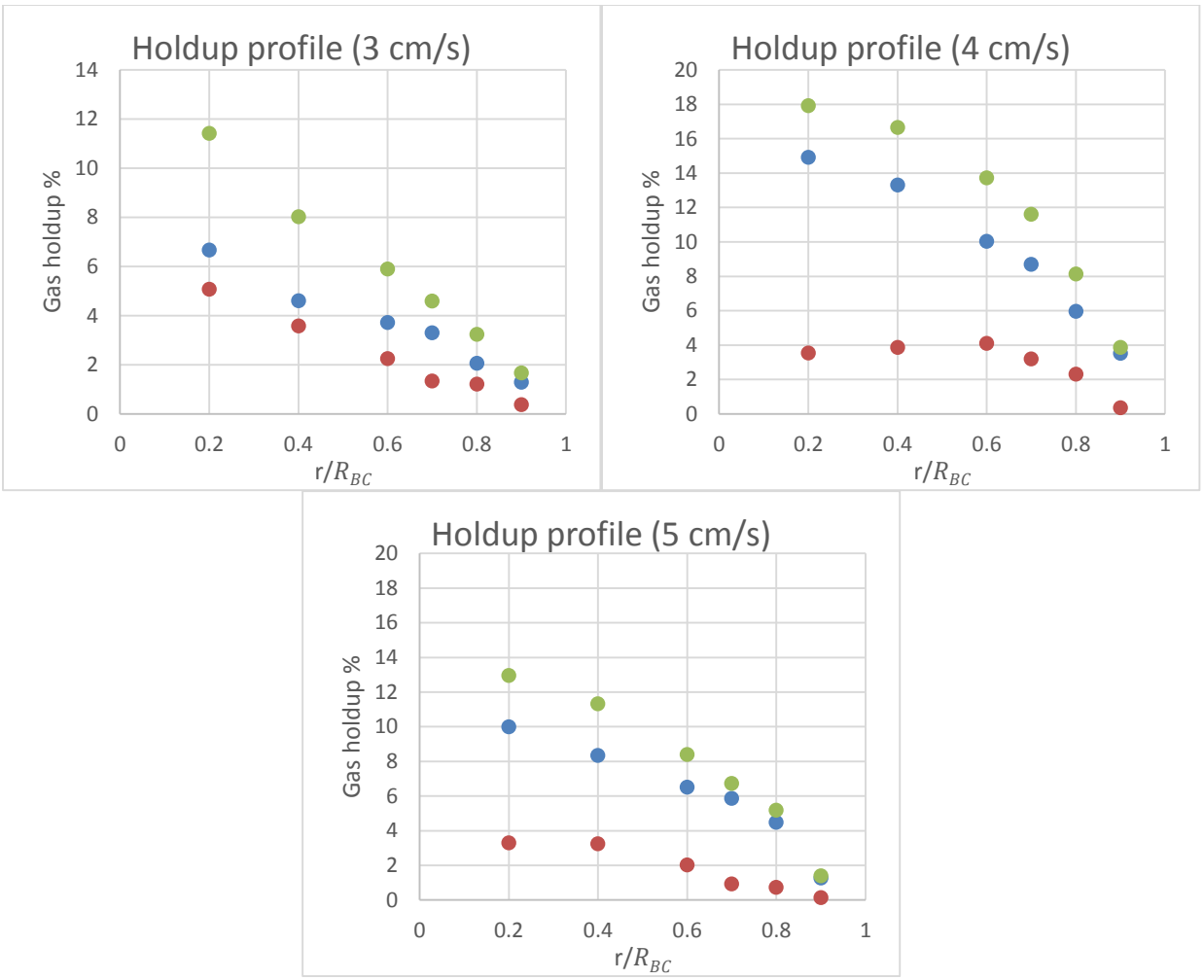

Figure 3.16: Measured gas phase holdup in exit zone. X-axis, dimensionless radial position; y-axis, gas holdup. Green represents "unbiased" local gas phase holdup; blue represents gas holdup contributed by bubbles traveling upward; red represents gas holdup contributed by bubbles traveling downward.

The rather unusual and unexpected non-monotonic overall gas holdup profile observed in the transition flow regime (Figures 3.9 and 3.10) was effectively captured by the local gas holdup and local backmixing profiles. As U_{gas} increased from 3 cm/s to 5 cm/s and the overall holdup showed a rise-and-fall pattern, so did the "unbiased" local gas holdup for all heights and radial positions investigated, revealing this pattern to be a global reactor characteristic not confined to entrance, mid-column, and/or exit zones.

At U_{gas} = 4 cm/s, where the overall gas holdup was found to at its largest, the contribution by bubbles traveling downward was found to be at its maximum at radial positions of r ≈ $0.8R_{BC}$, r ≈ $0.75R_{BC}$, and r ≈ $0.6R_{BC}$ for the entrance, mid-column, and the exit zones. This pattern is most likely due to the varying degrees of recirculation and the different paths these eddy-like structures take. The presence of buoyancy- and gravitational force-driven recirculation has been reported for both the continuous phase (liquid or liquid-solid) (e.g., Degaleeesan, 1997; Han, 2007) and dispersed (gas) phase (e,g, Xue, 2004; Wu, 2007), using proven experimental techniques.

In the transition flow regime, the distinctions and/or similarities between different reactor zones were less distinct. For example, in the mid-column zone, the measurements from the lower zone showed slightly higher "unbiased" local gas phase holdups than the upper mid-column section at all radial positions, yet the fractions of bubbles going down were observed to be nearly equal. Additionally, the overall gas holdup profiles were nearly equal in the upper mid-column and the exit zones, but the contribution from bubbles moving downward was found to be larger in the entrance zone. These results suggest that gas phase dynamics in the transition flow regime are more complex and irregular than in the homogeneous flow regime; further investigation is required in the transition flow regime for better gas phase reactor modeling.

3.3.5. Backmixing in heterogeneous flow regime

Figures 3.17 through 3.19 show the results obtained in the heterogeneous flow regimes for the three zones investigated. Once again, a parabolic gas holdup profile was found for all operating conditions and zones investigated.

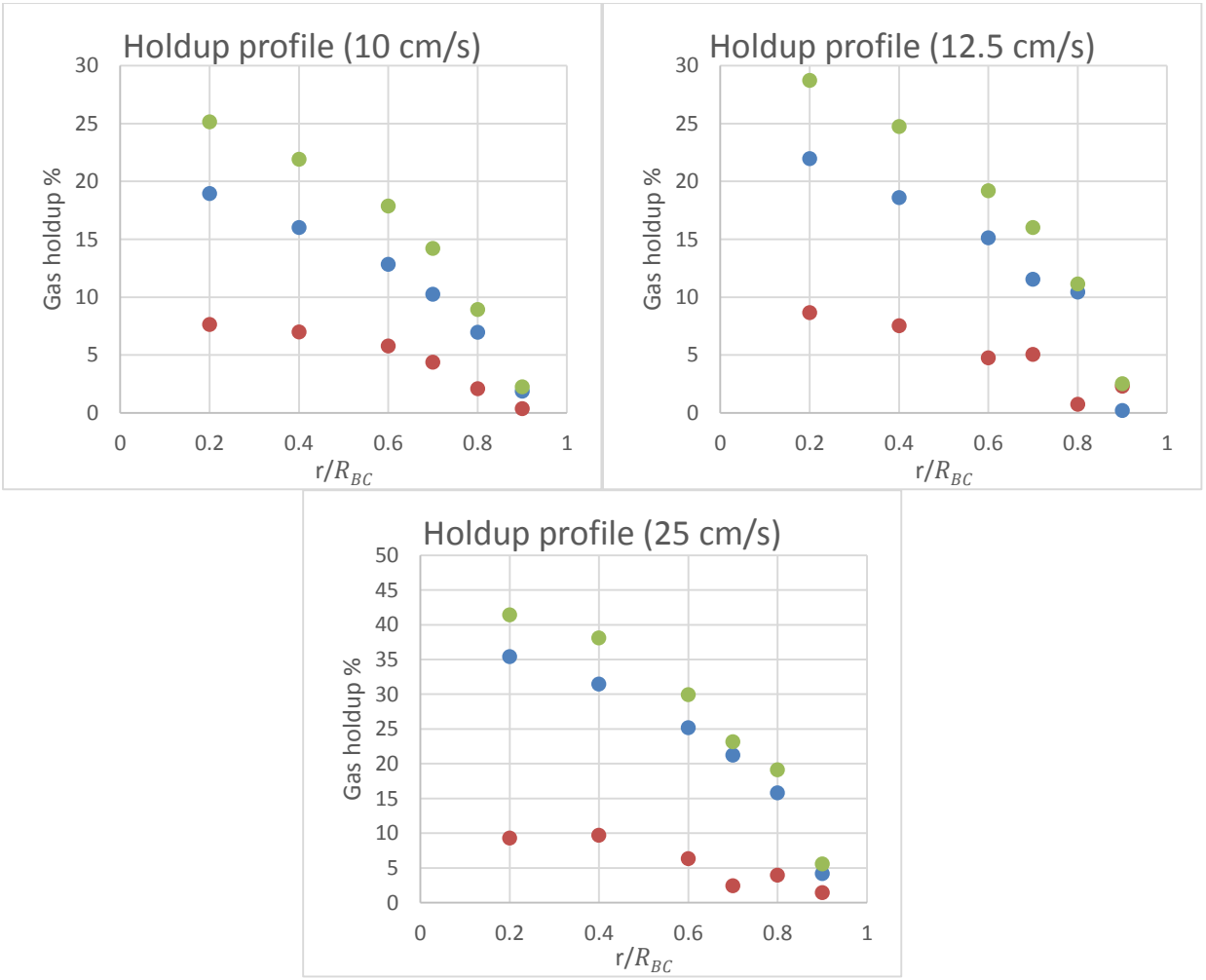

Figure 3.17: Measured gas phase holdup in entrance zone. X-axis, dimensionless radial position; y-axis, gas holdup. Green represents "unbiased" local gas phase holdup; blue represents gas holdup contributed by bubbles traveling upward; red represents gas holdup contributed by bubbles traveling downward.

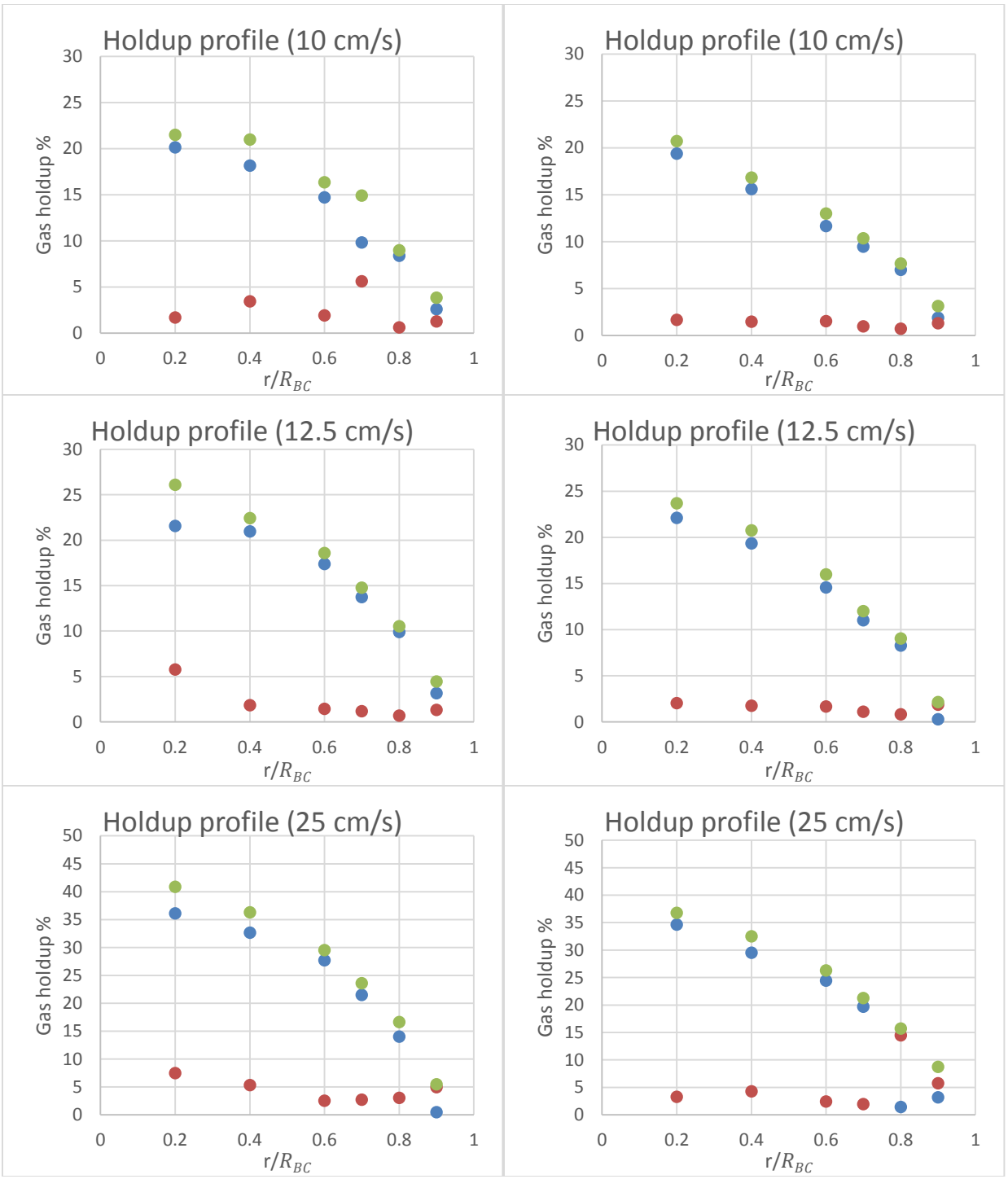

Figure 3.18: Measured gas phase holdup in the mid-column zone (left: lower mid-column zone, right: upper mid-column zone). X-axis, dimensionless radial position; y-axis, gas holdup. Green represents "unbiased" local gas phase holdup; blue represents gas holdup contributed by bubbles traveling upward; red represents gas holdup contributed by bubbles traveling downward.

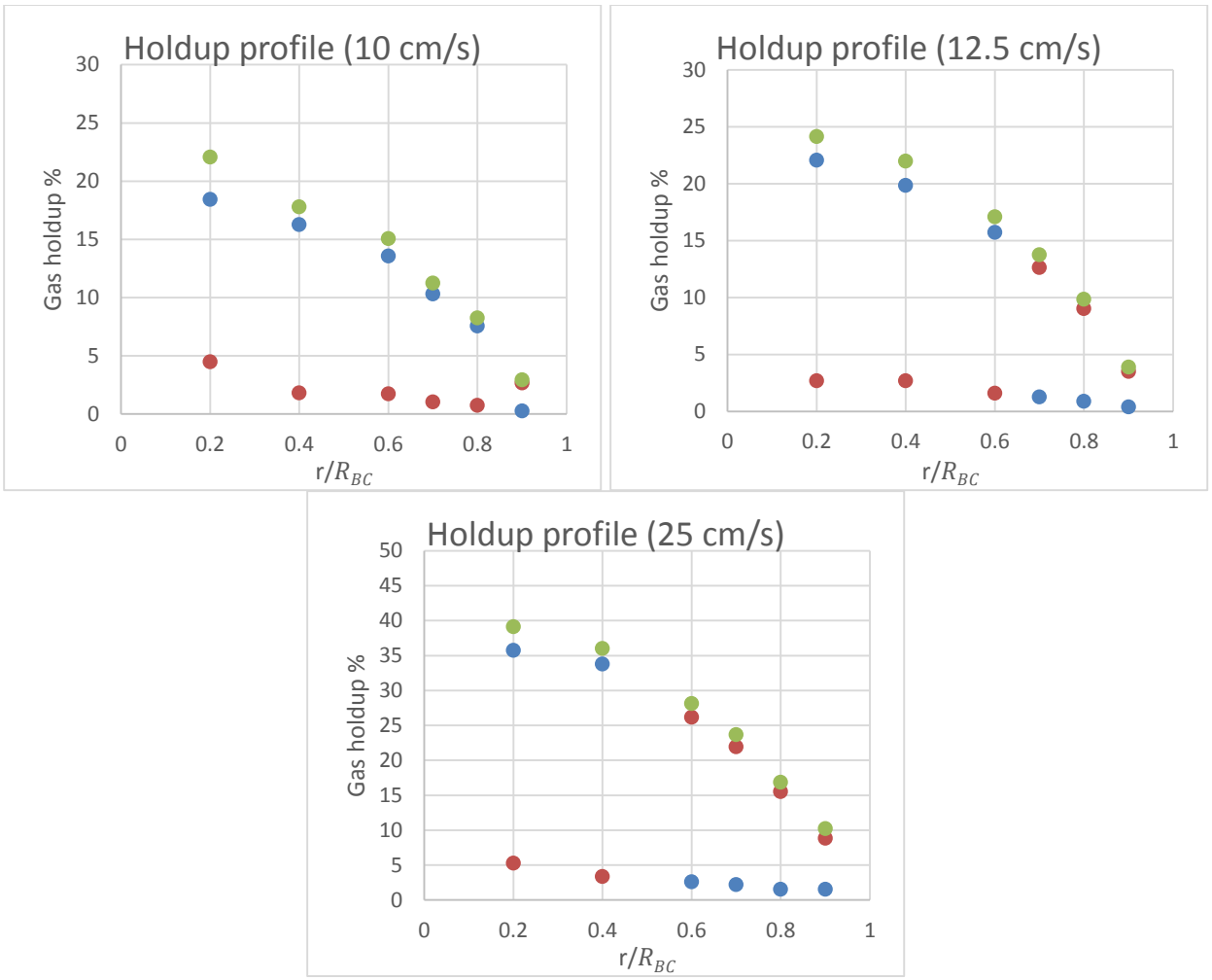

Figure 3.19: Measured gas phase holdup in exit zone. X-axis, dimensionless radial position; y-axis, gas holdup. Green represents "unbiased" local gas phase holdup; blue represents gas holdup contributed by bubbles traveling upward; red represents gas holdup contributed by bubbles traveling downward.

Several findings are apparent:

1. Both the "unbiased" local gas holdups and the degree of backmixing were the largest in the entrance zone. These results suggest the highest degree of CSTR-like behavior in the entrance zone for the gas phase, and they support the 1-D core-annulus model developed by Degaleesan (1997) and later extended by Gupta (2002). The boundary between the entrance and mid-column zone for the gas phase, however, needs to be adjusted, since the

boundary was set at $1D_{BC}$ for the core-annulus model, and the probe for this investigation was located at $1.5D_{BC}$.

2. In the exit zone: a) both the degree of recirculation near the wall and the local gas phase backmixing increased significantly as U_{gas} increased, b) a core-annulus-like flow structure with the greatest amount of gas phase backmixing was observed, and c) as U_{gas} increased, the radial position where the major bubble movement changes its direction from going up to going down shifted towards smaller R_{BC}.

3. The "unbiased" local gas phase holdup and backmixing profiles for the measurements made in the mid-column zone were nearly identical, supporting the idea of one mid-column zone with uniform hydrodynamic behavior. At very high U_{gas}, however, the radial position where major bubble movement changes its direction shifted toward the central part of the reactor, as captured in the upper mid-zone by the optical probe.

4. The degree of backmixing in the mid-column zone was very small for most operating conditions, suggesting a PFR-like behavior in this zone. This result is contrary to what was suggested when global experimental techniques, e.g., RTD, were used to fit the axial dispersion reactor model, e.g., Han (2007) and Hamed (2012). Having a larger fitted axial dispersion coefficient does not necessarily mean higher degree of backmixing; however, people often correlate the two things. These results suggest that in the heterogeneous flow regime, a model that compartmentalizes the reactor into entrance, mid-column, and exit zones should be utilized. In the entrance and mid-column zones, CSTR-like and PFR-like equations should be applied. For the exit zone, using a CSTR-like equation is

recommended, because largest gas phase backmixing was observed; however, further investigation is necessary due to the observed core-annulus-like flow pattern.

3.4. Conclusions

This chapter detailed the application of the OPPM to bubble column reactors. The results provided detailed gas phase dynamics and backmixing information that had not been available before, mainly due to the lack of experimental techniques. The optical probe and the OPPM were employed in six radial and four axial positions to elucidate the radial and axial dependency of the measured parameters.

To bridge the knowledge gap between the local and the global reactor hydrodynamics, the volume of expansion method was first employed to find the transition points for the different hydrodynamic flow regimes. For the small 10-cm diameter bubble column investigated, the overall gas holdup profile and visual investigation revealed homogeneous, transition, and heterogeneous flow regimes. Slug and annular flow regimes were not observed within the operating conditions investigated.

Within the homogeneous flow regime, the two quantities investigated – the "unbiased" gas phase holdup and degree of backmixing – showed positional and operating condition dependencies. Parabolic gas holdup profiles were not observed in the lowest part of the reactor when U_{gas} was very low. Detailed analysis of the two measured quantities suggested compartmentalization of the reactor into two regions for gas phase modeling, the lower and the upper zones. As the U_{gas} increased, so did the degree of backmixing for both regions; however, all regions investigated still behaved more like PFR.

For the transition flow regime, the rise-and-fall pattern of the overall gas phase holdup profile was effectively captured by the OPPM at all heights investigated. The hydrodynamic distinction between different heights was very difficult when the reactor was viewed as having distinct three zones (entrance, mid-column, and exit zones), because either the "unbiased" local gas phase holdups or the degree of backmixing did not match within the heights where our probes were employed. In general, the degree of backmixing was found to be greater than what was observed in the homogeneous and heterogeneous flow regimes.

As the flow regime transitioned into the heterogeneous flow regime, very distinct features were observed for the entrance, the mid-column, and the exit zones. In the entrance zone, the highest local gas holdups and degree of backmixing were observed, suggesting CSTR-like behavior. In the mid-column zone, the degree of backmixing was lower than observed backmixing in the heterogeneous flow regime, and similar to what was observed in the homogeneous flow regime, a PFR-like behavior. In the exit zone, the degree of recirculation near the wall increased significantly as U_{gas} increased. The radial position where the major bubble movement change its direction from going up to going down shifted towards smaller R_{BC}, suggesting a core-annulus type of flow.

For the first time, these results provide a physical description of gas phase backmixing in a bubble column reactor. The introduced methodology can be extended to any industrial bubble column reactors of different sizes for better gas phase modeling. For the reactor we investigated, the mid-column zone should be modeled using PFR-like equations in the homogeneous and heterogeneous flow regimes, whereas the entrance and exit zones can be modeled using a CSTR-like equation only in the heterogeneous regime.

Chapter 4. Gas phase dynamics in gas-liquid stirred tank reactors (STRs)[6]

STRs are one of the most effective gas-liquid contactors, capable of handling numerous duties (Harnby et al., 1985), from very basic chemical and petrochemical processes to newly developed biochemical and biological ones. Both the continuous phase (liquid or liquid-solid) and dispersed phase (gas) can be operated under either continuous or batch mode (Figure 4.1). STRs have been so popular among industry that, in 1991, it was estimated that nearly half of the chemical industry's output had passed through a STR at one point (Tatterson, 1991). This number probably has not changed by much: Stitt (2002) noted that any other types of liquid reactors are rarely used, because "stirred tank is convenient."

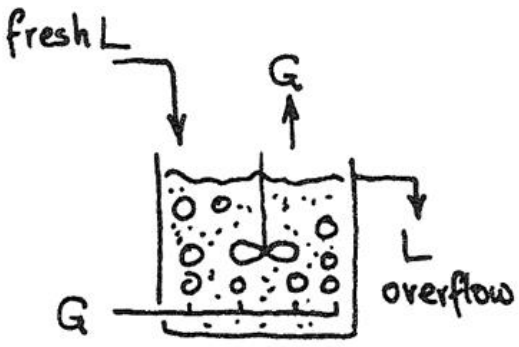

Figure 4.1: Stirred tank reactor (source: Levenspiel, 2002).

In general, the process efficiency of a gas-liquid STR highly depends on the degree of interfacial contact. As the gas-liquid interfacial area per unit volume (a) changes, so do other important operating parameters, such as the volumetric heat and mass transfer coefficients. Naturally, much

[6] Some material in this chapter was previously published in Lee and Dudukovic (2014a, 2014b).

effort has been invested in developing useful correlations for these parameters via proven experimental techniques and computational simulations (Wang et al., 2000; Lane et al., 2002, 2005; Cents et al., 2005; Khopkar and Ranade, 2006; Wang et al., 2006; Ford et al., 2008; Mueller, 2009; Mueller and Dudukovic, 2010). As with bubble column reactors, measuring all the needed parameters at the needed time and length scales is not possible from first-principle based reactor models, so simplifying assumptions and correlations have been developed and are widely utilized.

4.1. Hydrodynamic flow regimes and challenges in gas-liquid STRs

For a standard fully baffled gas-liquid STR equipped with central Rushton turbine (RT), several flow regimes have been identified, based on major bubble trajectories and flow patterns as shown in Figure 4.2.

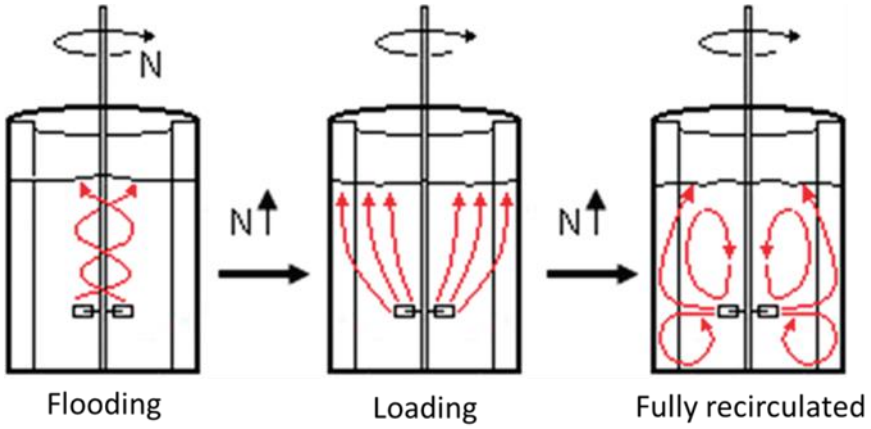

Figure 4.2: Flow regime transition from flooding to loading to the fully recirculated regime. As N (impeller rotational speed) increases, gas bubbles occupy more regions within the tank. Adapted from Mueller and Dudukovic (2010).

In the literature, three regimes have been described using two dimensionless numbers. These three regimes are called the flooding, loading, and fully recirculated regimes (Harnby et al., 1985; Tatterson, 1991; Bombac et al., 1997), and the two dimensionless numbers are the Flow number (*Fl*) and the Froude number (*Fr*). The *Fl* number is the ratio between the gas flow rate and the impeller driven flow rate; the *Fr* number is the ratio between the impeller driven acceleration and gravity. In equation form,

$$Fl = \frac{Q_g}{N \cdot D_T^3} \tag{4.1}$$

$$Fr = \frac{N^2 \cdot D_T}{g}, \tag{4.2}$$

where Q_g is the gas flow rate from the sparger, *N* is the impeller rotational rate, D_T is the turbine diameter, and g is the gravitational constant. As the *Fr* number increases, i.e., more acceleration is provided by an increased impeller rotational rate, the flow regime transitions from a less to a more dispersed state. Likewise, as *Fl* decreases, i.e., by introducing less gas to be dispersed or by providing more acceleration by means of an increased impeller rotational rate, the flow regime transitions from a less to a more dispersed state. A complete flow regime map for an air-water system has been provided by several researchers (Warmoeskerken and Smith, 1985; Bombac et al., 1997; Jade et al., 2006; Khopkar and Ranade, 2006; Mueller, 2009) and is shown in Figure 4.3.

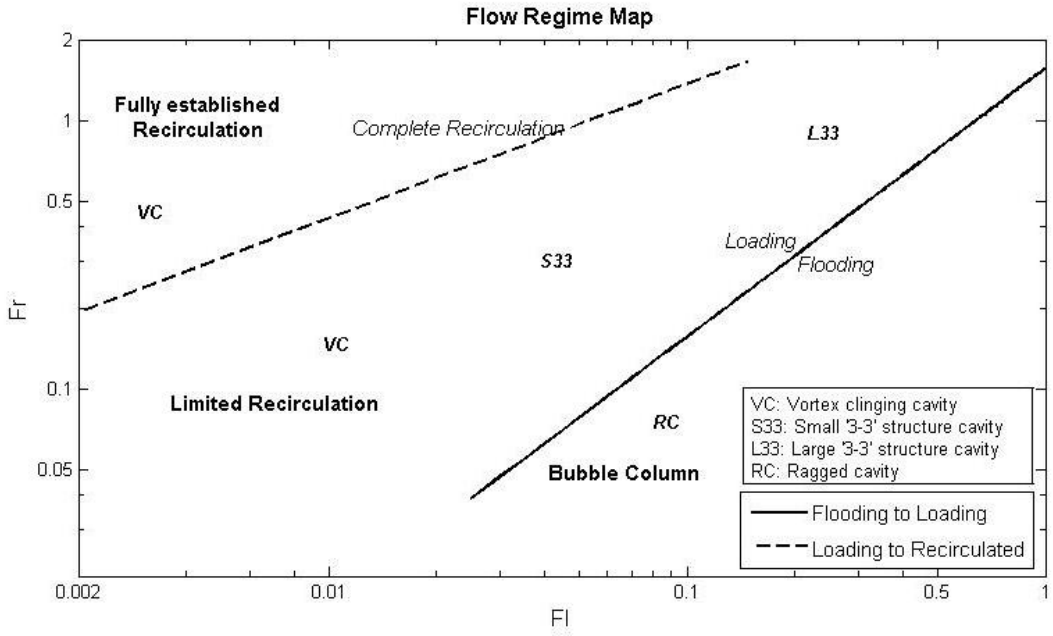

Figure 4.3: Complete flow regime map for a standard fully baffled air-water STR.

In the flow regime map, cavity structures observed behind the impeller blades are also indicated, because different cavity structures are well known to be associated with each flow regime (Bombac et al., 1997; Tatterson, 1991). VC represents the vortex clinging structure, S33 represents the small '3-3' structure, L33 represents the large '3-3'structure, and RC represents ragged cavities (Figure 4.4). The two transition lines, from the flooding to the loading and the loading to the fully recirculated regime, were first determined by observing at which operating conditions the dominant bubble trajectories had changed, and later confirmed by determining the cavity structures. In dimensionless form, the two transition lines are

$$\text{Transition from flooding to loading regime} = Fl_F = 30Fr\left(\frac{T}{D}\right)^{-3.5} \qquad (4.3)$$

$$\text{Transition from loading to recirculated regime} = Fl_{CD} = 13Fr^2\left(\frac{T}{D}\right)^{-5}. \qquad (4.4)$$

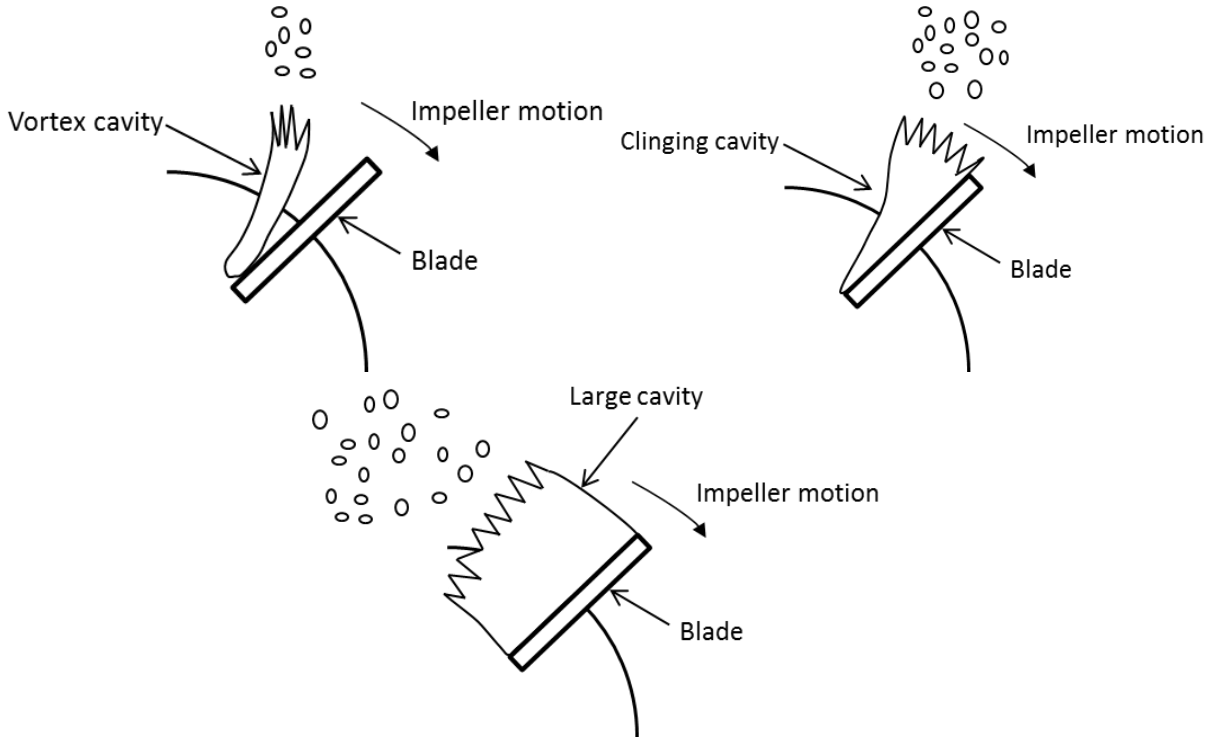

Figure 4.4: Cavities formed behind blades.
Refer to Rammohan (2002) for ragged cavity structure description.

In recent years, the demand for more reliable experimental techniques for identification of the flow regimes has risen considerably, partly due to ever increasing computational power and many computational fluid dynamic (CFD) models being readily available. As concluded by Rammohan (2002), Guha (2007), and Mueller (2009), even the most detailed results obtained by the CFD models in STRs are subject to validation via proven experimental techniques, due to the numerous assumptions and closure models associated with them. While much success in modeling gas-liquid STRs had been reported, e.g., Bakker and Van den Akker (1994) and Zhang et al. (2008), the results are almost always verified at only very few operating conditions. Whether the reported models can be used over the whole range of operating conditions remains to be verified, especially in the loading and fully recirculated regimes, where most processes are operated, and near the transition lines, where the local flow properties are difficult to describe.

Moreover, a robust methodology is needed for accurate in-situ characterization/determination of the flow regime, because each flow regime possesses different flow characteristics, e.g., the degree of local stress and the presence of recirculating loops, which play a critical role in different processes. For example, Shamlou et al. (1994) identified tensile stress, which originates from dynamic pressure fluctuations, as one of the leading causes for the breakage of filamentous micro-organisms in stirred tank bioreactors, and Ghadge et al. (2005) noted that the average shear rate is strongly correlated to the extent of enzyme deactivation. Breakup mechanisms for fluid particles, e.g., gas phase bubbles, are known to be determined by the hydrodynamic conditions, which include turbulent fluctuation, collision, and viscous shear stress, among others, as reviewed by Liao and Lucas (2009).

4.2. Time-series analysis of optical probe measurements for detection of flow regime transitions in STRs

Time-series analysis describes systems of dynamic and chaotic behavior in three domains: time, frequency, and state space. By applying the developed methodologies, the analysis breaks the time series data into the three domains, and the results are used to extract both meaningful and hidden statistics and characteristics. Noting the capability of time-series analysis, researchers developed numerous approaches for its use in bubble column reactors, fluidized bed reactors, and gas-liquid stirred tanks. Some of the notable works include analyses of global pressure fluctuation measurements in fluidized beds and bubble columns (Drahos et al., 1992; Johnsson et al., 2000; Fraguio et al., 2008; van Ommen et al., 2011); global pressure, impeller torque, and global conductance fluctuation measurements in gas-liquid stirred tanks (Paglianti et al., 2000; Khopkar et al., 2005); local flat-end optical probe measurements in fluidized beds (Werther et

al., 1996); and global CARPT measurements in bubble columns (Fraguío et al., 2007; Fraguio et al., 2008). In all these studies, the major objectives were to relate the degree of signal fluctuations to the unique underlying fluid dynamics of the observed global reactor flow regime.

This section describes the usefulness of the time-series analysis approach for measurements from tapered end optical probes. Specifically, it presents results based on time and frequency domain analyses for gas-liquid stirred tank reactors (STR). The region of interest is the impeller discharge plane, since in this region bubbles change their behavior from deterministic (with respect to the impeller motion) to chaotic as they move further away from the impeller. Although several studies (Kerdouss et al., 2006; Khopkar and Ranade, 2006; Zhang et al., 2008; Zhang et al., 2009; Petitti et al., 2010; Buffo et al., 2012) revealed where these transitions might take place, the main focus of those works was to validate the computational fluid dynamics (CFD) models, and therefore the results were presented at only several operating conditions. While the experiments and analysis methods presented here were carried out in a lab scale reactor using filtered air and tap water at standard temperature and pressure, the same technique and methodologies can be extended to other gas-liquid systems at harsh conditions, such as high temperatures and pressures, since the optical probe can operate under these conditions (Mueller et al., 2007; Sun et al., 2013).

4.2.1. Experimental setup and the optical probe

Gas-liquid stirred tank reactor (STR)

The gas-liquid STR used here is equivalent to the one used by Rammohan (2002), Khopkar et al. (2005), Guha (2007), and Mueller (2009). Figures 4.5 and 4.6 show the reactor and the gas sparger.

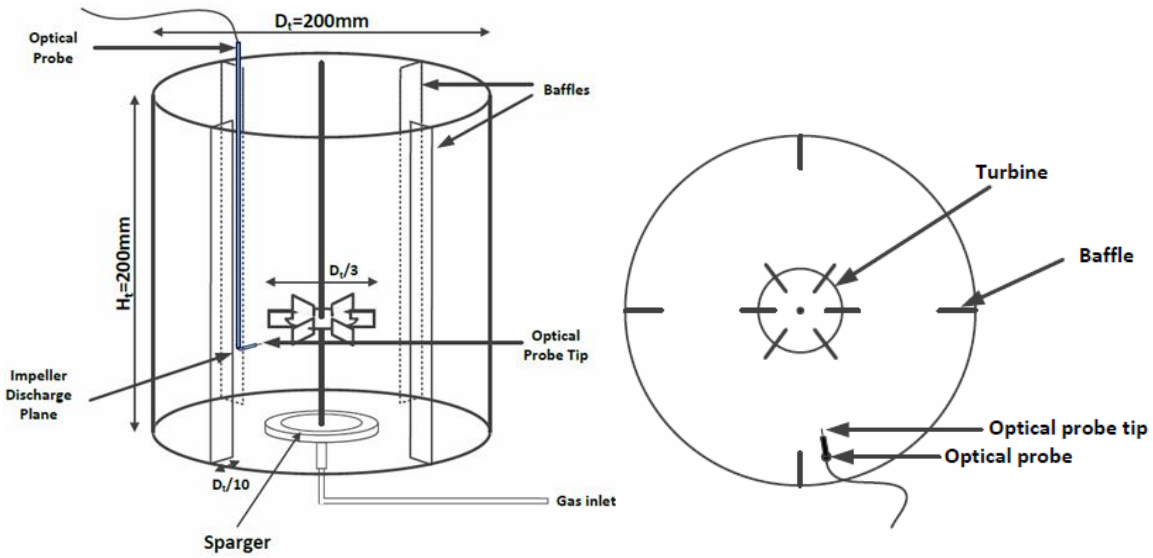

Figure 4.5: Gas-liquid STR setup equipped with a Rushton turbine and the optical probe positioned on the impeller discharge plane. Left: isometric view. Right: Horizontal cross-sectional plane.

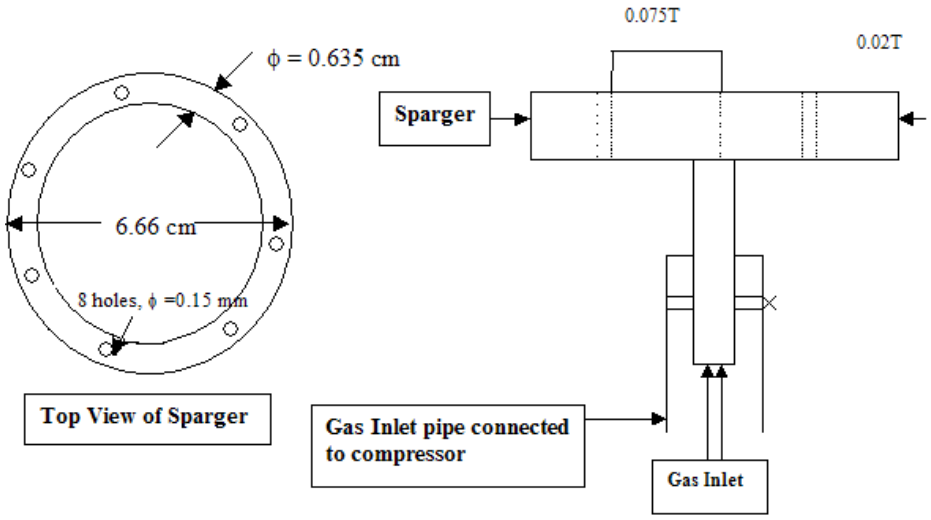

Figure 4.6: Ring gas sparger (source: Rammohan, 2002).

The setup consists of a central turbine positioned at 1/3 of liquid height, a ring gas sparger at the bottom of the tank, and four baffles of width $0.1D_{STR}$ (where D_{STR} = diameter of the tank) on the reactor wall to prevent vortexing at higher impeller speeds. Two impeller types with equivalent

dimensions were used: a Rushton turbine (RT) and a half circular blade disk turbine (CDT). Figure 4.7 shows the two impellers.

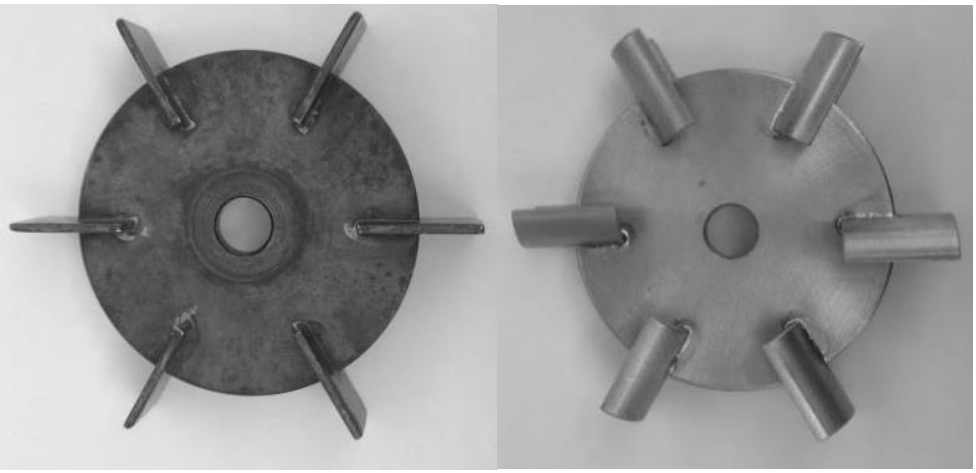

Figure 4.7: Rushton turbine (left) and half circular blades disk impeller (right).

For all runs, the reactor was filled with tap water up to H_t = 20 cm, and filtered air was used. Data were taken over the whole range of the *Fr* achievable in the CREL at a fixed *Fl* of 0.045. For the STR equipped with a RT, the flow regime transitions from flooding to loading to the fully recirculated regime at $Fr_{Flooding}$= 0.07 and the $Fr_{Loading}$ = 0.91 under the operating condition of *Fl* = 0.045. For the STR equipped with a CDT, the transition onsets were observed at lower Fr numbers (Vasconcelos et al., 1999).

Optical probe and data acquisition

For our probes, 105/125/250 μm core/cladding/coating diameter multimode optical fibers from Thorlabs were tapered and polished via methods outlined by Mueller (2009). The finished fibers were then epoxied into 1/8 inch-diameter stainless steel tubes. The probes were inserted into the reactor from the upper, free surface, with their tips bent at right angles to face the main flow direction at the impeller discharge plane, as shown in Figure 4.5.

For the gas-liquid STR equipped with a RT, measurements were taken at five radial positions, r = $0.4R_{STR}$, $0.5R_{STR}$, $0.6R_{STR}$, $0.7R_{STR}$, and $0.8R_{STR}$ (where R_{STR} = radius of the tank), whereas for the gas-liquid STR equipped with a CDT, measurements were taken at four radial positions r = $0.4R_{STR}$, $0.5R_{STR}$, $0.6R_{STR}$, and $0.7R_{STR}$. The probes were positioned at the windward side of the baffle to capture as few baffle effects as possible. For each run, voltage signals from the photodiode (Thorlabs PDA36A) were recorded at 40 kHz (PowerDAQ PD-BNC-16) for 138.24 seconds.

4.2.2. Data analysis

Three parameters typically obtained through a tapered optical probe, i.e., the local gas phase holdup, bubble count, and bubble residence time distributions, were obtained. In addition, autocorrelation sequences, R_{xx}, and power spectral density (PSD) estimates were obtained for determination of signal self-resemblance, *i.e.*, the likelihood of bubble occurrences at future times, and the chaotic nature of bubble occupancy. For these purposes, $V_{normalized}$ was further processed to consist of only two values, 1 for gas and 0 for liquid. The differences between the obtained R_{xx} and PSD estimates before and after the transformations were found to be insignificant.

The autocorrelation sequence represents the persistency of the data as a function of time lag, *m* times Δ*t*, and can be obtained via Equations 4.5 and 4.6,

$$r_{xx}(m) = \sum_{n=0}^{N-m-1} x(n) \cdot x(n+m) \tag{4.5}$$

$$R_{xx}(m) = \frac{r_{xx}(m)}{r_{xx}(0)}. \tag{4.6}$$

In these equations, *N* represents the total number of measurements, $x(n)$ the n-th data point, $r_{xx}(m)$ the non-normalized autocorrelation sequence, and $R_{xx}(m)$ the normalized autocorrelation sequence with respect to zero lag.

Rather than applying the discrete fourier transform (DFT) directly to the autocorrelation sequence, Welch's method (Welch, 1967) was used for the PSD estimations. This method applies a specified window function to the i-th segment of the original data before transforming it to the frequency domain. In equation form,

$$P_{xx}^{i}(f) = \frac{1}{N_s U}\left|\sum_{n=1}^{N_s} x_i(n)w(n)\exp(-j2\pi fn)\right|^2, \quad (4.7)$$

where P_{xx}^{i} is the PSD estimate of the i-th segment, $x_i(n)$ is the i-th segment of the original time series data, $w(n)$ is the specified window function, N_s is the segment length, and $U = \frac{1}{N_s}\sum_{n=1}^{N_s} w^2(n)$ is the window normalization constant. The averaged power spectrum is then obtained by averaging *i* PSD estimates via Equation 4.8,

$$P_{xx}(f) = \sum_{n=1}^{N_s} P_{xx}^{i}(n). \quad (4.8)$$

Welch's method is one of the most commonly used for obtaining PSD estimates, because it reduces noise in the estimated power (Harris, 1978; Welch, 1967) and has been used by other researchers, e.g., Johnsson et al. (2000), for analyzing periodic/chaotic signals. For our data, each data point was divided into eight equal length segments, and the Hamming window with no overlap was used. No identifiable differences were observed when other commonly used window

functions, e.g., the Hanning window, were used (Harris, 1978). All data were processed with MATLAB.

4.3.3. Results

Gas holdup and bubble count (STR equipped with a RT)

Figure 4.8 shows the gas holdup and bubble count profiles for the five radial positions we investigated.

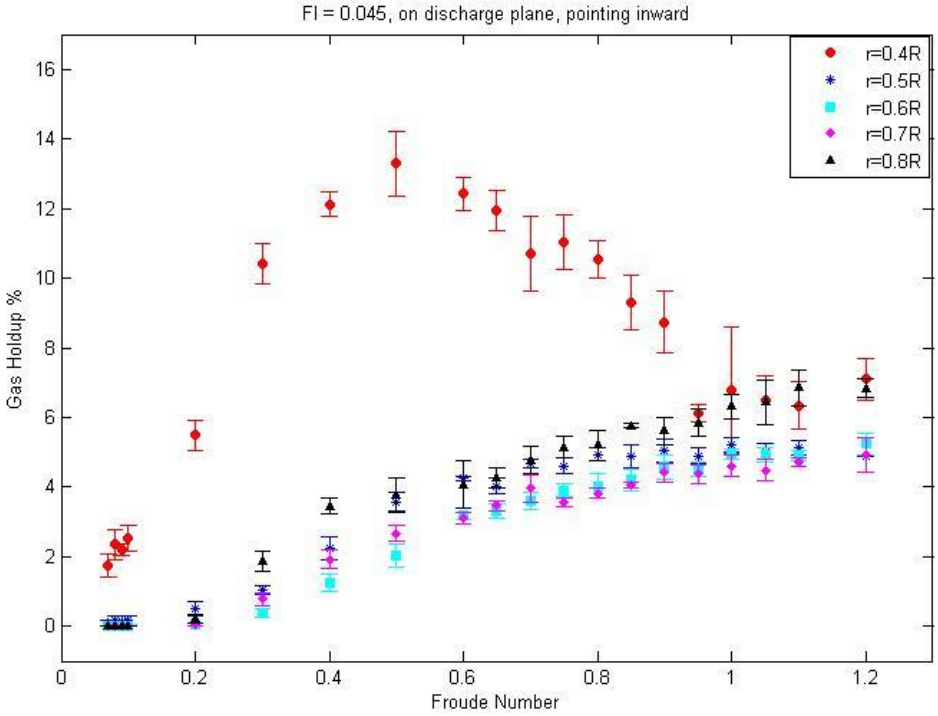

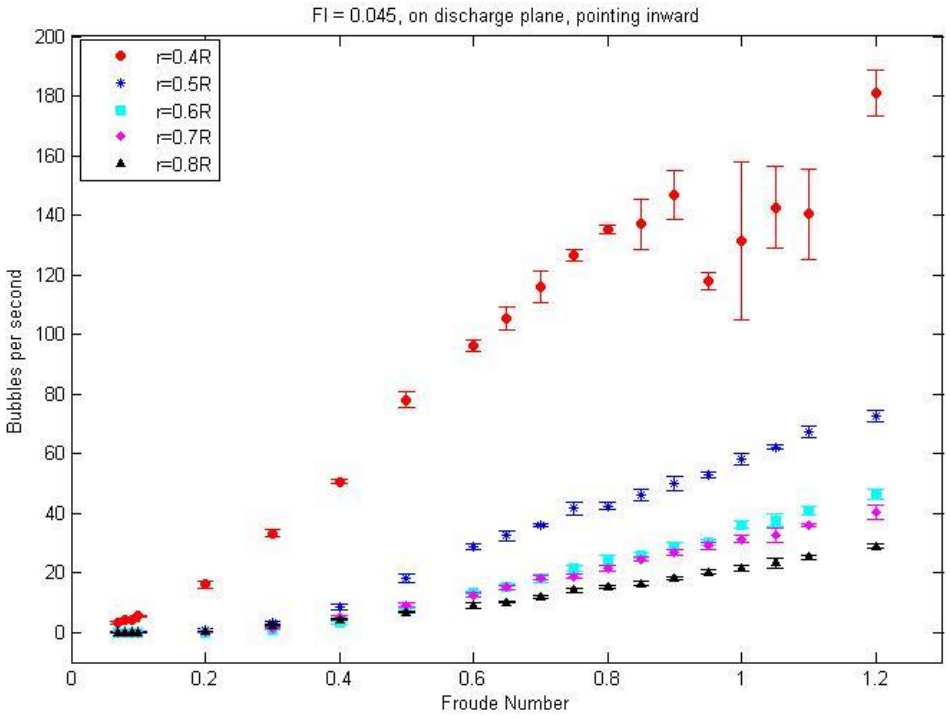

Figure 4.8: Gas holdup and bubble count profiles for the gas-liquid STR equipped with a RT.

As the flow regime transitioned from a less to a more dispersed state, i.e., increasing the *Fr* number while holding the *Fl* number constant, the time domain analyses revealed a linear relationship between the *Fr* number and the two parameters, the gas holdup and bubble count, for the regions r $\geq 0.5R_{STR}$. This finding agrees well with our intuition and what has been argued in the literature, e.g., Kong et al., 2012, regarding the relationship between the flow regime and the gas phase dispersion: The more dispersed the flow regime, the higher the gas holdup and the larger the number of bubbles in the impeller discharge plane. At r = $0.4R_{STR}$, however, such a relationship was not observed. The gas holdup initially increased up to *Fr* = 0.5, then decreased up to *Fr* = 0.95, and then increased again up to *Fr* = 1.2. Accordingly, the differences between what was observed in the region close to the impeller (r = $0.4R_{STR}$) and the region farther away (r

$\geq 0.5R_{STR}$) initially increased up to Fr = 0.5, decreased up to Fr = 0.95, and became insignificant at $Fr \geq 0.95$. At Fr = 0.95, a sudden drop of bubble counts was observed.

Comparatively higher gas holdups observed at r = $0.4R_{STR}$ have been previously reported by means of γ and X-ray CT measurements (Ford et al., 2008; Kong et al., 2012) and are due to a combination of several rheological effects, which include the extension of cavity structures, dispersions by the velocity field near the impeller rather than from the cavities, and bubbles leaving the radial flow stream before reaching the outer regions. Which one of these effects is most significant was not investigated here, but it is clear that these effects initially increase up to Fr = 0.5, decrease up to Fr = 0.95, and completely disappear beyond this point.

When r $\geq 0.5R_{STR}$, the gas holdups were found to stay relatively constant regardless of the operating conditions, which is also in agreement with what has been observed with γ and X-ray measurements (Ford et al., 2008; Kong et al., 2012). This agreement suggests that once the bubbles leave the region close to the impeller (r = $0.4R_{STR}$), the majority of them are not dominated by the aforementioned rheological effects. Considering gas holdup, two regions therefore exist in the flooding and the loading regimes: the inner region, where comparatively higher gas holdup is observed, and the outer region, where relatively constant gas holdup is observed. For the system investigated here, the boundary lies in between $0.4R_{STR}$ < r < $0.5R_{STR}$. After the flow regime transitions to the fully recirculated regime, the boundary disappears.

As mentioned in the previous section, under our experimental conditions of Fl = 0.045, the transition from the loading to the fully recirculated regime takes place at $Fr_{Loading}$= 0.91, where our results show the disappearance of the distinction between the inner and outer regions at r =

$0.4R_{STR}$. This disappearance most likely is caused by newly developed stronger recirculation loops below and above the impeller discharge plane, and by newly created interactions between the new bubbles and the recirculated bubbles. Sudden drops in bubble count at Fr = 0.95 at r = $0.4R_{STR}$ confirm such conclusions regarding the change of the flow behavior as the flow regime transitions into the fully recirculated regime. Since the homogenization of gas holdups on the impeller discharge plane (where our probes were employed) was observed to be a unique property of the fully recirculated regime, this criterion may be used for detecting the transition to the fully recirculated regime.

Gas holdup and bubble count (STR equipped with a CDT)

The gas holdup and the bubble count profiles for the STR equipped with a CDT differed in several aspects. While the magnitude of the effects that caused higher gas holdups in the inner region lessened - as evidenced by smaller differences in gas holdups at different radial positions - a linear relationship between the *Fr* number and gas holdup was not observed at any radial position. No conclusion regarding the inner and the outer region was thus made, based on gas holdup measurements.

For bubble counts, on the other hand, the linear relationship between the *Fr* number and bubble count was observed at all ranges of operating conditions and at all radial positions investigated, i.e., as the degree of dispersion increased, so did the number of detected bubbles. No sudden drops were observed at any positions, and the closer the probe was to the impeller, the more bubbles that were detected. Figure 4.9 shows the gas holdup and bubble count profiles for the STR equipped with a CDT.

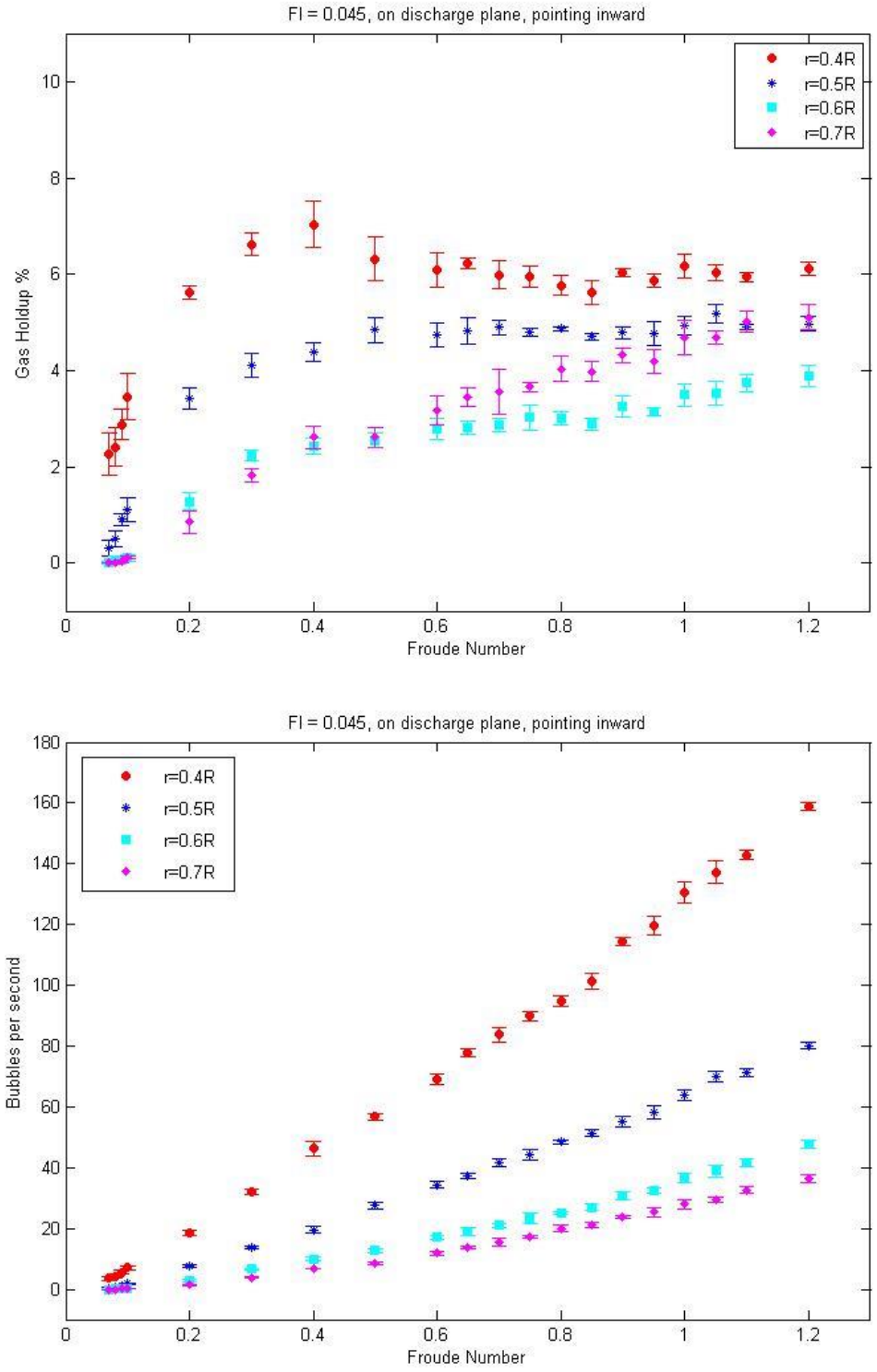

Figure 4.9: Gas holdup and bubble count profile for the STR equipped with a CDT.

The advantages of using hollow blade impellers (including the CDT) for better intra- and inter-phase mixing and more efficient gas dispersions over the RT in single and multiphase STRs have been reported in the literature for some time (Bakker et al., 1994; Vasconcelos et al., 1999; Revstedt et al., 2000; Smith and Gao, 2001; Li et al., 2013). Some of the reported disadvantages of a RT include a significant drop in relative power demand (RPD, the ratio of the power drawn in a gas-liquid system to the power drawn in a liquid system), which may lead to the loss of effective heat and mass transfer; higher impeller rotational speeds needed to transition into a more dispersed flow regime; and comparatively smaller gas handling capacities (Vasconcelos et al., 1999). Comparing the two gas holdups obtained at the same operating conditions and positions (Figure 4.10), our results agreed well with such conclusions in the *Fr* range up to 0.45. More bubbles were capable of traveling towards the reactor wall, and as a result, higher gas holdups were observed at $r \geq 0.5R_{STR}$ for the STR equipped with a CDT. As the flow regime transitioned to an even more dispersed regime ($Fr > 0.45$), however, no evidence for more effective dispersion was detected. Within the region covered by our probes, higher gas holdups were obtained for the STR equipped with a RT at $r = 0.6R_{STR}$.

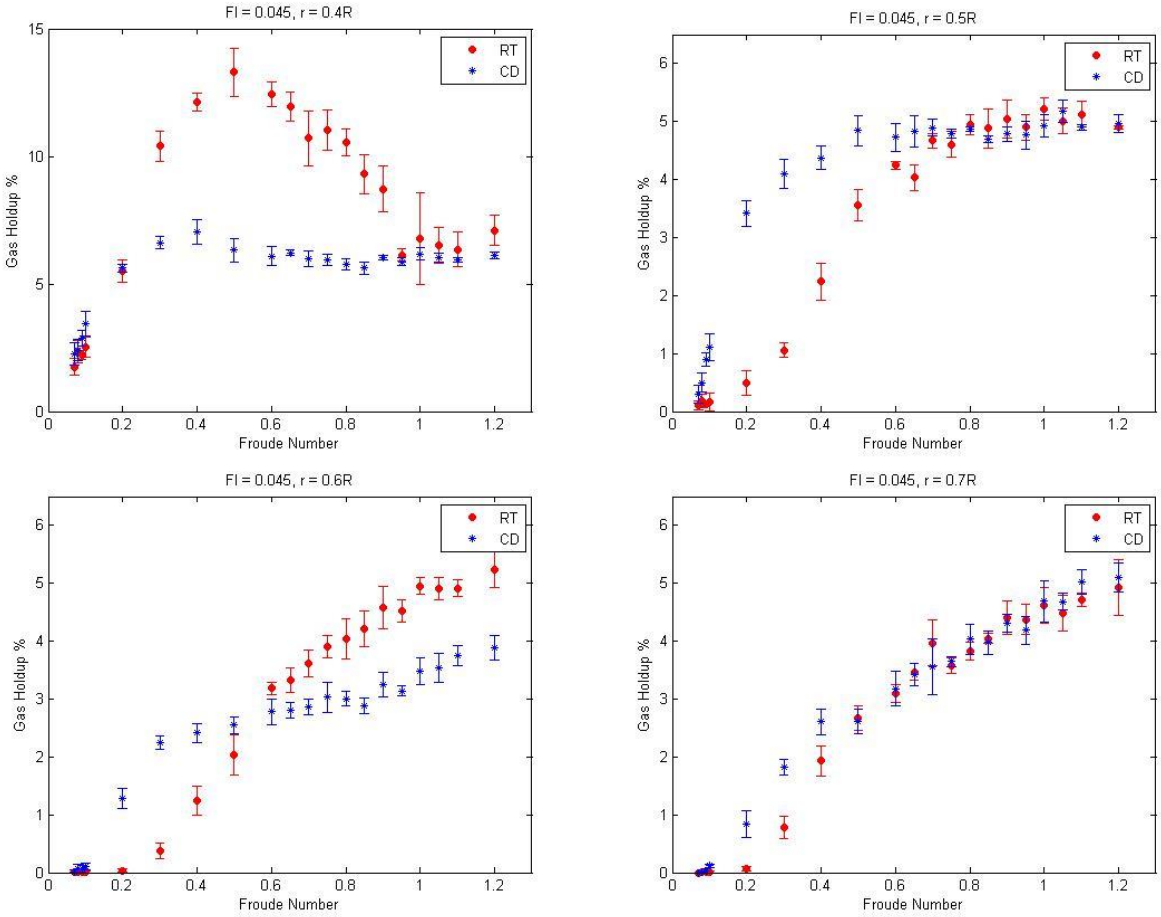

Figure 4.10: Comparisons of gas holdup values at four radial positions for STRs equipped with a RT and a CDT.

Autocorrelation sequence and power spectral density (PSD) estimates

The structures of the cavities formed behind the RT blades have been well identified by numerous researchers, e.g., Warmoeskerken and Smith (1985), and summarized by Rammohan (2002), yet whether the periodic behavior of dispersed bubbles persists throughout the reactor has not been given much consideration. However, since one of the most important parameters in gas-liquid STRs (as well as other multiphase reactors) is interfacial contacting, identifying the region and the condition at which the bubbles lose their cavity identity (due to coalescence / breakage, liquid / bubble velocity, bubble size, etc.) is of importance for a meaningful

description of the impeller's and the reactor's performance. In this section, autocorrelation sequences and PSD estimates from the optical probe measurements are presented, and the transitions from the periodic to the chaotic nature of bubble occurrences at different radial positions and operating conditions are discussed.

R_{xx} and PSD for STR equipped with a RT

For the STR equipped with a RT, the cavities behind the impeller blades follow the shapes of the trailing vortexes, and are classified into six structures: vortex clinging (VC), clinging cavities (1L), two large cavities (2L), three large and three clinging cavities (S33), three smaller and three larger cavities (L33), and ragged cavity (RC) structures, as was shown in Figure 4.4.

At our experimental condition of Fl = 0.045, as the Fr number increases from 0.07 to 1.2, the cavity structures change from the RC structures to the S33 structures, and the flow regime transitions from the flooding to the loading and then to the fully recirculated regime at Fr values of 0.1, 0.07, and 0.91, respectively.

Shown in Figure 4.11 are the autocorrelation sequences at five radial positions for all operating conditions we investigated. In these figures, the time lags for autocorrelation sequences are normalized with respect to the impeller motion since the main mechanism for bubble dispersion is from the cavity break up. Each line therefore represents a different time scale: the higher the Fr number, the shorter the actual time lags in unit time.

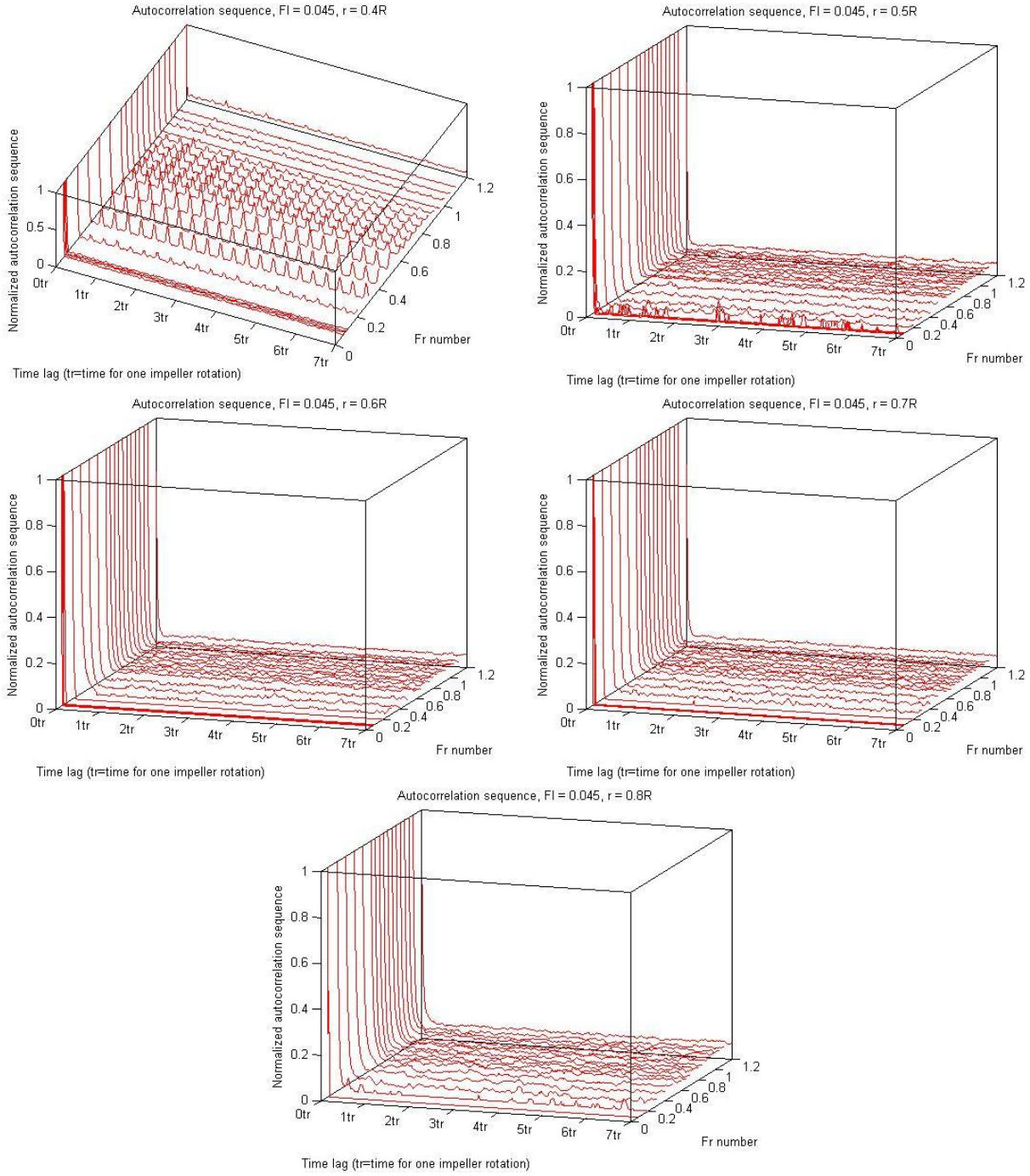

Figure 4.11: Autocorrelation sequences as a function of the normalized time lag (with respect to impeller motion) and the Fr number at five radial positions (r = $0.4R_{STR}$., $0.5R_{STR}$., $0.6R_{STR}$., $0.7R_{STR}$., $08R_{STR}$.) for a STR equipped with a RT.

For all operating conditions, a fast decay near zero time lag was followed by nearly constant autocorrelation sequences. The rate of decay was inversely proportional to the impeller rotational rate only for the probe that was positioned nearest to the impeller, r = $0.4R_{STR}$, at $Fr \leq 0.95$. At this position and at these conditions, periodic sequences were observed at the multiples of $1/3t_r$ (t_r = time for one impeller rotation), with the highest peak amplitude at the multiples of t_r.

As the *Fr* number increased (moving across the y-axis), the peak amplitudes increased up to *Fr* = 0.5 and then decreased up to *Fr* = 0.95. At Fr numbers higher than 0.95, i.e., when the flow regime has transitioned into the fully recirculated regime, periodic sequences were not observed. At all other positions, no correlations were observed.

These results are in accordance with what was concluded in the previous section regarding the presence of two regions within the impeller discharge plane, the inner and the outer regions, and the disappearance of the boundary at r = $0.4R_{STR}$ as the fully recirculated regime onsets at $Fr_{Loading}$= 0.91. In the inner region, where higher gas holdups are observed, bubble occurrences are strongly correlated to the impeller movement (thus cavity structures); in the outer region, where gas holdups do not change significantly, no such correlations exist.

PSD estimates revealed similar information regarding the periodic / chaotic nature of bubble occupancy, perhaps more obviously than the autocorrelation sequences. Figure 4.12 shows the PSD estimates at two locations, r = $0.4R_{STR}$ and $0.5R_{STR}$.

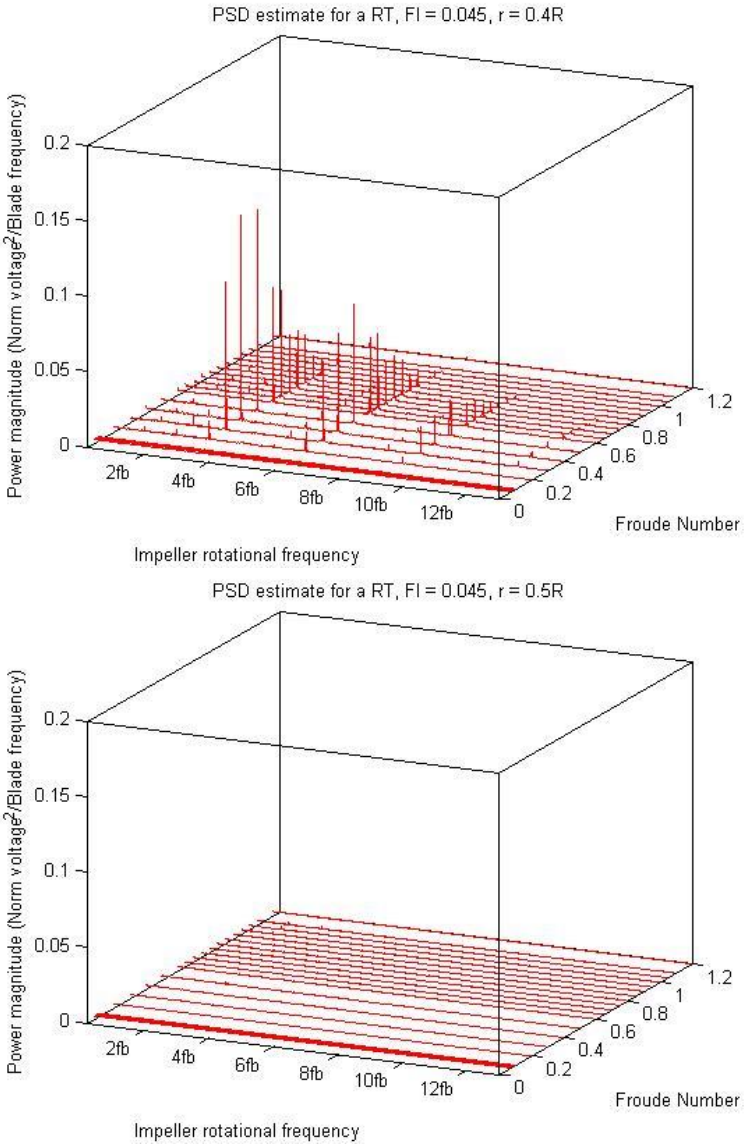

Figure 4.12: Power spectrum density estimate as a function of normalized frequency (with respect to blade frequency) and the *Fr* number. Upper figure from r = 0.4R_{STR}, lower figure from r = 0.5R_{STR}. fb represents rotational frequency of impeller.

Dominant frequencies were observed only for the probe that was positioned at the inner region, r = 0.4R_{STR}, in multiples of 3fb (fb = impeller rotational frequency) with descending power as the fb increased. These PSD estimates match the sub-harmonics of the 3-3 cavity structures observed by Bombac et al. (1997), and therefore confirm bubbles' cavity structure resemblance in the

inner region near the impeller. At the outer regions of r ≥ $0.5R_{STR}$, flat PSD estimates were obtained regardless of the operating conditions. The PSD estimates for the probes that were positioned at r = $0.6R_{STR}$, $0.7R_{STR}$, and $0.8R_{STR}$ are not shown in here since they looked much like the PSD estimates from r = $0.5R_{STR}$, where no dominant frequencies were present.

The disappearance of cavity structural dependence of bubbles at r = $0.4R_{STR}$ in the fully recirculated regime is once again most likely due to newly developed recirculation loops below and above the impeller discharge plane (Figure 4.2). As the *Fr* number increases, more and more of the dispersed bubbles in the outer region are carried back towards the inner region to interact with the cavities and dispersed bubbles; as a result, bubbles lose their cavity identity sooner than before. Since this phenomenon was observed to be a unique property of the fully recirculated regime, positioning an optical probe in the inner reactor region and obtaining either the autocorrelation sequence or the PSD estimate seems to offer one of the simplest, yet robust methods for distinguishing the fully recirculated regime from the loading regime. To the author's knowledge, very few (if any) techniques are capable of detecting this transition.

R_{xx} and PSD for STR equipped with a CDT

The advantages of a CDT over a RT for more effective gas dispersion and larger gas handling capacity are due to enhanced blade streamlining (Bao et al., 2008; Vasconcelos et al., 1999); yet the cavity structures from which the bubbles are dispersed have not been reported, to the author's knowledge. Since the autocorrelation sequences and the PSD estimates for the probe positioned at r = $0.4R_{STR}$ accurately captured the essence of the cavity structures for a RT, the probe located at the same position should reveal similar information regarding the cavity structures of a CDT. Furthermore, if a clear boundary between the inner and the outer reactor zone were to exist

(which was not obvious in the gas holdup profile), a distinct difference should be observed in the autocorrelation sequences and the PSD estimates (as was the case for the STR equipped with a RT). Figure 4.13 and 4.14 show the autocorrelation sequences at four radial positions and the PSD estimates at two radial positions. PSD estimates from two other outer regions are not shown here since they look similar to the one shown at r = $0.5R_{STR}$.

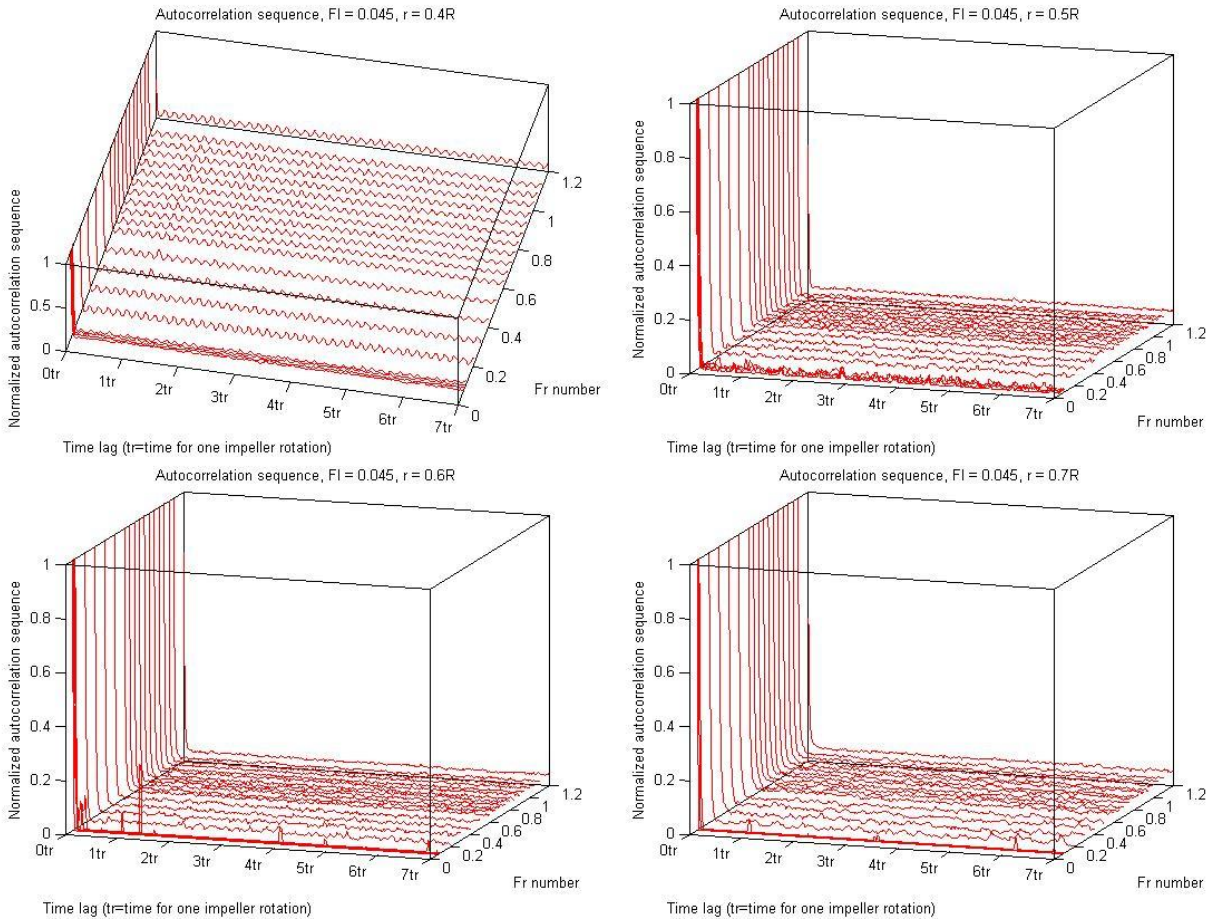

Figure 4.13: Autocorrelation sequences as a function of the normalized time lag (with respect to impeller motion) and the *Fr* number at four radial positions (r = $0.4R_{STR}$, $0.5R_{STR}$, $0.6R_{STR}$, $0.7R_{STR}$) for a STR equipped with a CDT.

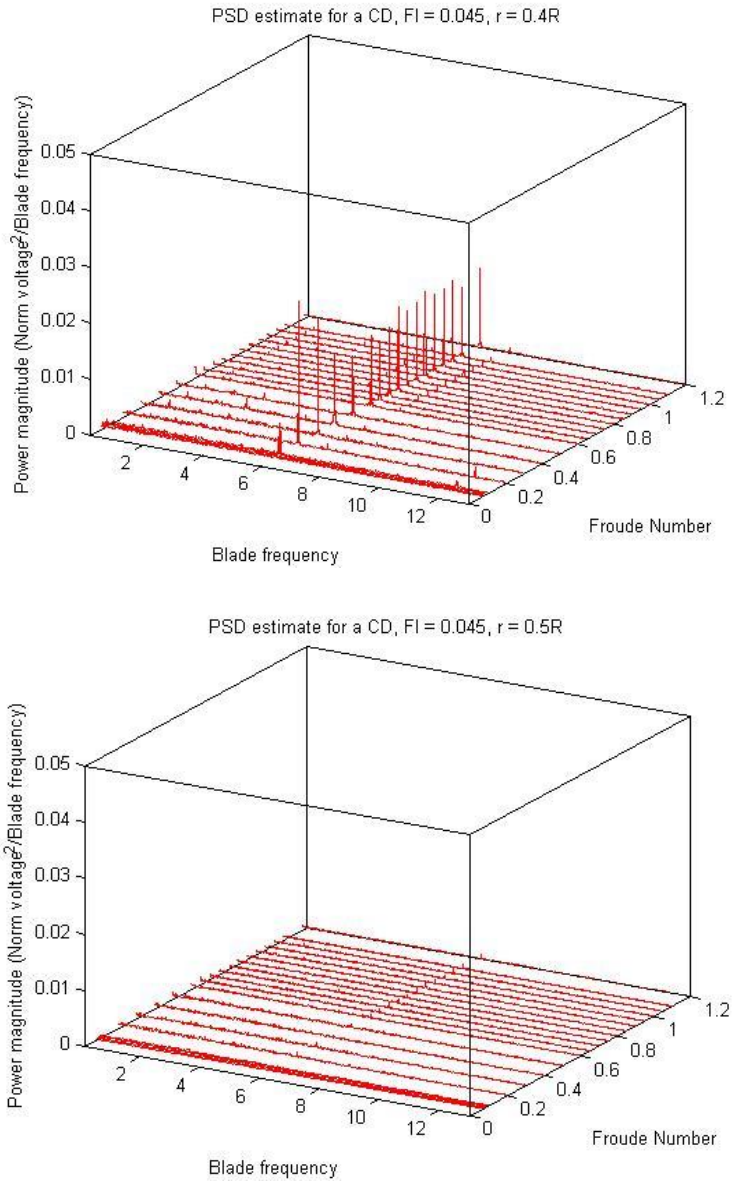

Figure 4.14: Power spectrum density estimate as a function of normalized frequency (with respect to blade frequency) and the *Fr* number. Upper figure from r = 0.4R_{STR}, lower figure from r = 0.5R_{STR}. fb represents rotational frequency of impeller.

Similar to what was obtained in a STR equipped with a RT, a fast decay near zero time lag was followed by near constant autocorrelation sequences at all operating conditions and positions. The rate of decay was inversely proportional to the impeller rotational rate only for the probe that was positioned at r = 0.4R_{STR}, at all operating conditions. Here, periodic sequences were

observed at multiples of 1/6 t_r, with equal peak heights. At all other radial positions where our probes were positioned, no periodic autocorrelation sequences were observed.

PSD estimates revealed only one dominant frequency at 6fb for the probe positioned at r = $0.4R_{STR}$. This finding suggests the cavity structures behind all six blades were of the same size and structure regardless of the flow regime, under our experimental condition of *Fl* = 0.045.

The results from the autocorrelation sequences and PSD estimates suggest the presence of two regions within the impeller discharge plane, even for a STR equipped with a CDT: the inner region, where bubble occurrences are strongly correlated to the impeller movement (and thus to cavity structures), and the outer region, where this is not the case. While the differences and demarcation boundary between the two regions were not obvious in the time domain analyses, a clear boundary marked by the disappearance of bubbles' cavity structural dependence was observed between r = $0.4R_{STR}$ and $0.5R_{STR}$.

The boundary between the inner and the outer regions at $0.4R_{STR} \leq r \leq 0.5R_{STR}$ was found to persist even after the flow regime has transitioned into the fully recirculated regime. For the STR equipped with a CDT, the transition from the loading to the fully recirculated regime is known to occur at a *Fr* number less than 0.91 (Bakker et al., 1994), yet the periodic sequences are observed for all operating conditions up to *Fr* = 1.2. This is most likely due to enhanced blade streamlining and the recirculated bubbles' inability to strongly interact with the bubbles in the flow stream at r = $0.4R_{STR}$. While the advantages of the CDT in the fully recirculated regime were not clear in the time-domain analyses, the autocorrelation sequences and PSD estimates

revealed stronger persistency of cavity-like nature of bubbles near the impeller, which may lead to larger interphase contacting.

4.4. Conclusions

Treatment of optical probe measurements in STRs equipped with a RT and a CDT in the time and the frequency domain revealed an inner and an outer region within the impeller discharge plane.

For the STR equipped with a RT, two zones were identified in both the time and frequency domain analyses. In the inner reactor zone, at r = $0.4R_{STR}$ (0.67cm away from the impeller blade tip), higher gas holdups and strong correlations between the bubbles and impeller motions were observed. Once the flow regime had transitioned into the fully recirculated regime ($Fr \geq 0.91$), the boundary between the inner and the outer reactor region disappeared in the region where our probes were employed. In the outer reactor region, the gas holdup values were found to be similar regardless of the radial position, and bubble occurrences were not correlated to the cavity structures. While the existence of two regions on the impeller discharge plane was previously reported by means of other measurement techniques (Ford et al., 2008; Kong et al., 2012), the disappearance of the boundary as the flow regime transitions to the fully recirculated regime has not. Since homogenization of gas holdup and the disappearance of bubbles' correlations to the impeller motion (and thus to cavity structures) at r = $0.4R_{STR}$ were unique characteristics of the fully recirculated regime, the technique and the methods presented in this chapter may be used to determine the flow regime transition from the loading regime to the fully recirculated regime. Moreover, the observed relationships between the *Fr* number and the two parameters showed

their potential usefulness as a key method for fast in-situ determination of the overall STR state of dispersion (flow regime).

For the STR equipped with a CDT, two zones persisted throughout the operating conditions we investigated. While the time domain analysis did not provide a clear insight regarding the existence of two regions, the frequency domain analysis revealed a clear distinction in bubble behavior between the inner and the outer regions. The optical probe positioned at r = $0.4R_{STR}$ effectively captured the essence of cavity structures behind the impeller blades.

Chapter 5. Summary of findings and recommendations for future work

This work investigated optical probe techniques' usefulness in different types of multiphase reactors. The three major contributions are: 1) the development of the Optical Probe Probabilistic Model (OPPM), 2) the model's application as an investigative tool for gas phase backmixing in bubble column reactors, and 3) the development of new analytical methodology for optical probe measurements in gas-liquid stirred tank reactors. Since they were first introduced to study multiphase reactors circa 1980s, optical probes have been widely adapted by numerous research groups for a number of purposes some of which were employed in this work. The research described here looks more closely as to the richness of information that they can provide.

The following sections summarize the key contributions and discuss how these findings can further be extended for better design, modeling, and scale-up of multiphase reactors.

5.1. The Optical Probe Probabilistic Model (OPPM)

We formulated a probabilistic model that makes use of the optical probe's invasiveness, which is otherwise considered a key disadvantage. The model assumes two things and makes use of experimental measurements collected at two opposing orientations of the optical probe. The two assumptions are: 1) All bubbles travelling within 90° of impact angle (θ) are captured by the probe, and 2) only a fraction of the bubbles traveling at larger angles are captured by the probe. To verify the results from the model, two methods were employed:

1. The results from different sets of measurements were compared to see if they gave the same “unbiased” local gas phase holdups and bubble counts.

2. Using a 2-D bubble column, the results from the OPPM and high speed camera (HSC) were compared.

The model was developed and applied for the optical probe technique; however, the same methodology can be extended to any other ‘needle-like’ techniques that are invasive, such as the resistivity probe used by Bombac et al. (1997).

The OPPM is particularly useful for reactor design, modeling, and scale-up because it can provide – for the first time – novel information about whether the addition or removal of certain reactor features, and/or scaling up or down, changes the local gas phase dynamics.

This model is useful as it is, what would be even more useful is a full understanding of how the degree of invasiveness, i.e., a change in the optical fiber size and/or metal sheathing, impacts the overall directional sensitivity of the probe. For the OPPM, the greater the directional sensitivity, the easier it is to solve the model equations. This improvement can be made in two ways, experimentally and theoretically. Experimentally, one can obtain and compare the results from different-sized fibers and metal sheathings. Theoretically, one can employ detailed multiphase fluid dynamics principles, e.g., CFD, for better understanding of the piercing mechanisms. Either or both these results can then be utilized to find the optimal optical fiber and sheathing sizes for the model’s applications in multiphase reactors operating at different conditions.

5.2. Gas phase backmixing in bubble column reactors

After the OPPM was developed, the optical probe and the developed model were employed in an air-water lab-scale bubble column reactor to elucidate the very complex gas phase dynamics. Several heights and radial positions were investigated, and the local gas phase backmixings – the fraction of gas phase bubbles traveling downward – were quantified. The volume of expansion method identified the transition between the homogeneous (bubbly), transition, and heterogeneous (churn-turbulent) flows, as well as the measured backmixing related to this global reactor hydrodynamic behavior.

The results revealed distinct hydrodynamics for the gas phase, when compared to the liquid and solid hydrodynamics previously reported in the literature. The most notable findings for the 10-cm bubble column reactor we investigated include:

1. Gas phase backmixing increased for all radial positions as U_{gas} increased in the homogeneous flow regime.

2. As the flow regime transitioned to the transition flow regime, gas phase backmixing remained very high.

3. The non-monotonic overall gas phase holdup profile as a function of gas phase superficial velocity for the transition flow regime was effectively captured at all heights investigated.

4. In the heterogeneous flow regime, the measured gas phase backmixing revealed close to PFR-like behavior in the mid-column zone. In the entrance and exit zones, CSTR-like behavior was observed.

The observed PFR-like behavior for the mid-column zone in the homogeneous and heterogeneous flow regimes versus CSTR-like behavior in the transition flow regime suggests a new way to look at the gas phase dynamics (modeling). Previous studies using global reactor measurements revealed monotonically increasing axial dispersion coefficients (Han, 2007; Hamed, 2012) as the flow regime transitioned to more dispersed regimes. Having a larger axial dispersion coefficient in the ADM does not necessary mean higher degree of backmixing; however, people often correlate the two things.

To fully incorporate these findings into successful reactor modeling and scale-up for industrial bubble column reactors, we need a mathematical model based on fundamentals to relate the experimental results to local dispersion coefficients like was done for liquid backmixing models developed by Degaleesan (1997). Moreover, the introduced methodology needs to be extended to bubble column reactors of different scales and operating conditions, and the boundaries between the entrance, mid-column, and exit zones need to be more precisely identified by deploying the optical probe and the OPPM at more axial positions.

5.3. Time-series analysis of the optical probe technique

Chapter 4 described the application of time-series analysis methods on the optical probe measurements collected in a lab-scale gas-liquid STR. The time and frequency domains were

particularly useful for the measurements made in the STR equipped with a Rushton turbine (RT) or a half circular blades disk turbine (CDT).

For the STR equipped with a RT, results from both the time and frequency domains revealed the existence of an inner and an outer region with respect to gas phase dynamics. Gas holdup and bubble count profile increased linearly as the *Fr* increased while holding *Fl* constant. As the flow regime transitioned to the most dispersed and turbulent fully recirculated flow regime, however, both parameters dropped significantly before monotonically increasing again. The inner region showed significantly higher gas holdup and bubble count profiles in the flooding and loading regimes; in the fully recirculated regime, the gas holdup values were nearly identical to those in the outer region. Similarly, the R_{xx} and PSD revealed a clear distinction between the two regions only in the flooding and loading regimes. As the flow regime transitioned into the fully recirculated regime, the distinction disappeared, and the two regions were homogenized.

For the STR equipped with a CDT, the distinction between the inner and outer regions persisted within the radial positions we investigated. A linear relationship was found only for the bubble count profile when plotted as a function of *Fr*, while holding *Fl* constant. The gas holdup profile did not reveal any notable trend.

These results reveal the optical probe's potential as an investigative and control tool in industrial gas-liquid STRs equipped with a RT. Optical probes can be employed in any medium, given sufficient protection at the tip; therefore, in processes where detecting the flow regime transitions to fully recirculated regime is critical, e.g., bioreactors, employing the optical probe in the inner region and monitoring the signal in the frequency domain will ensure continuous and successful operation.

Further research is needed for the STR equipped with a CDT, because the same distinction was not observed in the regions we investigated. This research can be performed by employing the optical probe in more radial positions between $0.4R_{STR}$ and $0.5R_{STR}$, and by applying the same methodologies introduced. Moreover, the results from the STR equipped with a RT – the disappearance of the inner and outer zone distinction – can be set as a criterion for CFD model validation.

Appendix A. Optical probe usage in multiphase reactors

Because optical probes can be made very small, they are considered one of the two micro-probes currently available, the conductivity probe being the other (Xue, 2004). As the name suggests, a conductivity probe measures the conductivity of its immediate surroundings, while an optical probe measures their refractive index.

Optical probes offer simple setup, easy signal interpretation, a low signal to noise ratio (compared to the conductivity probe), and a wide range of operable temperature and pressure conditions (Xue, 2004; Julia et al., 2005). Capitalizing on these advantages, optical probes have been used by CREL researchers to describe complex multiphase phenomena in multiphase reactors, e.g., bubble columns, slurry bubble columns, air-water stirred tanks, and gas-expanded liquids. Specifically, three tip configurations, shown in Figure A.1 (2.2), have been developed and employed in multiphase reactors.

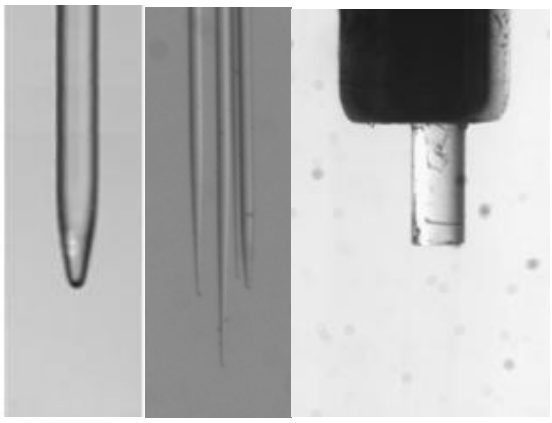

Figure A.1 (2.2): Optical probe tip types (left, single point; middle, four point; right, flat ended).

For an optical probe system used in CREL (Figure A.2), light is introduced into the fiber after passing through a collimator. A collimator is a lens device which narrows light beams, allowing more light to enter through the fiber core. The more light there is in the fiber, the less noise in the result obtained by the photodiode. Generally, monochromatic light is preferred over polychromatic.

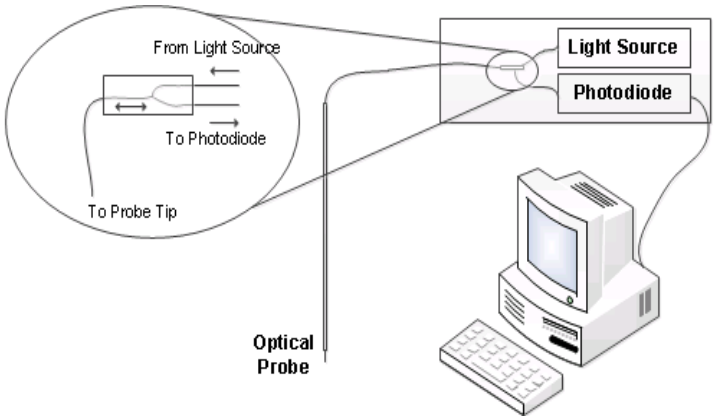

Figure A.2 (2.1): Optical probe technique setup.

A light wave travelling through an optical fiber is known to propagate according to Snell's law. At a phase boundary, Snell's law describes the refraction/reflection phenomena and states $n_1 \cdot \sin(\theta_1) = n_2 \cdot \sin(\theta_2)$, where n_1, n_2, θ_1, and θ_2 represent refractive indexes and angles of incidence with respect to axis normal to the interface. For example, for fibers with a glass core refractive index of $n_1 = 1.463$ and a cladding refractive index of $n_2 = 1.460$, the total reflection occurs at angles less than $\theta_c = \theta_i = \arcsin\left(\frac{n_2}{n_1}\right) = \arcsin\left(\frac{1.460}{1.463}\right) = 1.507\ radians = 86.33°$. Light rays traveling only at angles higher than this value will reflect internally to reach the optical fiber tip. While Snell's law gives a simple representation of the behavior of light, one must note that light propagation is much more complicated, and a full solution to Maxwell's equation should be obtained for a full interpretation.

Since only a small portion of light is allowed to transmit through the core at large angles normal to the cladding-core interface, the light propagation in fibers is often represented as shown in Figure A.3.

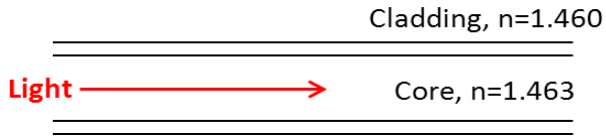

Figure A.3: Ray representation of light propagating in optical fiber.

During the past couple of decades, fiber ends have been shaped into different shapes for their usage in multiphase systems / reactors. Some of these tips are shown in figure A.4. In the upper figures, the amount of light reflected, R, compared to the amount of light emitted, E, largely depends on two things: the refractive index of the surrounding medium and the light contact angle. For detailed optical physics calculations for each of the tips, readers are directed to Cartellier and Achard (1991); Fordham et al. (1999a); Fordham et al. (1999b); Fordham et al. (1999c).

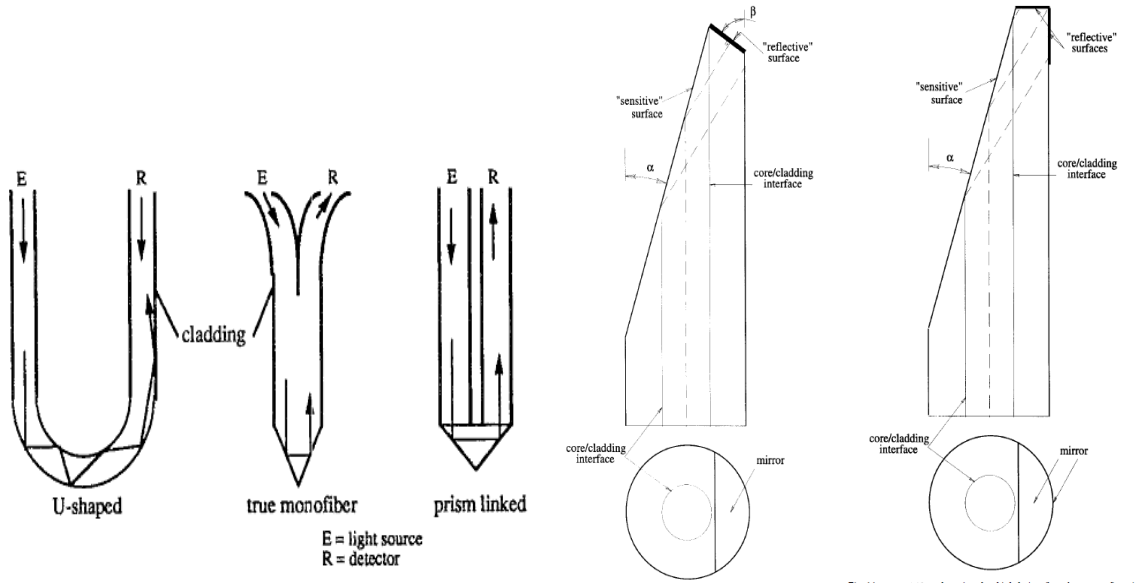

Figure A.4: Various optical fiber geometries. [source: Cartellier and Achard (1991) – left figure, Ramos and Fordham (1999) – right figure)].

Since an optical probe must see its medium to detect refractive index differences, optical probes are intrusive and may alter the flow. To minimize such effect, advances in optical probe technique have concentrated on reducing the overall dimensions of optical fibers; the smaller the tip size, the less the disturbance. In CREL, a true monofiber type was therefore chosen for all applications.

A.1. Tapered end optical probes

For a tapered end optical probe (monofiber) employed in gas liquid containing reactors, the probe's characteristic step response to a bubble is shown in Figure A.5. The response is caused by difference in the refractive index of gas and liquid phases and the contact angle between the medium and the tip.

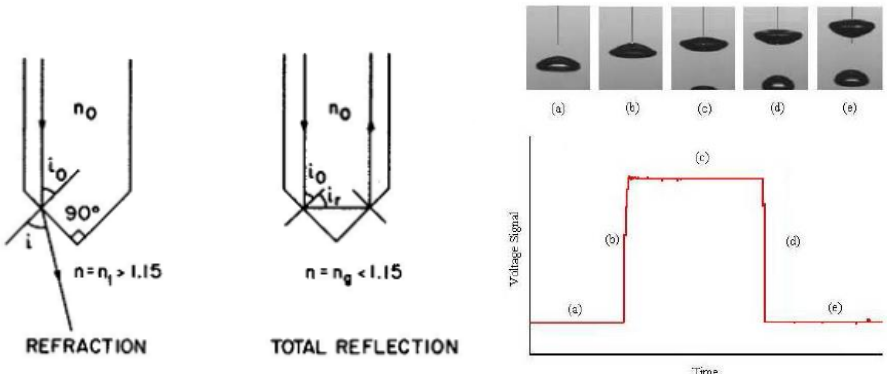

Figure A.5: Refraction and reflection of a monofiber type with the conical end (left) and the characteristic step response of a bubble (source: Mueller, 2009).

Based on this principle of total reflection versus refraction and by applying the ergodic theorem (which states that the volume-averaged holdup can be represented by the time-averaged measurement), a single point optical probe is therefore able to capture three key parameters when employed in an air-water system: local gas holdup, bubble count, and bubble residence time distribution. In equation form, the ergodic theorem states,

$$\varepsilon_{gas,local} = \frac{V_{gas,local}}{V_{liquid,local}+V_{gas,local}} = \frac{t_{gas}}{t_{liquid}+t_{gas}} \quad \text{(A.1)}$$

where ε is the phase holdup, *V* is the volume fraction, and *t* is the amount of time spent in a particular phase. This method has been extensively used by many researchers in the field to convert time-series point measurements to volume fraction measurements, e.g., Bombac et al. (1997); Hamad et al. (1997); Fordham et al. (1999a); Fordham et al. (1999b); Fordham et al. (1999c); Bombac and Zun (2000); Hamad et al. (2000); Gao et al. (2001); Rogerio et al. (2001); and Bombac and Zun (2006). For bubble count, number of signal jumps (or drops) can be counted; for bubble residence time distribution, the amount of time spent per bubble can be plotted.

In our group, Xue (2004) and Mueller (2009) also used the same fiber type to make the four-point optical probe for estimation of bubble size and bubble velocity distributions in bubble column and stirred tank reactors.

A.2. Four point optical probes

A four point probe makes use of four tapered end optical fibers and was originally developed at the University of Delft by Frijlink (1987) and his colleagues. Years later, after noting too many restrictions in the old algorithm, Xue (2004) improved the probe's algorithm to capture more bubble dynamic information. The beauty of the new algorithm lies in the fact that the probe does not need to be aligned opposite to the direction of the flow (Mueller, 2009).

A 4-point probe is made by positioning four adjacent tapered end fibers of different lengths so their tips form a tetrahedron in the configuration as shown in Figure A.6, and sheathing them in a

metal jacket. Signals from all fibers are recorded simultaneously, and the signals are used to calculate detailed bubble dynamics: bubble velocity distribution, chord length distribution, approach angle distribution, and interfacial area.[7] The new 4-point probe MATLAB algorithm is given in Appendix C.

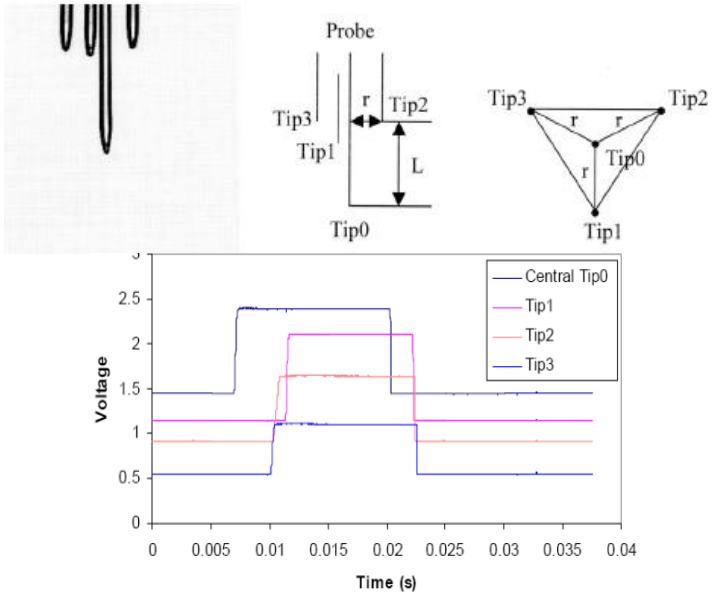

Figure A.6: Top: four point probe configuration, bottom: signal due to bubble striking the probe (source: Xue, 2004).

A.3. Flat end optical probes

Interpreting signals from a flat end optical probe is a very complex task as the amount of light reflected back depends on three things: 1) refractive index of the surrounding medium, 2) how much of the measuring (flat) area is in contact with which medium, and 3) which part of the measuring area is touching the medium, which are not easily observable or measurable. Despite the complexity, flat ended probes have been found to be valuable for several systems: Rogerio et al. (2001) combined their fiber with a fluorescence probe to estimate the volume fractions of

[7] Detailed equations and the algorithms are given in Xue (2004) and Mueller (2009).

each phase in an oil-water-gas system; Avdeev et al. (2004) used their probe to detect density changes in gases, liquids, and supercritical fluids; Piela et al. (2009) used their probe in an oil-water-gas pipe to determine the gas phase volume fraction; and Bao et al. (2015) used their robe to detect bubble and dew point for multicomponent systems.

In very simple gas-liquid, liquid-liquid, and three-phase systems (e.g., Fordham et al., 1999a; Fordham et al., 1999b; Fordham et al., 1999c), theoretical amount of reflected light was calculated using the Fresnel equation, which states

$$R_s = R_p = \left[\frac{n-1}{n+1}\right]^2 \qquad \text{(A.2)}$$

where $n = \frac{n_2(refractive\ index\ of\ the\ medium)}{n_1(refractive\ index\ of\ the\ fiber)}$ and R = fraction of the light energy reflected. However, in practical systems, a full understanding of fluid dynamics and inter- and intra-phase mixing using flat end optical probes is a formidable task, with a great many assumptions. Mizushima et al. (2013) elegantly developed a 3D computational ray tracing methods to track "enormous ray segment trajectories" and applied it to their wedge shape optical probe. Nonetheless, the application of similar methods to flat end probe in multiphase systems is questionable, because too many assumptions need to be made. Recent study by Sun et al. (2013) made in our CREL shows how a novel probe design was developed and the complexity of signals used to infer information on phase miscibility.

Appendix B. Checking for signal bimodality for tapered end optical probes[8]

In theory, the tapered optical fibers should result in binary signal distribution when employed in gas-liquid systems. However, several reviews pointed out some sources of error (Cartellier, 1990, 1992; Cartellier and Achard, 1991; Julia et al., 2005) caused by the deformation of the phase interfaces at the probe tip. The error was found to always translate into longer rise and fall times, i.e. the time needed for the signal to rise from the liquid level to the gas level and vice versa. In this section, two major sources of errors outlined in these reviews are summarized, and several signal distributions from results presented throughout this dissertation for discussion regarding the accuracy of the results.

B.1. Sources of error

B.1.1. Piercing near the bubble edge

Julia et al. (2005) investigated in detail the effect of piercing position on the rise and fall response curves. The results suggest that when the probe tip pierces the bubble near the edge, i.e. away from the equator, interpreting the raw signal as if the signal was binary (one for liquid, one for gas) and arbitrarily setting the cutoff-level somewhere in between the two levels may result in non-negligible error. The cutoff-level, or the signal criterion level, is the signal level at which

[8] Material in this chapter was previously published in Lee and Dudukovic (2014a).

the probe is considered to be completely immersed in the gas. Sample signal shapes as a function of piercing location are shown in Figure B.1.

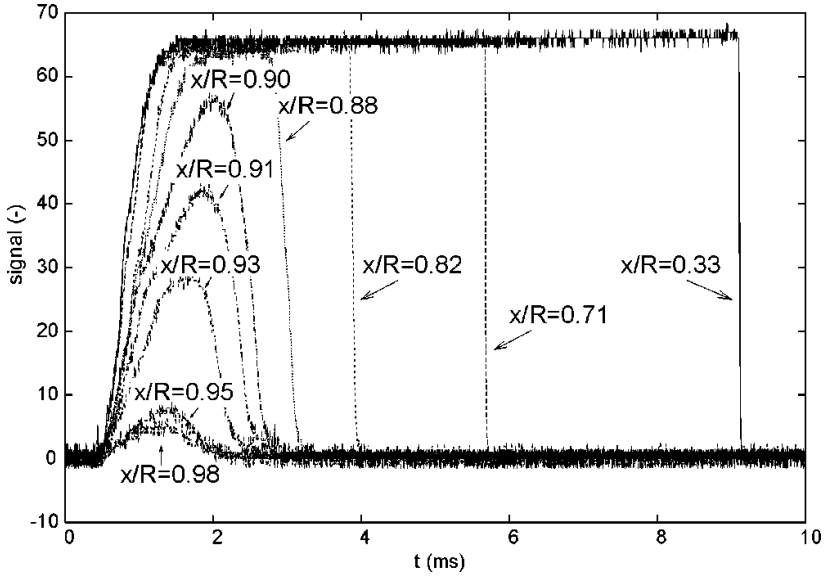

Figure B.1: Signal shapes at various piercing positions for ellipsoidal bubbles traveling in shorter axis' direction. x represents the distance away from the center of the bubble (source: Julia et al., 2004).

Signals of full amplitudes were found to be only observed for $x/R < 0.9$ and bell shaped signals were observed for $x/R > 0.9$, due to the wetting and de-wetting phenomena of the probe tip and their complex interaction with the light. Additionally, partial blinding effect associated with the bell shaped signals was also introduced. Figure C.2 shows this effect.

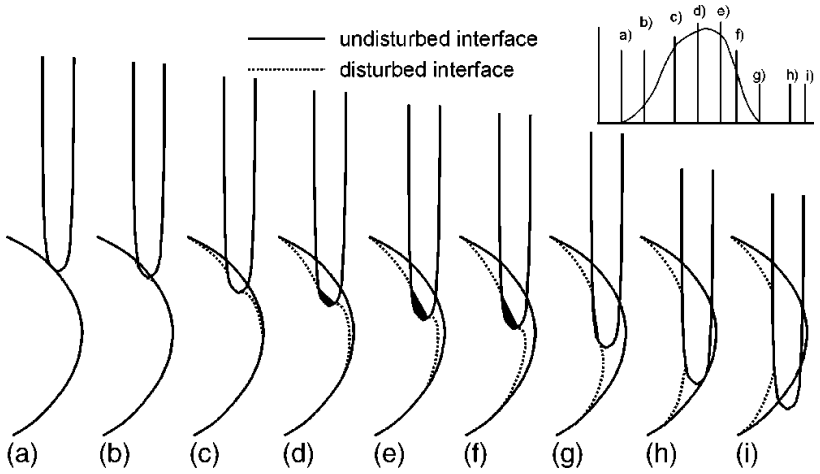

Figure B.2: Piercing of a bubble near the bubble edge and the blinding effect (source: Julia et al., 2004).

While the full optical-physics calculations are required for a thorough explanation, so is the complete description of the wetting/de-wetting fluid dynamics. Due to the difficulty of determining the exact tip shape and dynamics of liquid film removal/formation, only experimental description of the wetting/de-wetting and partial blinding phenomena has been reported based on the rise and the fall times of the detected signal (Cartellier, 1990, 1992; Cartellier and Achard, 1991; Julia et al., 2005).

After performing meticulous comparisons between the response curves and visual recordings, Julia et al. (2005) suggested the usage of a Lower Level Criterion (LLC) - defined as 10% of the maximum signal level – for differentiating which phase the tip is surrounded by.

B.1.2. Parallel piercing

In addition to the piercing near the bubble edge, Cartellier (1990) and Julia et al. (2005) also suggested parallel piercing as a source of error. Instead of the monotonic signal rise, Cartellier (1990) reported two peaks of different amplitudes when the probe tip was pierced across a gas-

liquid interface parallel to the tip long vertical axis orientation, thus parallel piercing. This phenomenon is illustrated in Figure B.3.

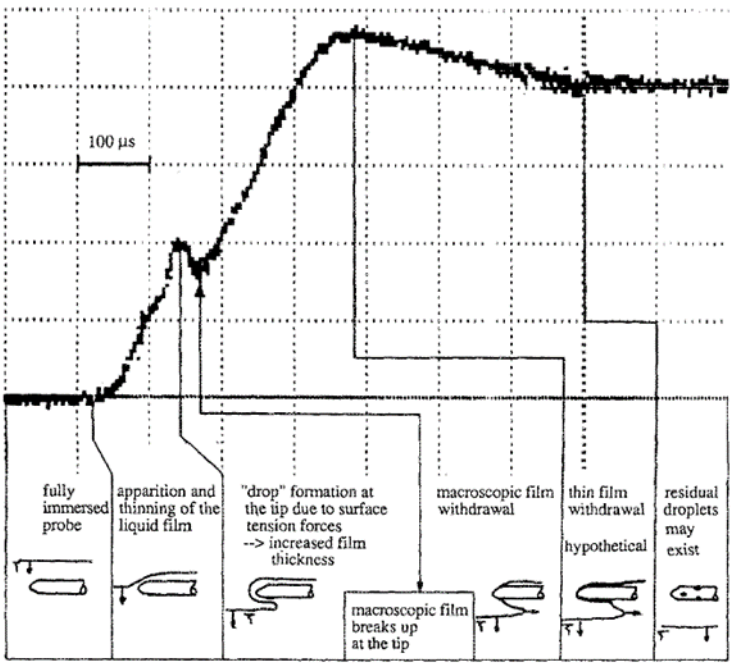

Figure B.3: Signal change when the tip is pierced sideways - parallel piercing (source: Cartellier, 1990).

The first peak occurs when the phase interface is disturbed by the tip, and the second peak occurs when the film is completely withdrawn from the tip. The duration of the signal rise (*Tm*) – which Cartellier (1990) defines as time to reach 90% of dry tip signal – was found to be very small when interfacial velocities were high. Specifically, for perpendicular piercing (gas-liquid interface perpendicular to the tip orientation), *Tm* was found to be less than ~ 0.3ms for interphase velocities larger than 50 cm/s. For parallel piercing, *Tm* was found to be less than ~ 0.8ms for interphase velocities larger than 50 cm/s. Although the average bubble velocities in our setups, i.e., gas-liquid stirred tanks, sparged tanks, and 2-D and 3-D bubble columns are much higher than this value (Xue, 2004; Mueller, 2009), since *Tm* is also a function of the exact tip

shape, it is unclear whether such effects are negligible. Further verifications may be required for each optical probe.

B.2. Signal interpretation

For the collected data presented throughout the dissertation, the signal density distributions of the signal levels were first plotted rather than obtaining visual images to quantify the effects of the two errors (piercing near the edge and parallel pierincing) combined. The rationale for this is as follows. Both studies by Cartellier (1990) and Julia et al. (2005) revealed a direct relationship between the two error types and the number of intermediate signal levels present. Thus, if negligible number of intermediate signals is observed, the above discussed errors can be neglected. On the other hand, if there is a significant number of intermediate signals present in our data, a new processing algorithm needs to be developed that takes into account these errors.

As an example, Figure B.4 shows several signal level distributions for the optical probe employed in gas-liquid stirred tank at various operating conditions (flooding, loading, transition, and fully recirculated regimes). On the left hand side are the original time-series data during the first 30 seconds. The collected signals were normalized by first subtracting the minimum voltage observed during the whole measurement time, and then dividing this value by the difference between the reference voltage and minimum voltage observed. The reference voltage was set to a value to have the dry tip signal be in between 0.8 and 1.2 (Equation 2.1):

$$V_{norm} = \frac{Meausred\ voltage - Minimum\ voltage}{Reference\ voltage - Minimum\ voltage} \tag{2.1}$$

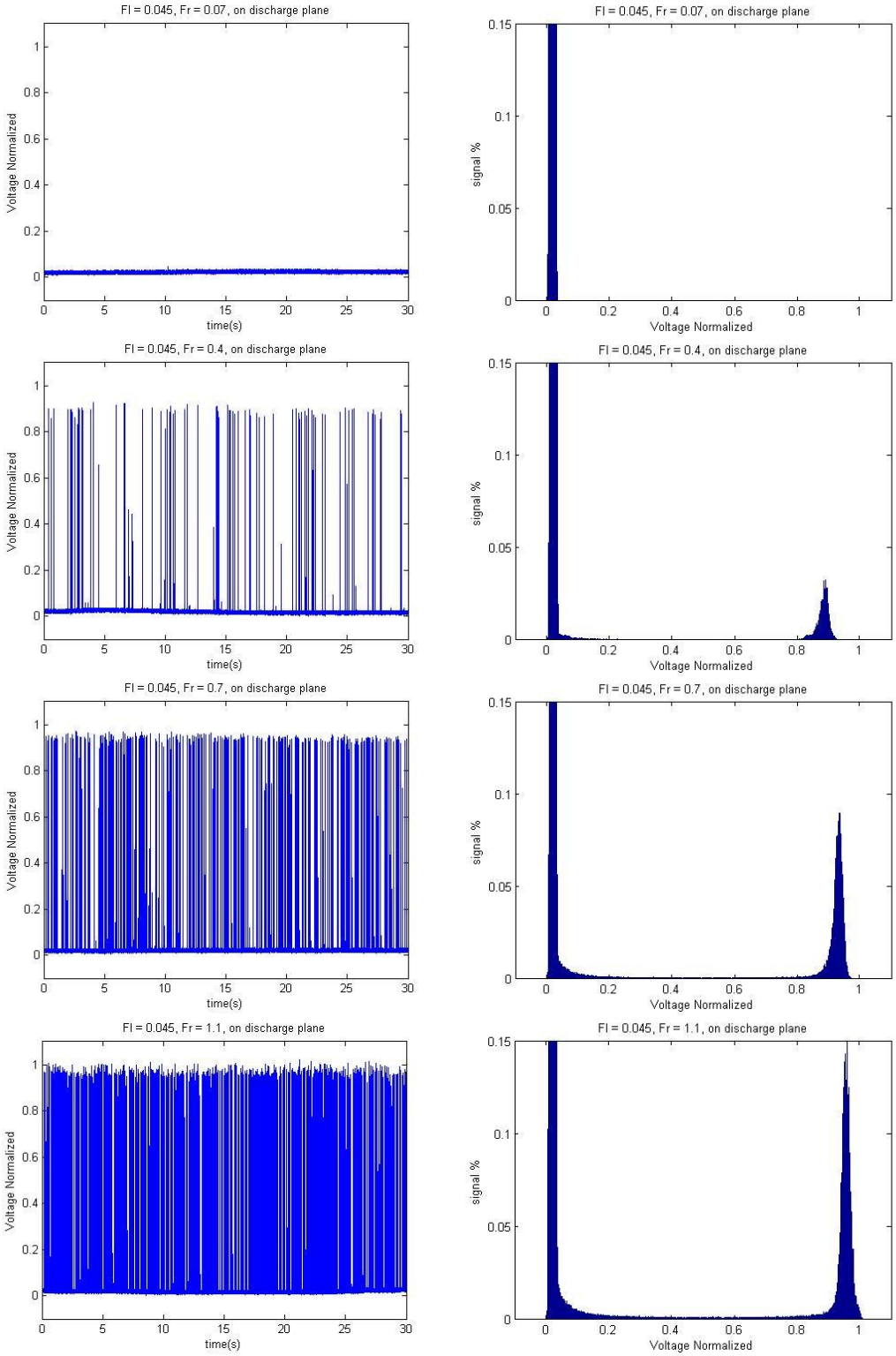

Figure B.4: Normalized voltage and corresponding signal level distributions for tips pointing inward. From top to bottom: flooding, loading, transition, and fully recirculated regime.

Appendix C. Improved 4-point probe algorithm

The 4-point probe algorithm originally developed by Xue (2004) was written in FORTRAN. This FORTRAN algorithm is very efficient and eloquent, however, the criteria for rejecting the "bad signals" that can skew the results were not detailed, e.g., multiple bubbles hitting different tips simultaneously and bubble only piercing three tips. To elucidate this uncertainty, in this section, we present a new and shorter version of the 4-point probe algorithm written in MATLAB.

C.1. Main code (Four_point_optical_probe_code.m)

```
clear all; clc;

% Declaring coordinates as global parameters
global x1 y1 z1 x2 y2 z2 x3 y3 z3;
% Declaring parameters in solver command as global parameters
global bigt0_calc bigt1_calc bigt2_calc bigt3_calc deltat1_calc deltat2_calc
deltat3_calc;
global bigt1_run1 bigt2_run1 bigt3_run1 deltat1_run1 deltat2_run1
deltat3_run1;

% Data collection frequency
freq=40000; %hz

% User defined tip coordinates
x1=-12/610; % in centimeters
y1=6/610; % in centimeters
z1=48/610; % in centimeters
% tip 2
x2=32/610; % in centimeters
y2=10/610; % in centimeters
z2=31/610; % in centimeters
% tip 3
x3=3/610; % in centimeters
y3=-16/610; % in centimeters
z3=50/610; % in centimeters

% Reading the txt file
raw_signal=csvread('filename.txt'); % Reading txt file
tip0=raw_signal(:,1); % Central tip signal
```

```
tip1=raw_signal(:,2); % Tip 1 signal
tip2=raw_signal(:,3); % Tip 2 signal
tip3=raw_signal(:,4); % Tip 4 signal

% Obtaining minimum and maximum voltage for each tip during the total
% measurement time
max_normal0=max(tip0); % Maximum voltage for central tip (gas phase) in volts
max_normal1=max(tip1); % Maximum voltage for tip 1(gas phase)
max_normal2=max(tip2); % Maximum voltage for tip 2(gas phase)
max_normal3=max(tip3); % Maximum voltage for tip 3(gas phase)
min_normal0=min(tip0); % Minimum voltage for central tip (liquid phase)
min_normal1=min(tip1); % Minimum voltage for tip 1 (liquid phase)
min_normal2=min(tip2); % Minimum voltage for tip 2 (liquid phase)
min_normal3=min(tip3); % Minimum voltage for tip 3 (liquid phase)

% Normalizing signal by substracting the minimum and then dividing maximum
voltage difference
nor_signal0=(tip0-min_normal0)./(max_normal0-min_normal0); % central tip
nor_signal1=(tip1-min_normal1)./(max_normal1-min_normal1); % tip 1
nor_signal2=(tip2-min_normal2)./(max_normal2-min_normal2); % tip 2
nor_signal3=(tip3-min_normal3)./(max_normal3-min_normal3); % tip 3

% Converting normalized signal to binary signal for central tip
signal_length=length(tip0);
for j=1:signal_length;
    if nor_signal0(j)<0.25;
        proc_signal0(j)=0;
    else proc_signal0(j)=1;  %so that when air=1, when in water=0
    end
end

for j=1:signal_length; %for tip 1
    if nor_signal1(j)<0.25;
        proc_signal1(j)=0;
    else proc_signal1(j)=1;
    end
end

for j=1:signal_length; %for tip 2
    if nor_signal2(j)<0.25;
        proc_signal2(j)=0;
    else proc_signal2(j)=1;
    end
end

for j=1:signal_length; %for tip 3
    if nor_signal3(j)<0.25;
        proc_signal3(j)=0;
    else proc_signal3(j)=1;
    end
end

% Let's get gas holdup
holdup0=mean(proc_signal0)*100 % central tip
```

```
holdup1=mean(proc_singal1)*100 % tip 1
holdup2=mean(proc_singal2)*100 % tip 2
holdup3=mean(proc_singal3)*100 % tip 3

% To free up un-needed variables memory used by matlab
clear raw_signal signal filname tip0 tip1 tip2 tip3 min_normal0
clear min_normal1 min_normal2 min_normal3 nor_signal0 nor_signal1
clear nor_signal2 nor_signal3

% From liquid to gas: step jump(center tip)
step_up0=zeros(1,signal_length);
step_up0(1)=0;
for k=2:signal_length;
    if proc_signal0(k)-proc_signal0(k-1)==1;
        step_up0(k)=k;
    else step_up0(k)=0;
    end
end
step_up0(step_up0==0)=[];
bubble_number_calc=length(step_up0)-1;

% Lets calculate big t0 (before rejecting bubbles not included in
% calculations)
for n=1:bubble_number_calc; % to calculate big t1
    tip0_stepup=step_up0(n);
    bigt0_loop=0;
    while proc_signal0(tip0_stepup+1)-proc_signal0(tip0_stepup)==0;
        bigt0_loop=bigt0_loop+1;
        tip0_stepup=tip0_stepup+1;
    end
    bigt0_pre(n)=bigt0_loop;
end
clear bigt0_loop tip0_stepup

% first criteria big t0 has to be larger than 10
for n=1:bubble_number_calc;
    if (bigt0_pre(n) < 15);
        bigt0_pre1(n)=0;
        step_up0_1(n)=0;
    else bigt0_pre1(n)=bigt0_pre(n);
        step_up0_1(n)=step_up0(n);
    end
end
bigt0_pre1(bigt0_pre1==0)=[];
step_up0_1(step_up0_1==0)=[];
bubble_number_calc=length(bigt0_pre1);

% Checking for simultaneous bubble occupancy for all four tips
starting_point=zeros(1,bubble_number_calc);
bigt0=zeros(1,bubble_number_calc);
for n=1:bubble_number_calc;
    duration_for_loop=bigt0_pre1(n);
    step_up_for_loop=step_up0_1(n);
    for m=step_up_for_loop+1:step_up_for_loop+duration_for_loop;
```

```
        if (proc_signal1(m)==1) && (proc_signal2(m)==1) &&
(proc_signal3(m)==1);
            starting_point(n)=step_up_for_loop;
            bigt0(n)=duration_for_loop;
            break
        end
    end
    clear duration_for_loop step_up_for_loop
end
starting_point(starting_point==0)=[]; %this gives you beginning point for 4-
point calculations
bigt0(bigt0==0)=[]; %big t0 to be used for calculations
bubble_number_used=length(starting_point);

% now obtaining (1) delta t1, t2, t3, and (2)T1, T2, T3
for n=1:bubble_number_used; % to calculate delta t1
    start_deltat1=starting_point(n);
    deltat1_loop=1;
    while proc_signal1(start_deltat1+2)-proc_signal1(start_deltat1+1)==0;
        deltat1_loop=deltat1_loop+1;
        start_deltat1=start_deltat1+1;
    end
    deltat1(n)=deltat1_loop;
end
clear deltat1_loop start_deltat1

for n=1:bubble_number_used; % to calculate delta t2
    start_deltat2=starting_point(n);
    deltat2_loop=1;
    while proc_signal2(start_deltat2+2)-proc_signal2(start_deltat2+1)==0;
        deltat2_loop=deltat2_loop+1;
        start_deltat2=start_deltat2+1;
    end
    deltat2(n)=deltat2_loop;
end
clear deltat2_loop start_deltat2

for n=1:bubble_number_used; % to calculate delta t3
    start_deltat3=starting_point(n);
    deltat3_loop=1;
    while proc_signal3(start_deltat3+2)-proc_signal3(start_deltat3+1)==0;
        deltat3_loop=deltat3_loop+1;
        start_deltat3=start_deltat3+1;
    end
    deltat3(n)=deltat3_loop;
end
clear deltat3_loop start_deltat3

for n=1:bubble_number_used; % to calculate big t1
    tip1_stepup=starting_point(n)+deltat1(n)+2;
    bigt1_loop=1;
    while proc_signal1(tip1_stepup)-proc_signal1(tip1_stepup-1)==0;
        bigt1_loop=bigt1_loop+1;
        tip1_stepup=tip1_stepup+1;
```

```
    end
    bigt1(n)=bigt1_loop;
    clear tip1_stepup bigt1_loop
end
clear deltat1_loop start_deltat1 bigt1_loop tip1_stepup start_deltat1

for n=1:bubble_number_used; % to calculate big t2
    tip2_stepup=starting_point(n)+deltat2(n)+2;
    bigt2_loop=1;
    while proc_signal2(tip2_stepup)-proc_signal2(tip2_stepup-1)==0;
        bigt2_loop=bigt2_loop+1;
        tip2_stepup=tip2_stepup+1;
    end
    bigt2(n)=bigt2_loop;
    clear tip2_stepup bigt2_loop
end
clear deltat2_loop start_deltat2 bigt2_loop tip2_stepup start_deltat2

for n=1:bubble_number_used; % to calculate big t3
    tip3_stepup=starting_point(n)+deltat3(n)+2;
    bigt3_loop=1;
    while proc_signal3(tip3_stepup)-proc_signal3(tip3_stepup-1)==0;
        bigt3_loop=bigt3_loop+1;
        tip3_stepup=tip3_stepup+1;
    end
    bigt3(n)=bigt3_loop;
    clear tip3_stepup bigt3_loop
end
clear deltat3_loop start_deltat3 bigt3_loop tip3_stepup start_deltat3

% Now lets screen out the ones that have very short bigt1, bigt2, and
% bigt3, criterion is that deltat1+bigt1>bigt0

bigt0_final=zeros(1,bubble_number_used);
bigt1_final=zeros(1,bubble_number_used);
bigt2_final=zeros(1,bubble_number_used);
bigt3_final=zeros(1,bubble_number_used);
deltat1_final=zeros(1,bubble_number_used);
deltat2_final=zeros(1,bubble_number_used);
deltat3_final=zeros(1,bubble_number_used);
starting_point_final=zeros(1,bubble_number_used);
%
for n=1:bubble_number_used;
    criterion1(n)=round(1/10*bigt0(n)); %to reject bubbles with occupancy
durations too low
    criterion2(n)=round(1/10*bigt0(n)); %to reject bubbles too fast and small
    criterion3(n)=round(9/10*bigt0(n)); %to reject bubbles hitting other
probes too fast
    if ((criterion2(n) <= deltat1(n)) && (criterion2(n) <= deltat2(n)) &&
(criterion2(n) <= deltat3(n)))...
        && (criterion1(n) <= bigt1(n)) && (criterion1(n) <= bigt2(n) &&
(criterion1(n) <= bigt3(n)))...
        && (deltat1(n)<=criterion3(n)) && (deltat2(n)<=criterion3(n)) &&
(deltat3(n)<=criterion3(n)));
```

```
        bigt0_final(n)=bigt0(n);
        bigt1_final(n)=bigt1(n);
        bigt2_final(n)=bigt2(n);
        bigt3_final(n)=bigt3(n);
        deltat1_final(n)=deltat1(n);
        deltat2_final(n)=deltat2(n);
        deltat3_final(n)=deltat3(n);
        starting_point_final(n)=starting_point(n);
    end
end
bigt0_final(bigt0_final==0)=[];
bigt1_final(bigt1_final==0)=[];
bigt2_final(bigt2_final==0)=[];
bigt3_final(bigt3_final==0)=[];
deltat1_final(deltat1_final==0)=[];
deltat2_final(deltat2_final==0)=[];
deltat3_final(deltat3_final==0)=[];
starting_point_final(starting_point_final==0)=[];
bubble_number_used=length(bigt0_final);


clear criterion1 criterion2 criterion3

% Now solving for theta=x(1), lowerphi=x(2), v-cos(higherphi)=x(3)
% using built-in MATLAB solver (first round to get estimate for initial
% guess)

for n=1:bubble_number_used;
    bigt0_calc=bigt0_final(n)/freq;
    bigt1_calc=bigt1_final(n)/freq;
    bigt2_calc=bigt2_final(n)/freq;
    bigt3_calc=bigt3_final(n)/freq;
    deltat1_calc=deltat1_final(n)/freq;
    deltat2_calc=deltat2_final(n)/freq;
    deltat3_calc=deltat3_final(n)/freq;

    x0=[pi()/6;pi()/6;30];
    options = optimset('TolX',1e-15,'TolFun',1e-
15,'MaxIter',100000,'MaxFunEvals',100000);
    %this function minimizes the function in bubble.m to reduce at
    %given range, for my case -1<x(1)<-1 since arcsin range, -1<x(2)<1
    %since arccos range and velocity non negative
    x=lsqnonlin(@bubble,x0,[-1;-1;0],[1;1;200],options);

    atheta(n)=x(1);
    alowerphi(n)=x(2);
    velocity(n)=x(3);
    theta(n)=asind(atheta(n));
    lowerphi(n)=acosd(alowerphi(n));
    clear x
end

velocity_mean(i)=mean(velocity)
velocity_std(i)=std(velocity)
```

```
figure(1);
hist(velocity,100);

%Now lets get the bubble chord length distribution
% L(i)=v-cos(higherphi)
% so for each bubble counted for velocity calculations, we have 4
% bubble chord length values
for n=1:bubble_number_used;
    chord1(n)=velocity(n)*bigt0_final(n);
    chord2(n)=velocity(n)*bigt1_final(n);
    chord3(n)=velocity(n)*bigt2_final(n);
    chord4(n)=velocity(n)*bigt3_final(n);
end
figure(2);
chord_length_final=[chord1 chord2 chord3 chord4]/freq*100; %in mm
hist(chord_length_final,100);

%Now lets calculate specific interfacial area
sum_pre=1./velocity;
inter_area=1/(length(proc_signal0)/40000)*length(bigt0_pre)/(length(bigt0_fin
al))...
    *sum(sum_pre); %in units of cm-1
```

C.2. Function code (bubble.m)

```
function F = bubble(x)
% sin(theta)=x(1), cos(lowerphi)=x(2), v-cos(higherphi)=x(3)
global x1 y1 z1 x2 y2 z2 x3 y3 z3
global bigt0_calc bigt1_calc bigt2_calc bigt3_calc deltat1_calc deltat2_calc
deltat3_calc;

F=zeros(3,1);
F=[(x1*x(1)*x(2)+y1*x(1)*((1-(x(2))^2)^(1/2))+z1*((1-
(x(1))^2)^(1/2)))/x(3)+(bigt0_calc-bigt1_calc)/2-deltat1_calc;
    (x2*x(1)*x(2)+y2*x(1)*((1-(x(2))^2)^(1/2))+z2*((1-
(x(1))^2)^(1/2)))/x(3)+(bigt0_calc-bigt2_calc)/2-deltat2_calc;
    (x3*x(1)*x(2)+y3*x(1)*((1-(x(2))^2)^(1/2))+z3*((1-
(x(1))^2)^(1/2)))/x(3)+(bigt0_calc-bigt3_calc)/2-deltat3_calc;]
```

References

1. Al-Dahhan, M.H., 2006. Bubble/slurry bubble column reactors. CREL workshop on multiphase reactor technology.

2. Avdeev, M.V., Konovalov, A.N., Bagratashvili, V.N., Popov, V.K., Tsypina, S.I., Sokolova, M., Ke, J., Poliakoff, M., 2004. The fibre optic reflectometer: A new and simple probe for refractive index and phase separation measurements in gases, liquids and supercritical fluids. Physical Chemistry Chemical Physics 6, 1258-1263.

3. Bakker, A., Van Den Akker, H.E.A., 1994. A computational model for the gas-liquid flow in stirred reactors. Chemical Engineering Research & Design 72, 594-606.

4. Bao, Y., Gao, Z., Li, Z., Bai, D., Smith, J.M., Thorpe, R.B., 2008. Solid suspension in a boiling stirred tank with radial flow turbines. Industrial & Engineering Chemistry Research 47, 2420-2427.

5. Bao, B., Fadaei, H., Sinton, D., 2015. Detection of bub ble and dew point using thin-film interference. Sensors and Actuators B 207, 640-649.

6. Bombac, A., Zun, I., Filipic, B., Zumer, M., 1997. Gas-filled cavity structures and local void fraction distribution in aerated stirred vessel. AIChE Journal 43, 2921 – 2931.

7. Bombac, A., Zun, I., 2000. Gas-filled cavity structures and local void fraction distribution in vessel with dual-impellers. Chemical Engineering Science 55, 2995-3001.

8. Bombac, A., Zun, I., 2006. Individual impeller flooding in aerated vessel stirred by multiple-Rushton impellers. Chemical Engineering Journal 116, 85-95.

9. Boyer, C., Duquenne, A.-M., Wild, G., 2002. Measuring techniques in gas–liquid and gas–liquid–solid reactors. Chemical Engineering Science 57, 3185-3215.

10. Bhusarapu, S.B., 2005. Solids Flow Mapping in Gas-Solid Risers. Department of Chemical Engineering. Washington University.

11. Buffo, A., Vanni, M., Marchisio, D.L., 2012. Multidimensional population balance model for the simulation of turbulent gas–liquid systems in stirred tank reactors. Chemical Engineering Science 70, 31-44.

12. Buwa, V.V., Ranade, V.V, 2002. Dynamics of gas-liquid flow in rectangular bubble column: experiments and single/multi-group CFD simulations. Chemical Engineering Science 57, 4714-4736.

13. Cartellier, A., 1990. Optical probes for local void fraction measurements: Characterization of performance. Review of Scientific Instruments 61, 874-886.

14. Cartellier, A., Achard, J.L., 1991. Local phase detection probes in fluid/fluid two-phase flows. Review of Scientific Instruments 62, 279-303.

15. Cartellier, A., 1992. Simultaneous void fraction measurement, bubble velocity, and size estimate using a single optical probe in gas--liquid two-phase flows. Review of Scientific Instruments 63, 5442-5453.

16. Cents, A.H.G., Brilman, D.W.F., Versteeg, G.F., 2005. Ultrasonic investigation of hydrodynamics and mass transfer in a gas-liquid(-liquid) sitrred vessel. International Journal of Chemical Reactor Engineering 3, 32.

17. Chaouki, J., Larachi, F., Duduković, M.P., 1997. Noninvasive Tomographic and Velocimetric Monitoring of Multiphase Flows. Industrial & Engineering Chemistry Research 36, 4476-4503.

18. Chen, P., 2004. Modeling the Fluid Dynamics of Bubble Column Flows. Department of Chemical Engineering. Washington University.

19. Degaleesan, S., 1997. Fluid Dynamic Measurements and Modeling of Liquid Mixing in Bubble Columns. Department of Chemical Engineering. Washington University.

20. Devanathan, N., 1991. Investigation of Liquid Hydrodynamics in Bubble Columns via Computer Automated Radioactive Particle Tracking (CARPT). Department of Chemical Engineering. Washington University.

21. Drahos, J., Bradka, F., Puncochar, M., 1992. Fractal behaviour of pressure fluctuations in a bubble column. Chemical Engineering Science 47, 4069-4075.

22. Dudukovic, M.P., 2009. Frontiers in Reactor Engineering. Science 325.

23. Dudukovic, M.P., Larachi, F., Mills, P.L., 2002. Multiphase catalytic reactors: a perspective on current knowledge and future trends. Catalysis Reviews.

24. Fogler, H.S., 2006. Elements of Chemical Reaction Engineering. Prentice Hall.

25. Ford, J.J., Heindel, T.J., Jensen, T.C., Drake, J.B., 2008. X-ray computed tomography of a gas-sparged stirred-tank reactor. Chemical Engineering Science 63, 2075-2085.

26. Fordham, E.J., Holmes, A., Ramos, R.T., Simonian, S., Huang, S.M., Lenn, C.P., 1999a. Multi-phase-fluid discrimination with local fibre-optical probes: I. Liquid/liquid flows. Measurement Science and Technology 10, 1329.

27. Fordham, E.J., Simonian, S., Ramos, R.T., Holmes, A., Huang, S.M., Lenn, C.P., 1999b. Multi-phase-fluid discrimination with local fibre-optical probes: II. Gas/liquid flows. Measurement Science and Technology 10, 1338.

28. Fordham, E.J., Ramos, R.T., Holmes, A., Simonian, S., Huang, S.M., Lenn, C.P., 1999c. Multi-phase-fluid discrimination with local fibre-optical probes: III. Three-phase flows. Measurement Science and Technology 10, 1347.

29. Fowles, G.R., 1975. Introduction to Modern Optics. Dover-Publ.

30. Fraguío, M.S., Cassanello, M.C., Larachi, F., Limtrakul, S., Dudukovic, M., 2007. Classifying flow regimes in three-phase fluidized beds from CARPT experiments. Chemical Engineering Science 62, 7523-7529.

31. Fraguio, M.S., Cassanello, M.C., Degaleesan, S., Dudukovic, M., 2008. Flow Regime Diagnosis in Bubble Columns via Pressure Fluctuations and Computer-Assisted Radioactive Particle Tracking Measurements. Industrial & Engineering Chemistry Research 48, 1072-1080.

32. Frijlink, J.J., 1987. Physical Aspects of Gassed Suspension Reactors. Delft university of Technology.

33. Gao, Z., Smith, J.M., Müller-Steinhagen, H., 2001. Void fraction distribution in sparged and boiling reactors with modern impeller configuration. Chemical Engineering and Processing: Process Intensification 40, 489-497.

34. Ghadge, R.S., Patwardhan, A.W., Sawant, S.B., Joshi, J.B., 2005. Effect of flow pattern on cellulose deactivation in stirred tank bioreactors. Chemical Engineering Science 60, 1067-1083.

35. Groen, J.S., 2005. Scales and structures in bubbly flows. Experimental analysis of the flow in bubble columns and in bubbling fluidized beds. Delft university of Technology.

36. Guet, S., Fortunati, R.V., Mudde, R.F., Ooms, G., 2003. Bubble Velocity and Size Measurement with a Four-Point Optical Fiber Probe. Particle & Particle Systems Characterization 20, 219-230.

37. Guha, D., 2007. Hydrodynamics and Mixing in Single Phase and Liquid-Solid Stirred Tank Reactors. Department of Energy, Environmental and Chemical Engineering. Washington University.

38. Gupta, P., 2002. Churn-Turbulent Bubble Columns – Experiments and Modeling. Department of Chemical Engineering. Washington University.

39. Hamad, F.A., Imberton, F., Bruun, H.H., 1997. An optical probe for measurements in liquid - liquid two-phase flow. Measurement Science and Technology 8, 1122.

40. Hamad, F.A., Pierscionek, B.K., Bruun, H.H., 2000. A dual optical probe for volume fraction, drop velocity and drop size measurements in liquid-liquid two-phase flow. Measurement Science and Technology 11, 1307.

41. Hamed, M.E., 2012. Hydrodynamics, Mixing, and Mass Transfer in Bubble Columns with Internals. Department of Energy, Environmental, and Chemical Engineering. Washington University.

42. Hamidipour, M., Chen, J., Larachi, F., 2012. CFD study on hydrodynamics in three-phase fluidized beds-Applications of turbulence models and experimental validation. Chemical Engineering Science 78, 167-180.

43. Han, L., 2007. Hydrodynamics, Back-mixing, and Mass Transfer in a Slurry Bubble Column Reactor for Fischer-Tropsch Alternative Fuels. Department of Chemical Engineering. Washington University.

44. Harnby, N., Edwards, F., Nienow, A.W., 1985. Mixing in the process industries. Butterworths.

45. Harris, F.J., 1978. On the use of windows for harmonic analysis with the discrete Fourier transform. Proceedings of the IEEE 66, 51-83.

46. Hill, J.H., 1976. The operation of a bubble column at high throughputs: I. Gas holdup measurements. Chemical Engineering Journal 12, 89-99.

47. Jade, A.M., Jayaraman, V.K., Kulkarni, B.D., Khopkar, A.R., Ranade, V.V., Ashutosh, S., 2006. A novel local singularity distribution based method for flow regime identification: Gas–liquid stirred vessel with Rushton turbine. Chemical Engineering Science 61, 688-697.

48. Jiri, V., Vecer, M., Orvalho, S., Sechet, P., Ruzicka, M.C., Cartellier, A., 2010. Measurement accuracy of a mono-fiber optical probe in a bubble flow. International Journal of Multiphase Flow 36, 533-548.

49. Johnsson, F., Zijerveld, R.C., Schouten, J.C., van den Bleek, C.M., Leckner, B., 2000. Characterization of fluidization regimes by time-series analysis of pressure fluctuations. International Journal of Multiphase Flow 26, 663-715.

50. Julia, J.E., Harteveld, W.K., Mudde, R.F., Van den Akker, H.E.A., 2005. On the accuracy of the void fraction measurements using optical probes in bubbly flows. Review of Scientific Instruments 76.

51. Kataoka, I., Ishii, M., Serizawa, A., 1986. Local formulation and measurements of interfacial area concentration in two-phase flow. International Journal of Multiphase Flow 12, 505-529.

52. Kerdouss, F., Bannari, A., Proulx, P., 2006. CFD modeling of gas dispersion and bubble size in a double turbine stirred tank. Chemical Engineering Science 61, 3313-3322.

53. Khopkar, A.R., Panaskar, S.S., Pandit, A.B., Ranade, V.V., 2005. Characterization of gas−liquid flows in stirred vessels using pressure and torque fluctuations. Industrial & Engineering Chemistry Research 44, 3298-3311.

54. Khopkar, A.R., Ranade, V.V., 2006. CFD simulation of gas–liquid stirred vessel: VC, S33, and L33 flow regimes. AIChE Journal 52, 1654-1672.

55. Kong, L.N., Li, W., Han, L.C., Liu, Y.J., Luo, H.A., Al Dahhan, M., Dudukovic, M.P., 2012. On the measurement of gas holdup distribution near the region of impeller in a gas-liquid stirred Rushton tank by means of gamma-CT. Chemical Engineering Journal 188, 191-198.

56. Krishna, R., Van Baten, J.M., Urseanu, M.I., 2000. Three-phase Eulerian simulations of bubble column reactors operating in the churn-turbulent regime: a scale up strategy. Chemical Engineering Science 55, 3275-3286.

57. Kumar, S.B., Moslemian, D., Dudukovic, M.P., 1997. Gas-holdup measurements in bubble columns using computed tomography. AIChE Journal 43, 1414-1425.

58. Laborde-Boutet, C., Larachi, F., Dromard, N., Delsart, O., Beliard, P.E., Schweich, D., 2010. CFD simulations of hydrodynamic/thermal coupling phenomena in a bubble column with internals. AIChE Journal 56, 2397-2411.

59. Lane, G.L., Schwarz, M.P., Evans, G.M., 2002. Predicting gas–liquid flow in a mechanically stirred tank. Applied Mathematical Modelling 26, 223-235.

60. Lane, G.L., Schwarz, M.P., Evans, G.M., 2005. Numerical modelling of gas–liquid flow in stirred tanks. Chemical Engineering Science 60, 2203-2214.

61. Lee, B.W., Dudukovic, M.P., 2014a. Determination of flow regime and gas holdup in gas–liquid stirred tanks. Chemical Engineering Science 109, 264-275.

62. Lee, B.W., Dudukovic, M.P., 2014b. Time-series analysis of optical probe measurements in gas–liquid stirred tanks. Chemical Engineering Science 116, 623-634.

63. Lee, B.W., Dudukovic, M.P., 2015. A probabilistic model for correcting the directional sensitivity of optical probe measurements. AIChE Journal 61, 3516-3527.

64. Letzel, H.M., Schouten, J.C., Krishna, R., Van Den Bleek, C.M., 1997. Characterization of regimes and regime transitions in bubble columns by chaos analysis of pressure signals. Chemical Engineering Science 52, 4447-4459.

65. Levenspiel, O., 2002. The Chemical Reactor Omnibook. OSU Bookstore.

66. Li, Z., Song, G., Bao, Y., Gao, Z., 2013. Stereo-PIV experiments and large eddy simulations of flow fields in stirred tanks with Rushton and curved-Blade turbines. AIChE Journal 59, 3986-4003.

67. Liao, Y., Lucas, D., 2009. A literature review of theoretical models for drop and bubble breakup in turbulent dispersions. Chemical Engineering Science 64, 3389-3406.

68. Lin, T.J., Juang, R.C., Chen, Y.C., Chen, C.C., 2001. Predictions of flow transitions in a bubble column by chaotic time series analysis of pressure fluctuation signals. Chemical Engineering Science 56, 1057-1065.

69. Liu, T.J., 1993. Bubble size and entrance length effects on void development in a vertical channel. International Journal of Multiphase Flow 19, 99-113.

70. Manjrekar, O.N., Dudukovic, M.P., 2015. Application of a 4-point optical probe to a slurry bubble column reactor. Chemical Engineering Science 131, 313-322.

71. Mizushima, Y., Sakamoto, A., Saito, T., 2013. Measurement technique of bubble velocity and diameter in a bubble column via single-tip optical-fiber probing with judgment of the pierced position and angle. Chemical Engineering Science 100, 98-104.

72. Mudde, R.F., Groen, J.S., Van Den Akker, H.E.A., 1997. Liquid velocity field in a bubble column: LDA experiments. Chemical Engineering Science 52, 4217-4224.

73. Mudde, R.F., Groen, J.S., Van Den Akker, H.E.A., 1998. Application of LDA to bubbly flows. Nuclear Engineering and Design 184, 329-338.

74. Mueller, S.G., Weber, J.R., Al-Dahhan, M.H., Dudukovic, M.P., 2007. Using a fiber-optic probe for the measurement of volumetric expansion of liquids. Industrial & Engineering Chemistry Research 46, 4330-4334.

75. Mueller, S.G., 2009. Optical Measurements in Gas-Liquid Stirred Tanks. Department of Energy, Environmental and Chemical Engineering. Washington University.

76. Mueller, S.G., Dudukovic, M.P., 2010. Gas holdup in gas-liquid stirred tanks. Industrial & Engineering Chemistry Research 49, 10744-10750.

77. Paglianti, A., Pintus, S., Giona, M., 2000. Time-series analysis approach for the identification of flooding/loading transition in gas–liquid stirred tank reactors. Chemical Engineering Science 55, 5793-5802.

78. Petitti, M., Nasuti, A., Marchisio, D.L., Vanni, M., Baldi, G., Mancini, N., Podenzani, F., 2010. Bubble size distribution modeling in stirred gas–liquid reactors with QMOM augmented by a new correction algorithm. AIChE Journal 56, 36-53.

79. Piela, K., Delfos, R., Ooms, G., Westerweel, J., Oliemans, R.V.A., 2009. Dispersed oil–water–gas flow through a horizontal pipe. AIChE Journal 55, 1090-1102.

80. Rammohan, A.R., 2002. Characterization of Single and Multiphase Flows in Stirred Tank Reactors, Department of Chemical Engineering. Washington.

81. Ramos, R.T., Fordham, E.J., 1990. Oblique-tip fiber-optic sensors for multiphase fluid discrimination. Journal of Lightwave Technology 17, 1392-1440.

82. Revstedt, J., Fuchs, L., Kovács, T., Tragardh, C., 2000. Influence of impeller type on the flow structure in a stirred reactor. AIChE Journal 46, 2373-2382.

83. Rogerio, T.R., Andrew, H., Xu, W., Elizabeth, D., 2001. A local optical probe using fluorescence and reflectance for measurement of volume fractions in multi-phase flows. Measurement Science and Technology 12, 871.

84. Roghair, I., Lau, Y.M., Deen, N.G., Slagter, H.M., Baltussen, M.W., Van Sint Annaland, M., Kuipers, J.A.M., 2011. On the drag force of bubbles in bubble swarms at intermediate and high Reynolds numbers. Chemical Engineering Science 66, 3204-3211.

85. Shah, Y.T., Kelkar, B.G., Godbole, S.P., Decker, W.D., 1982. Design parameters estimations for bubble column reactors. AIChE Journal 28, 353-379.

86. Shaikh, A., Al-Dahhan, M., 2007. A review on flow regime transitions in bubble columns. International Journal of Chemical Reactor Engineering 5, 1-68.

87. Shamlou, P.A., Makagiansar, H.Y., Ison, A.P., Lilly, M.D., Thomas, C.R., 1994. Turbulent breakage of filamentous microorganisms in submerged culture in mechanically stirred bioreactors. Chemical Engineering Science 49, 2621-2631.

88. Shetty, S.A., Kantak, M.V., Kelkar, B.G., 1992. Gas-phase backmixing in bubble column reactors. AIChE Journal 38, 1013-1026.

89. Smith, J.M., Gao, Z., 2001. Power demand of gas dispersing impellers under high load conditions. Chemical Engineering Research and Design 79, 575-580.

90. Stitt, H., 2002. Alternative multiphase reactors for fine chemicals. A world beyond stirred tanks? Chemical Engineering Journal 90, 47-60.

91. Sun, Y., Mueller, S.G., Lee, B.W., Dudukovic, M.P., 2013. Optical fiber reflectance probe for detection of phase transitions in multiphase systems. Industrial & Engineering Chemistry Research 53, 999-1003.

92. Tatterson, G.B., 1991. Fluid mixing and gas dispersion in agitated tanks. McGraw-Hill.

93. Van Ommen, J.R., Sasic, S., van der Schaaf, J., Gheorghiu, S., Johnsson, F., Coppens, M.O., 2011. Time-series analysis of pressure fluctuations in gas–solid fluidized beds – A review. International Journal of Multiphase Flow 37, 403-428.

94. Vasconcelos, J.M.T., Orvalho, S.C.P., Rodrigues, A.M.A.F., Alves, S.S., 1999. Effect of Blade Shape on the Performance of Six-Bladed Disk Turbine Impellers. Industrial & Engineering Chemistry Research 39, 203-213.

95. Wang, M., Dorward, A., Vlaev, D., Mann, R., 2000. Measurements of gas–liquid mixing in a stirred vessel using electrical resistance tomography (ERT). Chemical Engineering Journal 77, 93-98.

96. Wang, W., Mao, Z.S., Yang, C., 2006. Experimental and numerical investigation on gas holdup and flooding in an aerated stirred tank with Rushton impeller. Industrial & Engineering Chemistry Research 45, 1141-1151.

97. Warmoeskerken, M.M.C.G., Smith, J.M., 1985. Flooding of disc turbines in gas-liquid dispersions: A new description of the phenomenon. Chemical Engineering Science 40, 2063-2071.

98. Warsito, W., Fan, L.S., 2005. Dynamics of spiral bubble plume motion in the entrance region of bubble columns and three-phase fluidized beds using 3D ECT. Chemical Engineering Science 60, 6073-6084.

99. Welch, P.D., 1967. The use of fast Fourier transform for the estimation of power spectra: A method based on time averaging over short, modified periodograms. Audio and Electroacoustics, IEEE Transactions 15, 70-73.

100. Werther, J., Hage, B., Rudnick, C., 1996. A comparison of laser Doppler and single-fibre reflection probes for the measurement of the velocity of solids in a gas-solid circulating fluidized bed. Chemical Engineering and Processing: Process Intensification 35, 381-391.

101. Wu, C., 2007. Heat Transfer and Bubble Dynamics in Slurry Bubble Columns for Fischer-Tropsch Clean Alternative Energy. Department of Energy, Environmental and Chemical Engineering. Washington University.

102. Xue, J., 2004. Bubble Velocity, Size and Interfacial Area Measurements in Bubble Columns. Department of Chemical Engineering. Washington University.

103. Yang, G.Q., Fan, L.S., 2003. Axial liquid mixing in high-pressure bubble columns. AIChE Journal 49, 1995-2008.

104. Yang, G.Q., Du, B., Fan, L.S., 2007. Bubble formation and dynamics in gas–liquid–solid fluidization—A review. Chemical Engineering Science 62, 2-27.

105. Yang, N., Wu, Z., Chen, J., Wang, Y., Li, J., 2011. Multi-scale analysis of gas-liquid interaction and CFD simulation of gas-liquid flow in bubble columns. Chemical Engineering Science 66, 3212-3222.

106. Youssef, A.A., 2010. Fluid Dynamics and Scale-up of Bubble Columns with Internals. Department of Energy, Environment and Chemical Engineering. Washington University.

107. Zhang, Y., Yang, C., Mao, Z.S., 2008. Large eddy simulation of the gas–liquid flow in a stirred tank. AIChE Journal 54, 1963-1974.

108. Zhang, Q., Yong, Y., Mao, Z.S., Yang, C., Zhao, C., 2009. Experimental determination and numerical simulation of mixing time in a gas–liquid stirred tank. Chemical Engineering Science 64, 2926-2933.